Fully Coupled CEM/CFD Modelling of Microwave Heating in a Porous Medium

Duško D. Dinčov

Centre for Numerical Modelling and Process Analysis
School of Computing and Mathematical Sciences
the University of Greenwich
London

A thesis submitted in partial fulfillment of the requirements of the University of Greenwich for the Degree of Doctor of Philosopy

This research programme was sponsored by the University of Greenwich

June 20, 2002

Abstract

Computational results for the microwave heating of a porous material are presented in this paper. Coupled finite difference time domain and finite volume methods are used to solve equations that describe the electromagnetic field and heat and mass transfer in porous media. These equations are nonlinearly coupled through the dielectric properties which depend both on temperature and moisture content. By investigating the resonant behaviour in two-dimensional microwave cavities, the FD-TD scheme is validated. Validation of the microwave power distribution in 3-D microwave enclosures is compared with other numerical results available. 3-D temperature distribution in a biomaterial is validated against experimental results. Results using the proposed fully coupled approach are discussed and analyzed. The model is able to reflect the evolution of both temperature and moisture fields as well as energy penetration as the moisture in the porous medium evaporates. Moisture movement results from internal pressure gradients produced by the internal heating and phase change. The model is validated by comparison to some published results for simpler problems.

Acknowledgements

I would like to take this opportunity to express my sincere gratitude to my supervisors Professor Kevin Parrott and Professor Koulis Pericleous for their guidance throughout the study.

This research would not have been carried out without the financial support of the University of Greenwich. The support provided by this grant is gratefully appreciated.

I would also like to express my sincere thanks to Suchitra, Kamal and Matti and all of my other friends and colleagues for their encouragement, suggestions and assistance.

Special thanks to Dr Laurent Leboucher and Dr Nick Croft for their assistance during the preparation of this manuscript.

Finally, I would like to thank my family for their support through my many years in education.

Contents

List of Figures

Nomenclature

Roman Letters

a_P = System matrix diagonal coefficient for element P 69

a_{nb} = Coefficient multiplying neighbour nb 69

A_f = Area of a face (m^{-2}) 66

d_{RP} = Distance between centres of elements R and P (m) 66

D_f = Diffusion Conductance through face f 69

A_s = Total interface area (m^{-2}) 59

C_p = Specific heat $(Jkg^{-1}K^{-1})$ 59

C_{max} = Local electromagnetic wave speed (ms^{-1}) 84

D_{max} = Maximum dimension of the geometry of the heating system (m) 86

E_0 = Electric field strength on the surface (Vm^{-1}) 16

H = Enthalpy $(Jkg^{-1}s^{-1})$ 59

H^{int} = Interphase enthalpy $(Jkg^{-1}s^{-1})$ 59

J_S = Mass flux of vapour in sublimation-condensation region $(kgm^{-2}s^{-1})$ 78

K = Permeability 61

L = Latent heat of vaporization (Jkg^{-1}) 62

L_{crit} = Critical slab thickness (m) 21

M = Moisture content 57

P_E	=	Electric power (W)	16
P_{E0}	=	Electric power on the surface (W)	16
Q	=	Heating function (W/m^3)	56
S	=	Surface (m^2)	55
S_{IP}	=	Interphase source terms	57
S_Φ	=	Source term	57
T	=	Temperature (^oC)	59
T_a	=	Convective air temperature (^oC)	62
T_s	=	Load surface temperature (^oC)	62
V	=	Volume (m^3)	55
$\dot{m}$	=	Interphase mass trasfer rate	60
$\mathbf{B}$	=	Magnetic flux density vector (T)	30
$\mathbf{D}$	=	Electric flux density vector (Cm^{-2})	30
$\mathbf{E}$	=	Electric field intensity vector (Vm^{-1})	30
$\mathbf{H}$	=	Magnetic field intensity vector (Am^{-1})	30
$\mathbf{J}$	=	Conduction electric current density vector (Am^{-2})	30
$\mathbf{S}$	=	Poynting vector (W/m^2)	55
$\mathbf{u}$	=	Velocity vector (ms^{-1})	57
d	=	Penetration depth (m)	16
h_c	=	Convective heat transfer coefficient $(Wm^{-2}K^{-1})$	62
h_m	=	bulk-to-interface mass transfer coefficient $(Wm^{-2}K^{-1})$	60
h_{ij}	=	Bulk-to-interface heat transfer coefficient $(Wm^{-2}K^{-1})$	59
k	=	Conductivity $(Wm^{-1}K^{-1})$	59
p	=	Pressure (Pa)	61
p_c	=	Capillary pressure (Pa)	61
r	=	Volume fraction	56

u_{sat} = Moisture content of a saturated porous medium (kgm^{-3}) 78

F_f = Strength of convection through face f 69

$\mathbf{n}$ = Unit outward normal 65

Greek Letters

χ = Electric susceptibility 13

δ = Mesh size (m) 45

ϵ' = Dielectric constant (F/m) 12

ϵ'' = Dielectric loss factor (F/m) 12

ϵ''_{eff} = Effective relative loss factor 12

ϵ'_r = Relative dielectric constant 12

ϵ_0 = Permittivity of vacuum (F/m) 12

ϵ_{rad} = Radiative surface emissivity 62

Γ_Φ = Exchange coefficient for Φ 57

λ = Wavelength (m) 45

λ_0 = Wavelength in free space (m) 16

μ = Magnetic permeability (H/m) 30

ν = Viscosity (m^2s^{-1}) 61

ω = Angular frequency (rad/s) 13

ϕ = Porosity 57

ρ = Density (kgm^{-3}) 30

σ_{eff} = Effective conductivity (S/m) 13

σ_{rad} = Stefan–Boltzmann constant $(Wm^{-2}K^{-4})$ 62

Subscripts and Superscripts

A = Adjacent element 66

g	=	Gas	57
i	=	i^{th} phase	57
l	=	Liquid	57
s	=	Solid	57
sl	=	Solid-liquid	57
f	=	Face	65
nb	=	Neighbouring Elements	69

CHAPTER

ONE

Introduction

The microwave heating of food was first found in 1945 by Percy L. Spencer at the Raytheon Manufacturing Laboratories in Waltham, Massachussets. He accidentally discovered that radar waves had melted a candy bar in his pocket. Experiments showed that microwave heating could raise the internal temperature of many foods far more rapidly than a conventional oven. The first Raytheon commercial microwave oven was the 1161 Radarange, which was marketed in 1954. Rated at 1600 watts, it was so large and expensive that it was practical only for restaurant and institutional use. Over the years microwave heating phenomenon was understood better and the microwave oven had become a necessity in the commercial market with many possibilities. Nowadays, microwave heating is a common way of heating objects that is used in domestic, industrial and biomedical applications.

The ability of the microwave energy to penetrate and, hence, heat from within the product, helps reduce processing times, costs and in some cases of ceramic processing, reduce the sintering temperature. Conventional heating methods conduct heat from the surface of the product inward, while microwave heating acts as a volumetrically distributed heat source as a result of dielectric losses. It transfers energy directly into the product, providing fast heating throughout the entire product. The interaction of microwaves with materials provides a basis for obtaining controlled and precise heating. Energy saving is achieved due to the fact that microwaves are absorbed only in dried product, whereas the surrounding air space remains cool. Other advantages

over the conventional means of heating include energy efficiency, lack of combustion products and a quick start-up period.

One problem which has arisen though, is the control of heat generated by the microwaves, which can easily cause thermal runaway[5] and thus destruction of a material. Thermal runaway occurs when the thermal absorptivity increases with temperature. Safety hazards, such as overheating, stem from the lack of knowledge of the simultaneous heat transfer, moisture transfer and other changes occurring during microwave heating.

Microwave heating is most beneficial when used for materials that are not good conductors of electricity and contain water. Nevertheless, other materials can still be heated efficiently and quickly. It is an important industrial process for heating water-based materials and removing moisture from porous materials such as drying of textiles, wood, paper, photographic film and ceramics. Other uses include oil extraction from tar sands, cross-linking polymers, vulcanization and casting. Drying of a porous medium with internal heat generation has been investigated[6]. With internal heat generation the mechanism of energy transfer is primarily internal heat generation and the mass transfer is primarily through a total pressure gradient established due to the rapid vapour generation inside the sample. Moreover when the sample is initially very wet and the pressure inside the sample rises rapidly, liquid may be removed from the sample under the influence of a total pressure gradient. The higher the initial moisture, the more influence this pressure gradient has on total mass removal[6].

The use of microwaves to sinter or join ceramics[7] is widely used in industry where the efficient production of high quality materials is important. A lot of research work involving the direct application of microwave heating effects in chemical synthesis has been done[8]. Mathematical models for predicting thermal runaway[5] and hot spots formation[9] in microwave heated ceramics have been developed. Subirats et al.[10] simulated microwave–sintering processes in large multi–mode microwave

cavities. Shorter chemical reaction times under microwave heating were observed by Breccia[11]. Medical applications of microwaves include thawing frozen tissue, warming blood, and tumor therapies[12]. Sullivan[13] gave an example of the successful application of microwaves in a hyperthermia treatment.

Perhaps the largest consumer of microwave power is the foods industry, where the applications include: baking , blanching, cooking, dehydration, pasteurization, and sterilization[14]. Microwave heating has the potential to improve processes such as vacuum and freeze drying (a widely used method for dehydration[15], employed in situations where it is important to keep dried materials at low temperatures[16]). An example of microwave thawing applications is given in[17].

In the future more use of home microwave ovens is expected with more product and package developments as well as industrial advancements for specific applications.

§1.1 Generation of microwave frequencies in microwave ovens

Microwaves are very short waves of electromagnetic energy that travel at the speed of light (186,282 miles per second). Microwaves used in microwave ovens are in the same family of frequencies as the signals used in radio and television broadcasting. Their frequency range is between 300 and 30000 MHz which corresponds to 1 meter to 1 millimeter in the wavelength (see Figure 1.1.1). Certain frequencies within this range are set aside by the International Telecommunications Union for Industrial, Scientific and Medical use. These so-called ISM bands are at 2450 MHz, 915 MHz, and a few other frequencies according to the country. By far the most common in Europe is 2450 MHz, which is the frequency at which most domestic microwave ovens operate. Microwaves are generated in a magnetron, then they are guided through a wave guide and delivered in a chamber (cavity). The heart of every microwave oven is the high voltage system. Its purpose is to generate microwave energy. The high-voltage components accomplish this by stepping up AC line voltage to high

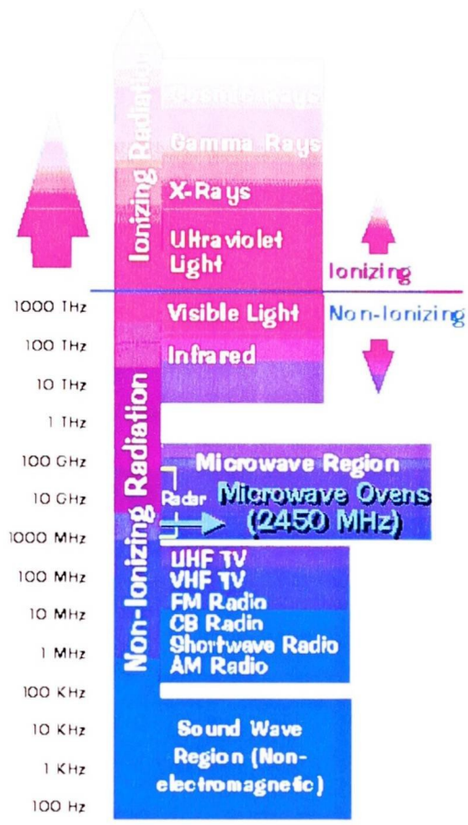

Figure 1.1.1: Frequency Spectrum

voltage, which is then changed to an even higher DC voltage. This DC power is then converted to the RF energy that cooks the food.

§1.1.1 Magnetron

The nucleus of the high-voltage system is the magnetron tube. The magnetron is a diode-type electron tube which is used to produce the required microwave energy. It is classed as a diode because it has no grid. A magnetic field imposed on the space between the anode (plate) and the cathode serves as the grid. The basic internal structure of a magnetron includes the anode, the filament/cathode, the antenna, and the magnets (see Figure 1.1.2). The theory of magnetron operation is based on the motion of electrons under the combined influence of electric and magnetic fields. The process starts when the cathode filament at the centre is heated by a low-voltage auxiliary electrical supply to reach its operating temperature. The increased temperature increases the molecular activity within the cathode and electrons are

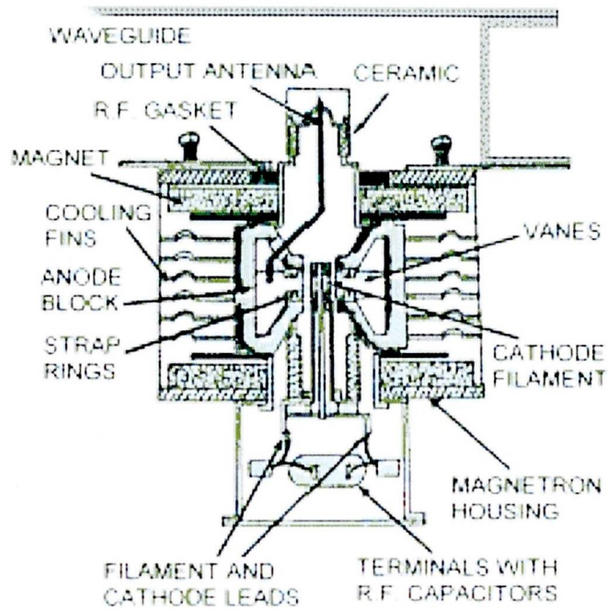

Figure 1.1.2: Sectional view of a typical magnetron

being released. For the tube to operate, electrons must flow from the cathode to the anode. There are two fundamental laws that govern their trajectory: 1. The force exerted by an electric field on an electron is proportional to the strength of the field. Electrons tend to move from a point of negative potential toward a positive potential. 2. The force exerted on an electron in a magnetic field is at right angles to both the field itself, and to the path of the electron. The direction of the force is such that the electron proceeds to the anode in a curve rather than a direct path. As the electrons pass by the anode, positive charges are produced. The alternate charging and discharging within the anode cavities produces an alternating current. The frequency of the alternating current is determined by the number and size of the cavities. Most magnetrons designed for domestic ovens operate at 2.45 GHz. The oscillations in the cavities are self-sustaining and excess microwave energy is extracted via a coupling loop, or antenna, transferring the microwave energy to the waveguide in the form of a transverse electromagnetic (TEM) wave.

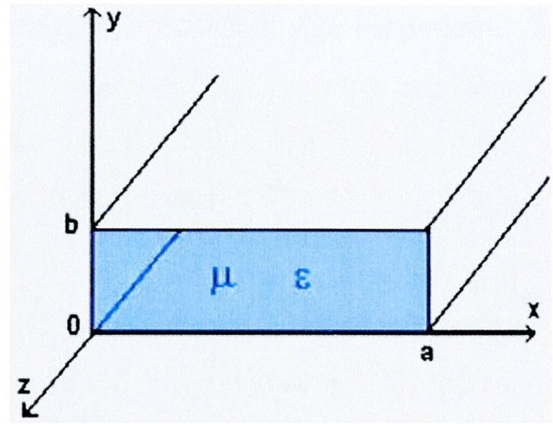

Figure 1.1.3: A cross section of a rectangular waveguide

§1.1.2 The Waveguide

Microwave energy cannot travel through a solid conductor, so the antenna radiates the RF power into a waveguide. The waveguide is a hollow metal tube (Fig. 1.1.3) that transports the microwave energy into the oven cavity. Metallic walls are nearly perfect electrical conductors, with low transmission losses. Most microwave ovens use a rectangular shaped waveguide, through which the waves of energy travel by reflecting from side to side in a zigzag pattern. A cross section of a rectangular waveguide with a material with permittivity ϵ and permeability μ is shown in Figure 1.1.3. The open end of the waveguide acts as a feed to the oven section of the system. Standing-wave patterns emerge within both the cavity and the waveguide, since energy not absorbed by the load is reflected by the metallic cavity walls, superimposing on itself. A portion of the energy will also reenter the waveguide, where it can damage the microwave generator if it returns too much energy.

§1.1.3 Microwave Applicators

An applicator is a general term for a device (i.e cavity) that transfers electromagnetic energy from the waveguide to the processed material. They can come in different sizes and shapes depending on the operating frequency and the properties, size and shape of the processed material. The most common applicators include single and

multi-mode cavities which are described in the subsequent sections.

§1.1.3.1 Multi-Mode Applicator

The simplest applicator is a rectangular metal (conductive) box that can accommodate the target load. When microwaves are launched into such a device via a waveguide, the waves undergo multiple reflections from the walls. The reflected waves interfere and, in so doing, establish a distribution of electrical field strengths within the internal space (including the load), that correspond to many different stable modes of propagation. This is why it is called a multi-mode applicator. The most common example of this device is a domestic microwave oven. The field distribution with a load contained in a multi-mode applicator depends not only on its dielectric loss, but also on its size and its location within the applicator. In this respect a multi-mode device is best suited to a load that is very lossy and which occupies a large volume (more than 50%) of the applicator. For low-medium loss materials occupying less than about 20% of the volume of the applicator, the temperature rise in the material, at best will be non uniform and, at worst, will contain potentially damaging "hot spots" that correspond with high local fields. By incorporating a mode stirrer (a rotating reflector) or continuously rotating the load on a turntable, temperature uniformity can be improved, albeit to a limited extent, by effectively smearing the electrical field distribution within the load. A major criticism of the use of a multi-mode oven for scientific study is that since the spatial distribution of field strength is unknown, the facility to generalize the results from a particular investigation is compromised, making it very difficult to effect a reliable scale-up. It is worth stressing that with all applicators, the important criterion is the electrical field within the sample. While it is possible to map the field distribution within an oven by moving, for example, a water load around it and recording the rate of rise of temperature, the results of such an exercise apply only to water. Once the target material is placed in the oven, the field distribution is changed completely. It is possible to calculate the field distribution within a loaded multi-mode cavity using Finite Difference Time Domain (FD-TD) procedures and, once such codes are

established and more generally available, the reservations over the use of such applicators may disappear. Over the past few years, interest in multi-mode ovens for low loss materials has increased as a result of the availability of multi-frequency sources. These allow a range of frequencies (typically, 2 GHz - 6 GHz) to be swept continuously so that the time averaged field pattern (and the resulting temperature rise in a load) is relatively uniform. At present the main disadvantages of such devices are that they are limited to relatively low power (100 W) and that they are expensive.

§1.1.3.2 Single Mode Applicator

By far the most efficient applicator is a single mode resonant cavity. Within such a cavity only one mode of propagation is permitted and hence the field pattern is defined in space, and the target load can be positioned accordingly. A single mode cavity may be cylindrical or rectangular. The simplest (and physically smallest) single mode cavity operates in the Transverse Magnetic mode (see Section 3.1), in which the electrical field strength is constant along length and varies with radius according to a combination of Bessel functions, such that the field is greatest at the axis. The radii of the cavity, load and die are determined by solving the electric and magnetic field equations within the cavity for the particular boundary conditions and mode of propagation. The resonance condition so derived defines these radii in terms of the dielectric constants of each of the components. A rectangular single-mode cavity consists of a length of waveguide which houses a non-contacting plunger that determines the effective cavity length. The mode of operation of such a device is, typically, TE_{10n} (see Section 3.1) with the target load positioned in a region of high field strength. The major limitation of this device is that the width of the load must be less than half a wavelength, otherwise the periodicity of the device will be reflected in a periodic heating pattern across the target. This can be overcome by moving the plunger in a reciprocating fashion so that the time-average field seen by the load is smeared.

§1.2 Factors affecting microwave heating

In many situations, the microwave heating process is observed to be tightly coupled and nonlinear. Small changes in the dielectric properties of the material can induce significant changes in the power distribution, and conversely, small changes in the power distribution impact substantially upon the temperature distribution[18]. The temperature and moisture distributions in a material during microwave heating are influenced by the interaction and absorption of radiation by the medium and the accompanying transport processes due to the dissipation of electrical energy into heat[1]. There are many factors that determine how the object will heat when subjected to microwave radiation: the geometry of the cavity in which heating takes place[12], microwave feed system design[19], the geometry and size of the object[20] and its electromagnetic and thermal parameters[1, 20].

The two most common methods used to improve the uniformity of heating are moving the food and using mode stirrers[21]. By moving the food (as it is done by the rotating the carousel in a domestic oven) all locations in the material can be made to encounter both the nodes and antinodes of the standing microwave pattern. A mode stirrer is generally a multi-blade rotating metallic reflector that continually changes the direction at which the microwaves are introduced into the cavity. This continuously perturbs the field distribution, which changes the locations of the nodes and antinodes and produce more uniform heating. The extent of uniformity provided by either moving the load or using the stirrers has been too complex to model mathematically.

The overall size of the food material influences its internal electrical field[21]. When the microwaves are randomly reflected from the metallic walls of the oven, they may be directed towards the food, but they may also reach another wall without encountering the food. Thus, a fraction of the microwave energy entering the oven is either dissipated by the walls or goes back to the magnetron. This causes the total amount of energy dissipated in the load (or energy coupled with the load) to

increase with load volumes. This changes the effective field intensity inside the food material as its size changes. Regular shapes heat more uniformly in a microwave oven. When the shape is irregular, the thin narrow parts tend to overcook and may be dried out by the time the thicker parts are done. This of course happens in conventional cooking but is less pronounced because cooking is slower. Where it is possible to control the shape, much more uniform results are obtained. Where this is not possible, thin parts may be covered with aluminum foil for a part of the cooking cycle. The same technique can be applied in protecting the wing tips and legs of roasting chickens and turkeys.

Packaging has direct effect on the electric field distribution and consequently on heating and moisture transport. Bows and Richardson[22], have examined the effects of food component layout and packaging materials (foil vs. plastic) on the microwave reheating characteristics of a standard experimental multicompartment food load. Edge over–heating can be avoided to some extent by using curved packaging and the heating effect can be modified by including susceptors or shielding inside the packaging. Susceptor materials are used to absorb microwave energy and provide localized heating. Internal heating is best achieved by 915 MHz oven and surface heating at 2450 MHz.

For microwave heating and drying, prediction of the heat and moisture transfer is essential for equipment design, process optimization and product quality. On-line measurement of temperature and moisture is difficult and time-consuming. The generalized mathematical model for the electromagnetic field distribution is given by Maxwell's equations[12]. These tell us how the electric and magnetic fields behave in space and time. The models for temperature and moisture distribution are respectively governed by the Fourier Heat Transfer Equation and the Continuity Equation (see Chapter 4).

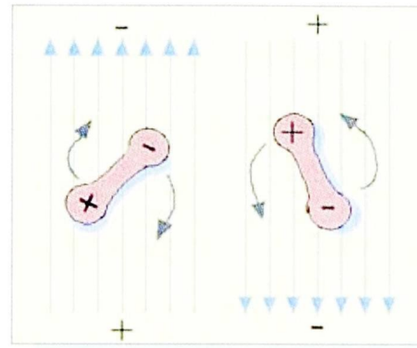

Figure 1.2.1: Dipole

§1.2.1 Microwave–Material Interactions

When an oscillating electrical field is applied to a polar dielectric, the dipoles within the material attempt to align themselves (polarize) with the field. The rate of change of polarization represents a displacement current in the dielectric and the product of this and the applied field gives the power generated as heat. Averaged over a cycle, the power "lost" in the material (ie dissipated as heat) depends on the phase angle between the applied field and the polarization. For most dielectrics the lag depends on the flexibility of the molecules that house the dipoles, and the randomization effect of temperature.

The dielectric heating mechanism relies on the fact that the water molecule is a dipole, i.e. has a positive and negative end. When a dipole is subjected to a microwave field with rapidly changing directions, the dipole tries to align itself with the direction of the electric field. This is not accomplished instantaneously, but requires some response time from the molecule to overcome the inertia and the intermolecular forces in the water. The electric field thus provides energy to the water molecule and makes them align with the microwave field. The energy is then lost by the random thermal motion of water molecules. When the water molecule realigns in the changing electric field, this energy is equivalent to the temperature increase. Heating results from the movement of the electrically charged ions within the food materials[23]. The heating of foods by microwaves is accomplished first by absorption

of microwave energy by water molecules, and the release of this energy as heat; and second by conductivity loses, due to ionic components of food materials. Thus, both the water content and the dissolved ion content are the main factors in the microwave heating of foods.

§1.2.1.1 Dielectric Properties

Dielectric properties of materials subjected to microwave heating play a key role in designing proper microwave applications. They are: permittivity ϵ, permeability μ and effective conductivity σ_{eff}. The permittivity measures the interaction of the material with the high frequency electric field and is defined by the following equation

$$\epsilon = \epsilon' - j\epsilon'' \tag{1.2.1}$$

where ϵ' is the dielectric constant, ϵ'' the dielectric loss factor and $j = \sqrt{-1}$. Alternatively, it can be expressed as

$$\epsilon = \epsilon_0(\epsilon_r' - j\epsilon_{eff}'') \tag{1.2.2}$$

where $\epsilon_r^{'}$ is the relative dielectric constant, $\epsilon_{eff}^{''}$ is the effective relative loss factor and $\epsilon_0 = 8.85 \times 10^{12}\, F/m$ is the permittivity of vacuum. $\epsilon_r^{'}$ is a measure of the polarizability of a material in the electric field, and $\epsilon_{eff}^{''}$ includes the loss factors which are relevant to high frequency heating.

The definition for both ϵ_r' and ϵ_{eff}'' can be derived using the constitutive equation for electric field. The constitutive equation that connects the electric field intensity $\mathbf{E}$, the electric flux density $\mathbf{D}$, and the electric polarization vector $\mathbf{P}$ is

$$\mathbf{D} = \epsilon_0\mathbf{E} + \mathbf{P} \tag{1.2.3}$$

This expression can be rewritten as

$$\mathbf{D} = \epsilon_0 \epsilon_r' \mathbf{E} \tag{1.2.4}$$

where

$$\epsilon_r' = 1 + \frac{P}{\epsilon_0 E} = 1 + \chi. \tag{1.2.5}$$

χ is the electric susceptibility and is always greater than zero (for air is equal to zero). The total current density for sinusoidal electric field variations can be expressed as

$$\mathbf{J} = \sigma_{eff}\mathbf{E} + j\omega\epsilon_0\epsilon_r'\mathbf{E} \tag{1.2.6}$$

Rearranging this equation yields:

$$\mathbf{J} = j\omega\epsilon_0(\epsilon_r' - j\frac{\sigma_{eff}}{\omega\epsilon_0})\mathbf{E} \tag{1.2.7}$$

Comparison of the previous two equations leads to an abridged form

$$\mathbf{J} = j\omega\epsilon_0\epsilon_c^\star\mathbf{E} \tag{1.2.8}$$

where

$$\epsilon_c^\star = \epsilon_r' - j\frac{\sigma_{eff}}{\omega\epsilon_0} = \epsilon_r' - j\epsilon_c'' \tag{1.2.9}$$

is the effective dielectric constant of the medium, where conduction effects dominate. Any other form of loss can be subsequently included as the imaginary part of the complex dielectric constant. When all types of losses are included, the equation 1.2.7 becomes

$$\mathbf{J} = j\omega\epsilon_0[\epsilon_r' - j(\epsilon'' + \frac{\sigma_{eff}}{\omega\epsilon_0})]\mathbf{E}. \tag{1.2.10}$$

We can define an effective loss factor ϵ_{eff}'' by grouping together all different forms of

losses

$$\epsilon''_{eff}(\omega) = \epsilon''(\omega) + \frac{\sigma}{\epsilon_0 \omega} = \epsilon''_a(\omega) + \epsilon''_d(\omega) + \epsilon''_e(\omega) + \epsilon''_s(\omega) + \frac{\sigma_{eff}}{\epsilon_0 \omega}. \tag{1.2.11}$$

The subscripts a, d, e and s refer to atomic, dipolar, electronic and space charge respectively. The last term in the equation accounts for the contribution due to conduction losses. The loss factors are frequency dependent which often simplifies the analysis because, in a given frequency band, one or two loss mechanisms dominate over the others. Another way of describing dielectric losses is the loss tangent, defined as the ratio of the effective loss factor to the dielectric constant

$$\tan \delta_{eff} = \frac{\epsilon''_{eff}}{\epsilon'_r} = \frac{\sigma_{eff}}{\omega \epsilon_0 \epsilon'_r} \tag{1.2.12}$$

where

$$\sigma_{eff} = \omega \epsilon_0 \epsilon''_{eff} = \sigma_s + \sigma_a \tag{1.2.13}$$

is the electric conductivity of the material for a given angular frequency ω. A static portion, σ_s, characterizes the free-electron conductive properties, and an alternating portion, σ_a, accounts for the rotation of dipoles as they try to align with the applied field as its polarity alternates [12].

Losses under the influence of the magnetic field can be described in a similar way to losses in electric materials. However, most materials used in microwave processing are magnetically transparent. The magnetic permeability in this work is assumed to have the value of the free space permeability $\mu_0 = 4\pi \times 10^{-7}\, H/m$.

Both ϵ'_r and ϵ''_{eff} are temperature, T, dependent and a number of investigations have been made in order to explain this behavior[1, 24]. In most cases, their values will increase as the material thaws after which, the values will decrease as the temperature increases as shown in Figure 1.2.2.

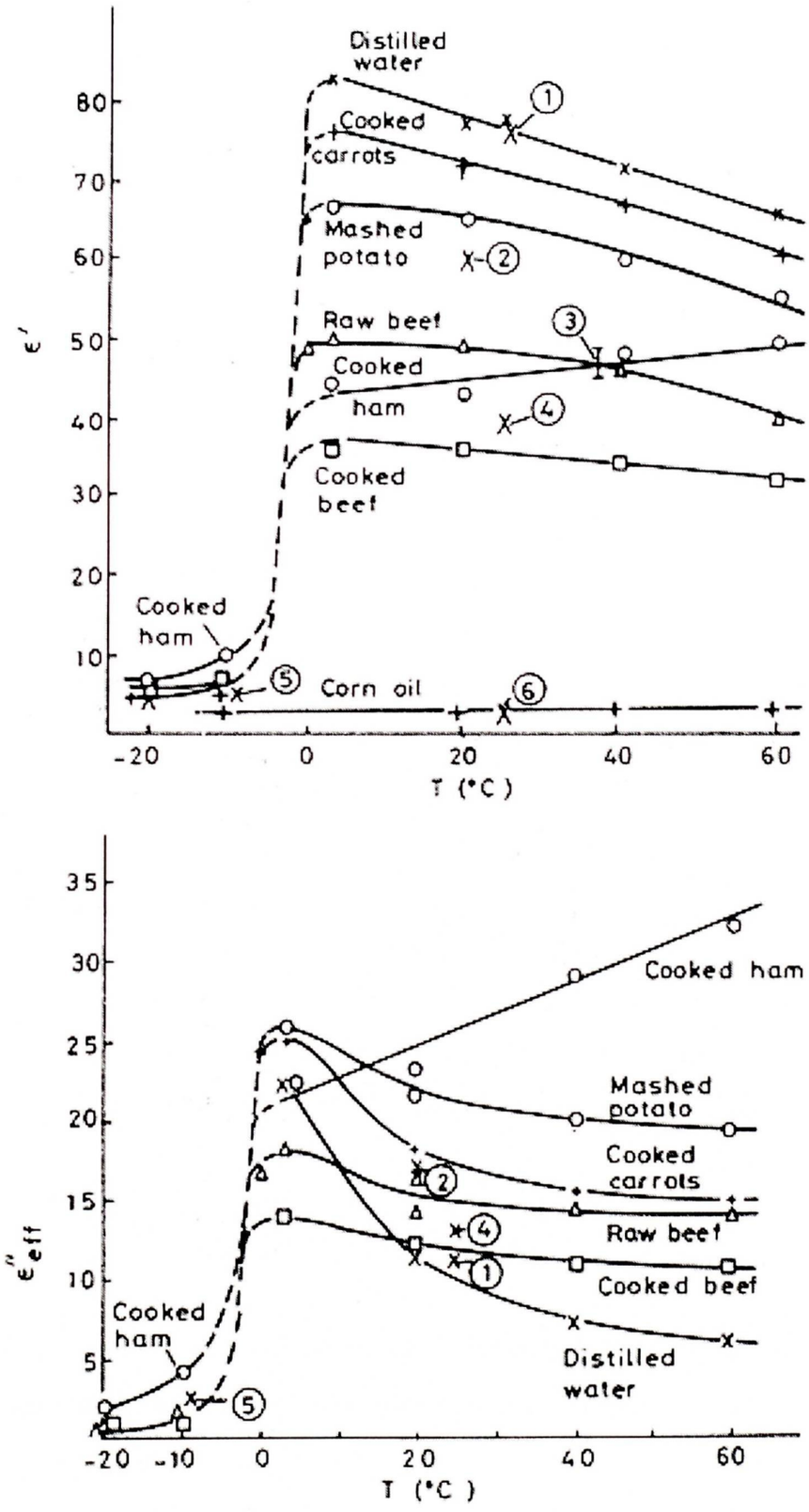

Figure 1.2.2: Dielectric properties for different materials as a function of temperature[1]

Since most foodstuffs contain an appreciable amount of water, the variation of $\epsilon_r^{'}$ and $\epsilon_{eff}^{''}$ with the moisture content plays an important role in the design of the microwave heating process. In a multiphase porous medium, if the temperature dependencies of all phases are known, the dependencies on moisture can be obtained from homogenization as described in Section 4.2.

§1.2.2 Energy penetration

A mathematical derivation of power penetration depth for lossy materials is available in the literature[25]. An electromagnetic wave impinging on a food surface will be exponentially attenuated, through absorption of energy accompanied by heat development, according to Lambert's law[24]. The electric strength E and power P_E can be shown to satisfy the following expressions

$$E = E_0 e^{-\overline{\alpha}\, x} \tag{1.2.14}$$

$$P_E = P_{E0} e^{-2\,\overline{\alpha}\, x} \tag{1.2.15}$$

where E_0 and P_{E0} refer to the conditions at the surface. The attenuation constant $\overline{\alpha}$, (also known as the skin depth[12]) is derived from the following expression[14]

$$d = \frac{\lambda_0}{2\pi(2\epsilon_r')^{1/2}} \left[\left(1 + (\frac{\epsilon_{eff}''}{\epsilon_r'})^2 \right)^{1/2} - 1 \right]^{-1/2}. \tag{1.2.16}$$

where λ_0 is the wavelength in free space. The penetration depth, d, defined as the distance from the surface where the power of the wave has decreased to $1/e$ of the surface value, is equal to

$$d = \frac{1}{2}\, \overline{\alpha}\ \ (m). \tag{1.2.17}$$

For materials with relatively low dielectric loss, it may be approximated by the expression[14]

$$d = \frac{\lambda_0}{2\pi\sqrt{\epsilon_r'} tan\,\delta_{eff}}. \tag{1.2.18}$$

The equation indicates that the penetration depth increases with decreasing frequency. In general the penetration depth at frequencies bellow 100 MHz presents little problems for penetration unless the loss factors are high[26]. At microwave frequencies the penetration depth is smaller. If the size of the material to be treated is many times larger than the penetration depth, then microwave heating may result in non-uniform temperature distributions[1].

The relative magnitudes of penetration depth and sample size determine the uniformity of heating. If the penetration depth is much larger than the sample size there will be little variation in the rate of heating between the surface and the interior of the sample and the resulting heating will be uniform[21]. When the penetration depth is much less than the sample size, heating will occur near the surface only.

§1.3 Outline of Contents

The present work considers microwave heating of a simple porous material[27, 28]. Dielectric properties are both temperature and moisture dependent. Maxwell's equations, which describe the electromagnetic distribution, are coupled to 3-D heat and mass transfer equations (used in the Finite Volume code PHOENICS[29]). Maxwell's equations are solved according to the Finite Difference Time domain technique. The coupled algorithms allows a complete mathematical description of the microwave heating phenomena within a porous biomaterial located in a microwave oven.

Relevant work available in literature is reviewed in Chapter 2. Chapter 3 covers the electromagnetic distribution in materials. It also describes the Yee's FD-TD discretisation of the Maxwell's equations. The chapter ends with the investigation

of material properties, the size and location of resonant behaviour in single and multi-mode cavities.

Chapter 4 introduces the heat and mass transfer in two-phase porous materials. It proceeds with the description of the Finite Volume method which is used to solve the equations involved. Finally, a simple 1-D example of freeze-drying is presented and investigates different aspects of the drying phenomenon.

The solution technique is given in Chapter 5. The algorithm that couples the electromagnetic solver with the heat and mass transfer solver is presented. It also gives details on the mapping between the FD-TD and FV meshes as well as stability and computational considerations.

Chapters 6 and 7 present 2-D and 3-D computational results, respectively. They contain validation examples for the Yee's scheme on both structured uniform and non-uniform meshes. Chapter 6 also contains a validation of the author's coded 3-D FD-TD algorithm against other numerical results available in the literature. Chapter 5 has a comparison between 2-D temperature distribution obtained using the author's code and the results obtained using the commercial code PHOENICS. A validation of a 3-D temperature distribution against experimental measurements is given in Chapter 6. Fully coupled 2-D and 3-D results are shown and several heating aspects are investigated.

The concluding Chapter 8 suggests further advances in these methods for the future.

CHAPTER

TWO

Literature Review

As shown in the previous section, the microwave process is a very complex one. Prediction of heating and moisture patterns can only really be achieved numerically. There is no realistic analytical solution. Any of the factors that influence the heating can easily be changed in a computer program so that the optimal configuration can quickly be found before anything is built. Computer modelling and numerical techniques provide an attractive, accurate, fast and effective means for calculating power deposition patterns, temperature and moisture distributions during and after microwave processing. Besides giving information on heating rates and patterns, numerical modelling and computational techniques may provide valuable information that may result in better control and optimization of the heating process. These calculations can be made for a wide variety of heating techniques (single and multi mode cavities and other types of devices) and more cost effectively for a wide variety of heating patterns, sample geometries, and sample–insulation combinations. Computer modelling and computational techniques can also be used to calculate temperature distribution and heating patterns in processed samples and may help identify critical parameters in controlling heating processes. Iskander[30] gave a review of computational techniques suitable for quantifying microwave interactions with materials.

§2.1 Electromagnetic modelling

One of the major problems associated with microwave heating and drying is the spatial non-uniformity of the microwave heating strength, responsible for localized hot or cold spots in the applicators[31]. To overcome or minimize these problems, knowledge of the microwave field structure and the power distribution inside the applicator is essential. A considerable research effort has been concentrated on these problems. Because of the complexity involved in the mathematical calculation of the microwave field and power distribution inside applicators, most of the work in the literature concerns experimental measurements, analytical solutions for some simple geometry applicators or a microwave power distribution based on Lambert's law (see Equations 1.2.14 and 1.2.15). The studies based on Lambert's law[24,32] have assumed that the incident power at the surface of the loading material is uniform and normal to the surface and attenuated exponentially in the direction of propagation.

The power absorbed per unit volume is valid for semi-infinite media and is usually referred as the Lambert law limit[24]. It requires an estimate of the power transmitted to the surface. This is obtained from calorimetric measurements or it is used as an ad hoc parameter that matches experimental profiles with the model. Alternatively, if the power transmitted to the surface is the incident flux then Lambert's law must be modified to account for the decrease in power, due to reflection at the surface of the sample.

Ayappa et al.[24] made a comparison between models of microwave heating based on a Lambert's law formulation and models in which the power is computed from Maxwell's equations. Lambert's law is strictly used for semi-infinite samples. It determines the conditions of the approximate applicability for finite slabs and was compared with the microwave heating predicted from Maxwell's equations. They found that the critical slab thickness $L_{crit}(m)$ above which the Lambert's law limit

is valid can be estimated from

$$L_{crit} = 2.7d^{-1} - 0.08\,. \tag{2.1.1}$$

This approach has been applied to the modelling of heat transfer of dielectrically heated solid foods by Chen et al.[32] and Lin at al[33].

However, it is very difficult to calculate the field structure in a general microwave heating applicator by these methods. For a general applicator where the load may have arbitrary geometries and the dielectric properties may vary with space, there is usually no alternative other than to resort to a numerical method. In spite of the advantages made in numerical methods concerning this problem, limited progress has been made.

Time domain methods are based on the differential form of Maxwell's equations in time domain. There are several numerical methods in use as time domain: Transmission-Line Modelling method[34], Edge Elements[35], Method of Lines[25], Co-Volume method[36] and Finite-Difference Time-Domain Method[37] (FD-TD). They are implemented in an iterative process following the time evolution, initiated via an excitation vector[38].

The Finite Element Method (FEM) provides a powerful tool, being easily applicable to structures with arbitrary geometries, non-linear behaviours (in time domain), anisotropic and lossy materials. It involves sparse matrix inversion and very simple boundary conditions in closed structures. Important contributions on microwave heating have been made using the FEM by Jia[39] who calculated the power distribution dissipated in the dielectric material in multimode rectangular cavity excited by waveguides. The method was verified by analyzing a simple loaded problem which can be solved analytically. Important results on microwave power disrtibution in multimode applicators using Finite-Element Time-Domain (FE-TD) analysis were presented by Dibben[35, 40]. The FE-TD method can account for complex geometries and the physical behaviour of media, but some adequate techniques are still

needed to reduce computation time due to the matrices inversion needed at each time step[38].

The Co-Volume method is a generalization of FD-TD to unstructured meshes. Its accuracy has not been established but its mathematical structure is very similar to edge elements and it is very likely to have similar (more likely worse) accuracy on a given mesh. FD-TD gives a superior accuracy for the same number of degrees of freedom when structured meshes are acceptable (see also[41,42]). A number of authors[2,43,44] have investigated the microwave power distribution in microwave enclosures. Liu at al.[2] developed a 3-D computer algorithm for calculating the power distribution inside a lossy material in a rectangular cavity. The technique will be explained in detail in Chapter 3.

In cases of microwave devices where a rigorous description of the electromagnetic field propagation is important and the evolution during transience is not, frequency-domain methods are an ideal tool for such analysis. The most popular are the Finite Element Method [45] and the global integral equation techniques [38], namely Boundary Element Method (B.E.M) and Volume Integral Method (V.I.M). The B.E.M[46] considers linear behaviour while the V.I.M[47] can account for nonlinearity. These methods satisfy the radiation condition and do not need absorbing boundary conditions for open boundary problems. However, they need a full matrix inversion.

For loads with low permittivity the frequency domain works very well. However as the permittivity of the load increases the method can become very slow[45]. For this type of problem the time domain method provides an alternative that allows a much quicker solution and overcomes the problems of ill-conditioning[45]. The time domain is also advantageous when solutions within a range of different frequencies need to be obtained with a single calculation[40].

For dispersive materials a Frequency–Dependent Finite–Difference Time–Domain ($(FD)^2TD$) formulation has been used[48,49]. The method was applied to obtain

a broad band frequency information in 3-D biological applications[13]. Microwave heating of dispersive media was also analyzed by Kriegsmann[50] using this method.

Even though all of the above mentioned algorithms provide a useful tool for understanding the microwave power distribution, their use for realistic simulations is limited due to the fact that almost all of them assume constant dielectric properties.

§2.2 Heat and mass transfer during microwave heating

In the previous section computational techniques for modelling the power deposition in materials using microwaves were described. Of ultimate interest, however, is the calculation of the the temperature and moisture distribution in the heated samples. These calculations require knowledge of the microwave power deposition pattern in the object and also the nature and distribution of the various heat exchange mechanisms that occur during heating. Microwave heating involves the transformation of electromagnetic energy into heat[1]. Microwave heating involves both heat and mass transfer. The relevant references are reviewed in this section. The numerical treatment of the Heat Transfer Equation (HTE)[51] will be described in Chapter 4.

Ohlsson and Bengston[14] used the finite difference technique to study heat transfer phenomena in a slab of salted ham and beef subjected to microwave heating. A general agreement between simulated and measured temperature profiles was found for temperatures approaching 100^oC.

A FEM based model was used by Chen et al[52]. A non linear heat generation term was linearized and incorporated into an axisymmetric finite element model for the analysis of the temperature distribution within a microwaved material. The FEM was also used to model the microwave thawing of pure water and $0.1NaCl$ cylinders[17]. They also observed the non-uniformity of heating. The heating uniformity in a microwave oven can be improved either by rotating the food or by mode stirring.

The simulation of heat transfer into a canned corn starch dispersion subjected to axial rotation was also studied[53].

Datta and Liu[54] compared the temperature history of solids and liquids for microwave and conventional heating. They investigated the uniformity of heating inside the material and the product degradation. Advantages and disadvantages for each method were outlined.

The classical mass transfer equation is described by Fick's law[23]. It assumes that the driving force during moisture migration is the moisture gradient and constant moisture diffusivity. Therefore, heat and mass transfer equations can be solved separately i.e. Fourier's equation for heat transfer and Fick's equation for mass transfer. This method was first applied by Luikov[55]. These equations were simplified and could be solved analytically.

However, because of the complexity of coupled heat and mass transfer equations, solutions must generally be obtained by numerical techniques. Wang et al.[56] described a 1-D sublimation–condensation model for freeze drying of unsaturated porous media. They assumed constant electromagnetic power and studied microwave freeze drying process numerically for different operating conditions including electric field strength, sample thickness and vacuum pressure.

A 2-D mathematical model for drying of porous material was developed by Lian et al[57]. The moisture transfer is a combination of the liquid water and vapour water transfer that takes place simultaneously. Heat transfer was based on the energy conservation of the sensible heat, latent heat and source heat of microwave power. The equations were coupled and solved using finite element method and were applied to simulate the heat and mass transfer of a concentrated water soluble paste. The electric field strength was assumed to be uniform around the surface of the loaded material and decayed exponentially with increasing depth from the surface of the material according to Lambert's law.

A three–dimensional FEM to predict temperature and moisture distributions during microwave heating of a potato sample for both slab and cylindrical geometries is available[23, 58]. Lambert's law was again used to represent the electromagnetic power absorbed by the food material. Good agreement between measured and numerical results for the temperature and moisture content on the material's surface were obtained.

A number of papers mainly dealing with moisture distribution in microwave heating of foods were published by Ni and Datta[59–61]. A very detailed 1-D dimensional multi–phase porous media model[59] predicting moisture transport during intensive microwave heating of wet bio–materials was proposed. They observed the internal pressure gradients in low and high moisture materials. The pressure gradients arise from internal heating and vapourization and significantly enhanced moisture transport. Even moderate internal pressure gradients in low moisture materials are shown to cause moisture to move towards the surface, leading to a soggy surface. A strong internal pressure gradient in high moisture materials led to a fully saturated surface and very high moisture loss by liquid outflow at the surface. They suggested additional hot air heating of the surface to increase evaporation in those regions. Lambert's law was used for microwave power estimation. The effect of food structure, initial moisture level, and different surface conditions on moisture distribution and loss in microwave heating of foods were investigated by the same authors[62]. The approach was applied to simulate the moisture, oil and energy transport during deep–fat frying of fat materials[61].

One of the most comprehensive drying models was proposed by Perre and Turner[63]. The 3-D algorithm was able to deal with the heat and mass transfer in porous media. The most important physical phenomena treated in the formulation included capillary and convective liquid flow, bound and gaseous diffusion and convective gaseous migration, thermal conductivity and heat required for evaporation. The 3-D heat and mass transfer equations as well as Darcy's law were solved using the control volume method.

§2.3 Coupled Algorithms

As it can be seen from the previous two sections, most of the published work has considered either the detailed electromagnetic field distribution in microwave ovens with given effective conductivities (e.g.[64]) or detailed heat and mass transfer (usually diffusion driven but sometimes pressure driven) in biomaterials with assumed electromagnetic field distributions (e.g.[58,65]). This results in a linear problem, decoupling the wave propagation from the accompanying heat and mass transfers and allowing each phenomenon to be analyzed independently. However electric permittivities and effective conductivities are highly sensitive to moisture concentration so that moisture transport has a direct effect on the microwave power distribution and a fully coupled approach is essential to further progress.

A coupled electromagnetic and thermal analysis can account for the interdependence in time of constitutive parameters and solution. The degree of coupling between the two phenomena depends on the nature of the materials being processed. In most cases electromagnetic time–constant is much shorter compared to the thermal one, and hence the coupling is weak and the solutions of the respective phenomena can be achieved in a sequential manner; the solution results of one phenomenon become the input of the second (Razek[38]).

As it was described in the previous section, dielectric properties of most bio-materials vary with temperature (Ayappa et al.[66]). Transient temperature profiles in multilayer slabs were predicted, by simultaneously solving Maxwell's equations with a Galerkin Finite element method. The method was illustrated with applications involving the heating of food and polymers with microwaves. Dielectric properties are function of temperature.

Torres at al.[67] proposed a 3-D algorithm that couples electromagnetic computation (based on the $((FD)^2TD)$ method) with the heat transfer via temperature dependent dielectric properties (a very simple explicit finite–difference scheme was used for the

HTE with no cooling effects assumed). A time scaling factor was introduced to make up for different time steps of both algorithms. The results were partially validated against experimental data and satisfactory agreement was shown. The model was able to predict the locations of hot spots within the material.

Experimental comparison for microwave–thermal model was carried out by Ma et al[4]. They used a FD-TD method to solve both Maxwell's equations and an explicit FV scheme for the HTE. The results were obtained for a phantom gel contained in a container and were validated against experimental measurements. The numerical results proved useful for predicting the locations of hot spots. However, for better agreement mass transfer has to be incorporated into the model.

Liu at al.[68] coupled Maxwell's electromagnetic equations to the heat transfer equations and solved them numerically in order to simulate the microwave heating of a polymer material inside a ridge waveguide. The electromagnetic fields and power distribution in the polymer material within the waveguide are predicted by means of the FD-TD technique. The FD-TD scheme was modified for the field component adjacent to the curved surface of the ridge waveguide by applying the contour path technique. Implicit finite difference scheme was used to discretize the heat equation. The numerical results obtained were in good agreement with experimental results up to the temperature of 150^oC. Properties were assumed to be temperature dependent.

Zhao[18] proposed a 3-D mathematical model for microwave heating, together with an algorithm for coupling electromagnetic and thermal computational codes. The method was applied to microwave heating of wood and was able to predict the temperature inside the material accurately. The model couples a Finite Volume Time Domain Algorithm (FV-TD) for resolving Maxwell's equation on arbitrarily shaped domains, together with an algorithm for determining the thermal distribution within the wood sample based on an unstructured mesh finite volume method .

In all the above reviewed works, the transfer of mass is assumed to be unimpor-

tant. However, if significant drying occurs during heating, mass transfer must be accounted for. Excellent research into drying of wood was carried out by Perre[36]. The model couples a two-dimensional set of equations to describe the drying process (control volume technique[51]) with a complete three-dimensional solution of Maxwell's equations within a rectangular waveguide in the time domain(FD-TD). Dielectric properties were assumed to vary with both moisture content and the drying process. Match between experimental and theoretical results was reasonable. The model captures the overall drying behavior reasonably well, and was able to predict the occurrence of hot spots and thermal runaway within the material. However, there is a need for fully coupled 3-D model, since the impact of 2-D heat and mass transfer model with 3-D electromagnetic model is unclear.

CHAPTER

THREE

Electromagnetic fields in microwave enclosures

The intensity of the electromagnetic field and its distribution are key factors that determine microwave absorption. They are influenced by material properties, size, cavity dimensions and shape operating conditions. In order to examine the influence of any of those factors, it is essential to understand the basic laws governing electromagnetic wave propagation, i.e *Maxwell's* equations. Application of the theoretical concepts contained in these relations are critical to good design and operation of practical microwave processing systems.

In this section the general form of Maxwell's equations given. They are described along with the accompanying boundary conditions. They are solved in the time domain using an algorithm, first proposed by Yee[37]. The algorithm is based on the Finite-Difference Time-Domain (FD-TD) method[2, 43, 44] and is easily adapted for one-, two- and three-dimensional problems. The mathematical model which is presented in this section considers the field distribution in the input section of the waveguide and in the entire cavity.

The resonant behaviour in single and multimode cavities[69] illustrates the implementation of the explicit finite difference scheme. Simulations show the influence of working frequency, sample size and dielectric properties.

§3.1 Maxwell's equations

The distribution of electromagnetic field in space and time is governed by Maxwell's equations[37]. They describe the interaction between electric charges, at rest and in motion; the consequences of these are electric currents, electric and magnetic fields. The differential form of Maxwell's equations can be expressed in terms of the electric field intensity $\mathbf{E}$, electric flux density $\mathbf{D}$, magnetic field intensity $\mathbf{H}$, magnetic flux density $\mathbf{B}$, and conduction electric current density $\mathbf{J}$

$$\frac{\partial \mathbf{B}}{\partial t} = -\nabla \times \mathbf{E} \tag{3.1.1}$$

$$\frac{\partial \mathbf{D}}{\partial t} = \nabla \times \mathbf{H} - \mathbf{J} \tag{3.1.2}$$

$$\nabla \cdot \mathbf{D} = \rho \tag{3.1.3}$$

$$\nabla \cdot \mathbf{B} = 0. \tag{3.1.4}$$

To these differential equations are added the constitutive relations

$$\mathbf{D} = \epsilon \mathbf{E} \tag{3.1.5}$$

$$\mathbf{B} = \mu \mathbf{H} \tag{3.1.6}$$

$$\mathbf{J} = \sigma_{eff} \mathbf{E} \tag{3.1.7}$$

Assuming that the material parameters μ, ϵ and σ_{eff} are independent of time, in rectangular coordinate systems (x, y, z), the curl equations can be expressed as a set

of six coupled scalar partial differential equations

$$\frac{\partial H_x}{\partial t} = \frac{1}{\mu}(\frac{\partial E_y}{\partial z} - \frac{\partial E_z}{\partial y}) \tag{3.1.8}$$

$$\frac{\partial H_y}{\partial t} = \frac{1}{\mu}(\frac{\partial E_z}{\partial x} - \frac{\partial E_x}{\partial z}) \tag{3.1.9}$$

$$\frac{\partial H_z}{\partial t} = \frac{1}{\mu}(\frac{\partial E_x}{\partial y} - \frac{\partial E_y}{\partial x}) \tag{3.1.10}$$

$$\frac{\partial E_x}{\partial t} = \frac{1}{\epsilon_0 \epsilon_r'}(\frac{\partial H_z}{\partial y} - \frac{\partial H_y}{\partial z} - \sigma_{eff} E_x) \tag{3.1.11}$$

$$\frac{\partial E_y}{\partial t} = \frac{1}{\epsilon_0 \epsilon_r'}(\frac{\partial H_x}{\partial z} - \frac{\partial H_z}{\partial x} - \sigma_{eff} E_y) \tag{3.1.12}$$

$$\frac{\partial E_z}{\partial t} = \frac{1}{\epsilon_0 \epsilon_r'}(\frac{\partial H_y}{\partial x} - \frac{\partial H_x}{\partial y} - \sigma_{eff} E_z). \tag{3.1.13}$$

Assuming a plane-polarized radiation source, Maxwell's equations decouple into one of two polarization states: Transverse Electric mode (TE)

$$\mathbf{E} = (0, 0, E_z), \quad \mathbf{H} = (H_x, H_y, 0) \tag{3.1.14}$$

and Transverse Magnetic mode (TM)

$$\mathbf{E} = (E_x, E_y, 0), \quad \mathbf{H} = (0, 0, H_z) \tag{3.1.15}$$

where

$$\mathbf{E} = \mathbf{E}(x, y, z, t), \quad \mathbf{H} = \mathbf{H}(x, y, z, t). \tag{3.1.16}$$

For two-dimensional problems, assumed uniform and infinite in the z-direction, the TE equations reduce to:

$$\frac{\partial E_z}{\partial t} = \frac{1}{\epsilon_0 \epsilon_r'}\left(\frac{\partial H_y}{\partial x} - \frac{\partial H_x}{\partial y} - \sigma_{eff} E_z\right) \tag{3.1.17}$$

$$\frac{\partial H_x}{\partial t} = -\frac{1}{\mu}\frac{\partial E_z}{\partial y} \tag{3.1.18}$$

$$\frac{\partial H_y}{\partial t} = \frac{1}{\mu}\frac{\partial E_z}{\partial x} \tag{3.1.19}$$

and the TM equations are expressed as

$$\frac{\partial H_z}{\partial t} = \frac{1}{\mu}\left(\frac{\partial E_x}{\partial y} - \frac{\partial E_y}{\partial x}\right) \tag{3.1.20}$$

$$\frac{\partial E_x}{\partial t} = \frac{1}{\epsilon_0 \epsilon_r'}\frac{\partial H_z}{\partial y} \tag{3.1.21}$$

$$\frac{\partial E_y}{\partial t} = -\frac{1}{\epsilon_0 \epsilon_r'}\left(\frac{\partial H_z}{\partial x} + \sigma_{eff} E_y\right) \tag{3.1.22}$$

The TM equations contain only the electric field in the x, y-plane along with the induced magnetic field and the TE equations contain only the magnetic field in the x, y-plane along with the induced electric field. In this and following chapters only TE polarization is considered, although TM polarization could just as easily be simulated.

§3.2 Yee's discretisation scheme

The fastest and most popular method for solving the Maxwell's equations is the FD-TD method. The method as used in electromagnetics was firstly described

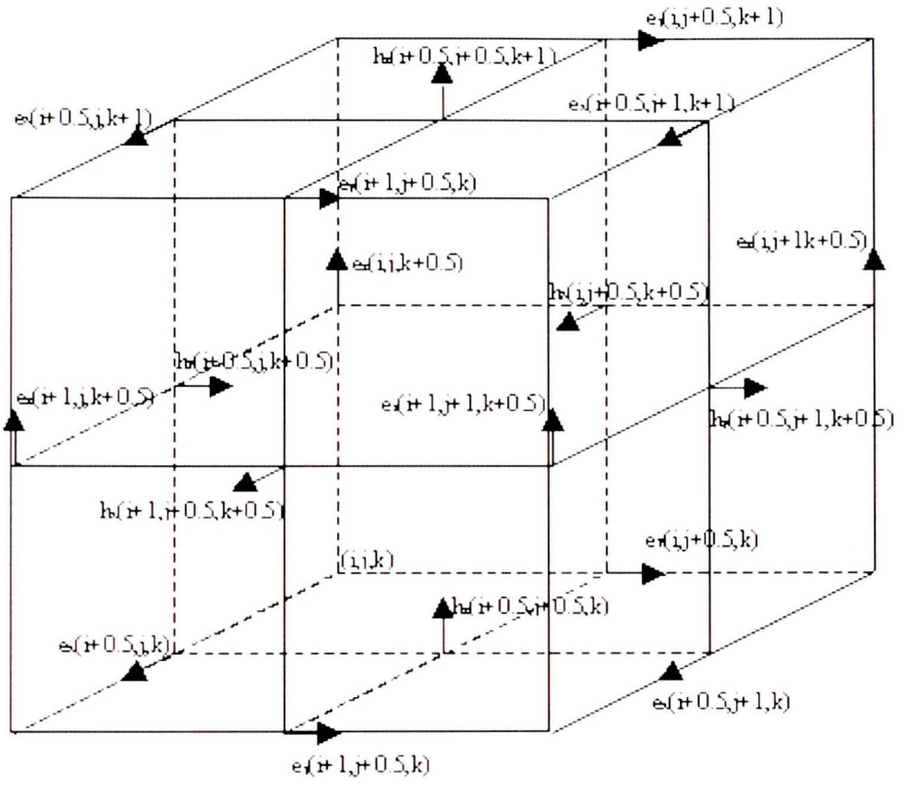

Figure 3.2.1: Yee's scheme nodal description

by Yee[37]. The Yee's scheme proceeds by segmenting the volume into a three-dimensional mesh composed of a number of finite volumes, as shown in Fig. 3.2.1. It makes use of finite difference approximations to electric and magnetic fields components, that are staggered both in time and space. **E** and **H** field components are positioned at half-step intervals around unit volumes and they are evaluated at alternate half-time steps, effectively giving centered difference expressions for both time and space derivatives.

Following Yee's notation, we denote a space point in a cubic lattice as

$$(i, j, k) = (i\Delta x, j\Delta y, k\Delta z) \tag{3.2.1}$$

and any function of time and space evaluated at each point as

$$F^n(i, j, k) = F(i\Delta x, j\Delta y, k\Delta z, n\Delta t) \tag{3.2.2}$$

where Δx, Δy, Δz are the space increments (in the case where they are the same

δ will be used), Δt is the time increment, and i, j, k and n are integers. Yee used centered finite-difference expressions for the space and time derivatives that are both simply programmed and second order accurate in δ and in Δt, respectively:

$$\frac{\partial F^n(i,j,k)}{\partial x} = \frac{F^n(i+\frac{1}{2},j,k) - F^n(i-\frac{1}{2},j,k)}{\delta} + O(\Delta x^2) \tag{3.2.3}$$

$$\frac{\partial F^n(i,j,k)}{\partial t} = \frac{F^{n+\frac{1}{2}}(i,j,k) - F^{n-\frac{1}{2}}(i,j,k)}{\Delta t} + O(\Delta t^2) \tag{3.2.4}$$

To achieve the accuracy of Equation 3.2.3, and to realize all of the space derivatives of Equation 3.1.13, Yee positioned components of **E** and **H** about a unit cell of the lattice as shown in Figure 3.2.1. To achieve the accuracy of Equation 3.2.4, he evaluated **E** and **H** at alternate half time steps.

Many electromagnetic interaction problems involve nonpermeable media and can be approached using a fixed time step and space increment. For such problems, the quantity $\Delta t/\mu(i,j,k)\delta$ is constant for all (i,j,k) of the lattice, and the Yee's system of equations can be simplified to reduce computer time in the following manner. The following constants can be defined:

$$R = \frac{\Delta t}{2\epsilon_0}, \tag{3.2.5}$$

$$R_a = \frac{(\Delta t)^2}{\delta^2 \mu_0 \epsilon_0}, \tag{3.2.6}$$

$$R_b = \frac{\Delta t}{\mu_0 \delta}, \tag{3.2.7}$$

$$C_a(i,j,k) = \frac{1 - \frac{R\sigma_{eff}(i,j,k)}{\epsilon_r'(i,j,k)}}{1 + \frac{R\sigma_{eff}(i,j,k)}{\epsilon_r'(i,j,k)}}, \tag{3.2.8}$$

$$C_b(i,j,k) = \frac{R_a}{\epsilon_r'(i,j,k) + R\sigma_{eff}(i,j,k)}. \tag{3.2.9}$$

We also define a proportional electric–field vector

$$\tilde{E} = R_b\mathbf{E}. \tag{3.2.10}$$

Using the definitions of Equations 3.2.5 -3.2.9 and 3.2.10, we reformulate Yee's finite-difference approximation to equations 3.1.8 - 3.1.13 as

$$\begin{aligned} H_x^{n+\frac{1}{2}}(i,j+\frac{1}{2},k+\frac{1}{2}) &= H_x^{n-\frac{1}{2}}(i,j+\frac{1}{2},k+\frac{1}{2}) \\ &+ \tilde{E}_y^n(i,j+\frac{1}{2},k+1) - \tilde{E}_y^n(i,j+\frac{1}{2},k) \\ &- \tilde{E}_z^n(i,j+1,k+\frac{1}{2}) + \tilde{E}_z^n(i,j,k+\frac{1}{2}) \end{aligned} \tag{3.2.11}$$

$$\begin{aligned} H_y^{n+\frac{1}{2}}(i+\frac{1}{2},j,k+\frac{1}{2}) &= H_y^{n-\frac{1}{2}}(i+\frac{1}{2},j,k+\frac{1}{2}) \\ &+ \tilde{E}_z^n(i+1,j,k+\frac{1}{2}) - \tilde{E}_z^n(i,j,k+\frac{1}{2}) \\ &- \tilde{E}_x^n(i+\frac{1}{2},j,k+1) + \tilde{E}_x^n(i+\frac{1}{2},j,k) \end{aligned} \tag{3.2.12}$$

$$\begin{aligned} H_z^{n+\frac{1}{2}}(i+\frac{1}{2},j+\frac{1}{2},k) &= H_z^{n-\frac{1}{2}}(i+\frac{1}{2},j+\frac{1}{2},k) \\ &+ \tilde{E}_x^n(i+\frac{1}{2},j+1,k) - \tilde{E}_x^n(i+\frac{1}{2},j,k) \\ &- \tilde{E}_y^n(i+1,j+\frac{1}{2},k) + \tilde{E}_y^n(i,j+\frac{1}{2},k) \end{aligned} \tag{3.2.13}$$

$$\begin{aligned} \tilde{E}_x^{n+1}(i+\frac{1}{2},j,k) &= C_a(i+\frac{1}{2},j,k)\tilde{E}_x^n(i+\frac{1}{2},j,k) \\ &+ C_b(i+\frac{1}{2},j,k)[H_z^{n+\frac{1}{2}}(i+\frac{1}{2},j+\frac{1}{2},k) - H_z^{n+\frac{1}{2}}(i+\frac{1}{2},j-\frac{1}{2},k) \\ &+ H_y^{n+\frac{1}{2}}(i+\frac{1}{2},j,k-\frac{1}{2}) - H_y^{n+\frac{1}{2}}(i+\frac{1}{2},j,k+\frac{1}{2})] \end{aligned} \tag{3.2.14}$$

$$\begin{aligned}\tilde{E}_y^{n+1}(i,j+\frac{1}{2},k) &= C_a(i,j+\frac{1}{2},k)\tilde{E}_x^n(i,j+\frac{1}{2},k) \\ &+ C_b(i,j+\frac{1}{2},k)[H_x^{n+\frac{1}{2}}(i,j+\frac{1}{2},k+\frac{1}{2}) - H_x^{n+\frac{1}{2}}(i,j+\frac{1}{2},k-\frac{1}{2}) \\ &+ H_z^{n+\frac{1}{2}}(i-\frac{1}{2},j+\frac{1}{2},k) - H_z^{n+\frac{1}{2}}(i+\frac{1}{2},j+\frac{1}{2},k)]\end{aligned} \tag{3.2.15}$$

$$\begin{aligned}\tilde{E}_z^{n+1}(i,j,k+\frac{1}{2}) &= C_a(i,j,k+\frac{1}{2})\tilde{E}_z^n(i,j,k+\frac{1}{2}) \\ &+ C_b(i,j,k+\frac{1}{2})[H_y^{n+\frac{1}{2}}(i+\frac{1}{2},j,k+\frac{1}{2}) - H_y^{n+\frac{1}{2}}(i-\frac{1}{2},j,k+\frac{1}{2}) \\ &+ H_x^{n+\frac{1}{2}}(i,j-\frac{1}{2},k+\frac{1}{2}) - H_x^{n+\frac{1}{2}}(i,j+\frac{1}{2},k+\frac{1}{2})].\end{aligned} \tag{3.2.16}$$

This reformulation eliminates three multiplications needed by Yee to compute H_x, H_y, and H_z. Further, it eliminates the need for computer storage of separate ϵ_r' and σ_{eff} arrays. Changes in ϵ_r' and σ_{eff} involve only the recalculation of $C_a(i,j,k)$ and $C_b(i,j,k)$.

With the system of Equations 3.2.11-3.2.16, the value of a field component at any lattice point depends only on its previous value and the previous value of the components of the other field vector at adjacent points. Therefore, at any given time step, the computation of a field vector may proceed either one point at a time, or, with a parallel processing computer, at many points at a time.

This scheme is second order accurate in both time and space on uniform and non–uniform meshes[70], and can be locally refined[41] without significant loss of accuracy. The use of (semi)–structured meshes ensures optimally fast computations for the most time–consuming component of the overall calculations and is sufficient for our geometric modelling requirements.

Over the years it has been used and improved by many authors[2,43,44]. It has been used frequently for a wide range of applications, from the analysis of microstrip antennas[71] and scattering from guided missiles[44] to hyperthermia in medicine[72], sintering of ceramics[10,30] and other heating applications[4]. Sundberg at al.[73]

showed some aspects of the use of the FD-TD method for analysis of industrial microwave tunnel ovens.

Domestic microwaves are primarily rectangular enclosures so structured meshes can provide an adequate approximation to the microwave cavity geometry[4]. In this application the computational domain is physically enclosed by the conducting walls of the cavity. Hence, most of the computational difficulties and the inaccuracies encountered due to utilization of the artificial absorbing boundary conditions are eliminated and replaced by "solid", well-defined boundary conditions of perfectly conducting walls[30]. FD-TD approach is particularly effective in the calculation of large three dimensional structures because, for a given cell size, computation and storage requirements increase only linearly with the number of cells[74]. The FD-TD method involves the development of the steady-state solution of the field quantities by time-integration.

§3.3 Incident wave

The formulation of the FD-TD lattice involves the division of the computational space into two distinct regions, connected by a transverse waveguide plane, input plane, as shown in Figure 3.3.1. In two dimensions, the surface has four faces; in three dimensions, the surface has six faces. Region 2 of the FD-TD lattice is denoted as the *total-field* region. Here, it is assumed that all computed field quantities are comprised of the sum of the incident and reflected components

$$\mathbf{E}_{tot} = \mathbf{E}_{inc} + \mathbf{E}_{scat} \tag{3.3.1}$$

$$\mathbf{H}_{tot} = \mathbf{H}_{inc} + \mathbf{H}_{scat}. \tag{3.3.2}$$

The interaction structure is embedded within this region.

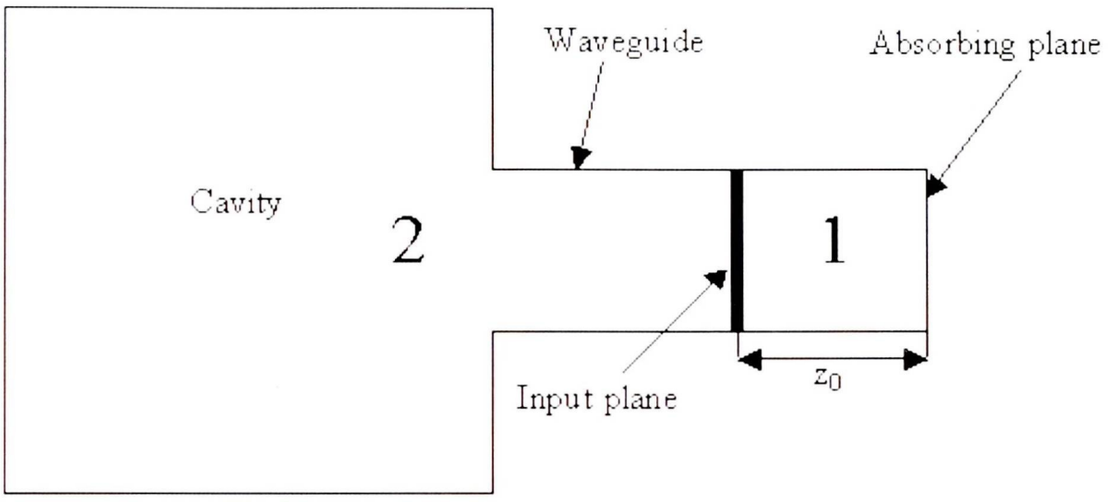

Figure 3.3.1: Schematic diagram of microwave cavity, waveguide, radiation source and absorbing plane

Region 1 of the FD-TD lattice is denoted as the *scattered-field* region. Here it is assumed that all computed field quantities are comprised only of a scattered wave component and is absorbed in the terminal plane.

The input plane is located far enough from any discontinuity to make sure that in the steady state only the lowest mode (TE_{10}) is present. In the input plane, the FD-TD scheme is corrected for the incident-field components. For a TE_{10} incident field, the new equations at the input plane location $z = k_0$ are

$$\begin{aligned} H_x^{n+\frac{1}{2}}(i, j+\frac{1}{2}, k_0-\frac{1}{2}) &= H_x^{n-\frac{1}{2}}(i, j+\frac{1}{2}, k_0-\frac{1}{2}) \\ &+ \tilde{E}_y^n(i, j+\frac{1}{2}, k_0) - \tilde{E}_y^n(i, j+\frac{1}{2}, k_0-1) \\ &+ \tilde{E}_z^n(i, j, k_0-1) - \tilde{E}_z^n(i, j+1, k_0-\frac{1}{2}) \\ &- \tilde{E}_{y,inc}^n(i, j+\frac{1}{2}, k_0) \end{aligned} \tag{3.3.3}$$

$$\begin{aligned}
\tilde{E}_y^{n+1}(i, j+\frac{1}{2}, k_0) &= C_a(i, j+\frac{1}{2}, k_0)\tilde{E}_y^n(i, j+\frac{1}{2}, k_0) + C_b(i, j+\frac{1}{2}, k_0) \\
&\times [H_x^{n+\frac{1}{2}}(i, j+\frac{1}{2}, k_0+\frac{1}{2}) \\
&- H_x^{n+\frac{1}{2}}(i, j+\frac{1}{2}, k_0-\frac{1}{2}) \\
&+ H_z^{n+\frac{1}{2}}(i-\frac{1}{2}, j+\frac{1}{2}, k_0) \\
&- H_z^{n+\frac{1}{2}}(i+\frac{1}{2}, j+\frac{1}{2}, k_0)] \\
&- C_b(i, j+\frac{1}{2}, k_0)H_{x,inc}^{n+\frac{1}{2}}(i, j+\frac{1}{2}, k_0-\frac{1}{2}).
\end{aligned} \tag{3.3.4}$$

$\tilde{E}_{y,inc}^n(i, j+\frac{1}{2}, k_0)$, and $H_{x,inc}^{n+\frac{1}{2}}(i, j+\frac{1}{2}, z_0-\frac{1}{2})$ are the transverse components of the incident wave. The equations for other fields remain unchanged. Through the definition of the incident wave components given by Equations 3.3.4 and 3.3.5, the FD-TD scheme is systematically applied in both regions, either to the total-field or to the scattered-field quantities.

§3.4 Absorbing boundary condition

The scattered wave component is absorbed by a terminal plane. The absorbing boundary condition expresses the fact that the EM field on the terminal plane comprises a wave propagating in the direction of decreasing z–coordinate with the phase velocity of the TE_{10} mode.

In steady state the scattered wave in Region 2 may be expressed as [43]

$$E_y = E_{y0}cos(\omega t + \beta z)sin\frac{\pi x}{a} \tag{3.4.1}$$

where E_{y0} is the amplitude of the scattered wave, β is the propagation constant of the TE_{10} mode and a is the broad-wall waveguide dimension.

The first order (Mur) boundary conditions[43] are used to absorb the reflected TE_{10}

wave:

$$(\frac{\partial}{\partial z} - \frac{1}{v_\phi}\frac{\partial}{\partial t})E_x|_{z=0} = 0, \tag{3.4.2}$$

$$(\frac{\partial}{\partial z} - \frac{1}{v_\phi}\frac{\partial}{\partial t})E_y|_{z=0} = 0. \tag{3.4.3}$$

where $v_\phi = \frac{1}{\sqrt{\mu_0 \epsilon_0}}$ is the phase velocity of the TE_{10} mode.

Equations 3.4.2 and 3.4.3 are discretised using centered differences and linear interpolation in time and space. The finite-difference expressions for the absorbing boundary condition are

$$\begin{aligned} \tilde{E}_x^{n+1}(i+\frac{1}{2}, j, 0) &= \tilde{E}_x^n(i+\frac{1}{2}, j, 1) + (\frac{v_\phi \Delta t - \delta}{v_\phi \Delta t + \delta}) \\ &\quad [\tilde{E}_x^{n+1}(i+\frac{1}{2}, j, 1) - \tilde{E}_x^n(i+\frac{1}{2}, j, 0)] \end{aligned} \tag{3.4.4}$$

$$\begin{aligned} \tilde{E}_y^{n+1}(i, j+\frac{1}{2}, 0) &= \tilde{E}_y^n(i, j+\frac{1}{2}, 1) + (\frac{v_\phi \Delta t - \delta}{v_\phi \Delta t + \delta}) \\ &\quad [\tilde{E}_y^{n+1}(i, j+\frac{1}{2}, 1) - \tilde{E}_y^n(i, j+\frac{1}{2}, 0)]. \end{aligned} \tag{3.4.5}$$

Due to this approximation, there is a second order local truncation error in the Equations 3.4.4 and 3.4.5. These equations relate to the tangential electric–field components at the terminal plane to the field components located at a distance δ from it. They are only valid for the considered mode (TE_{10}) and are readily implemented in the FD-TD scheme.

§3.5 Boundary Conditions on the walls and at dielectric interfaces

When an electromagnetic wave propagates in an microwave enclosure, the boundary conditions on the walls have to be met. Metallic walls are near-ideal reflectors of

microwave radiation and are often considered perfect electrical conductors. Boundary conditions for the electric and magnetic field components on a perfect conductive wall are:

$$\mathbf{E} \times \mathbf{n} = \mathbf{0} \tag{3.5.1}$$

$$\mathbf{H} \cdot \mathbf{n} = 0 \tag{3.5.2}$$

where $\mathbf{n}$ represent the unit normal vector to the interface.

When material interfaces are present, boundary conditions must be imposed to account for discontinuities of charge and current densities. Provided both media have finite conductivity and there are no impressed sources at the interface, the tangential electric and magnetic fields along the interface are continuous, i.e.,

$$\mathbf{n} \times (\mathbf{E}_2 - \mathbf{E}_1) = \mathbf{0} \tag{3.5.3}$$

$$\mathbf{n} \cdot (\epsilon'_{r2}\mathbf{E}_2 - \epsilon'_{r1}\mathbf{E}_1) = \mathbf{0} \tag{3.5.4}$$

$$\mathbf{n} \times (\mathbf{H}_2 - \mathbf{H}_1) = 0 \tag{3.5.5}$$

$$\mathbf{n} \cdot (\mu_2\mathbf{H}_2 - \mu_1\mathbf{H}_1) = \mathbf{0}. \tag{3.5.6}$$

For E_y situated at the boundary plane in Figure 3.5.1 between media 1 and 2, the equations are:

$$\epsilon_0\epsilon'_{r1}\frac{\partial E_y^1}{\partial t} + \sigma_{eff1}E_y^1 = \frac{\partial H_x^1}{\partial z} - \frac{\partial H_z^1}{\partial x} \tag{3.5.7}$$

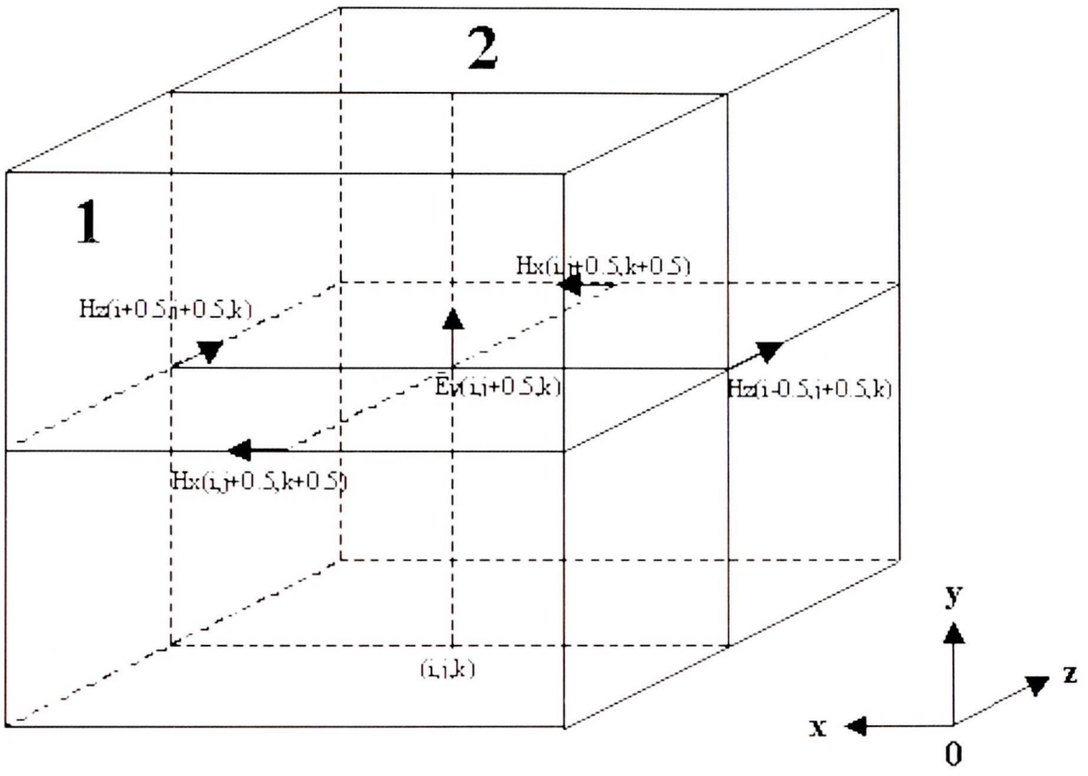

Figure 3.5.1: Field components at a boundary between two dielectrics

$$\epsilon_0 \epsilon'_{r2} \frac{\partial E_y^2}{\partial t} + \sigma_{eff2} E_y^2 = \frac{\partial H_x^2}{\partial z} - \frac{\partial H_z^2}{\partial x}. \tag{3.5.8}$$

Since the tangential electric component E_y is continuous across the interface, it is possible to add the equations 3.5.7 and 3.5.8

$$\left(\frac{\epsilon_0(\epsilon'_{r1} + \epsilon'_{r2})}{2} \right) \frac{\partial E_y}{\partial t} + \left(\frac{\sigma_{eff1} + \sigma_{eff2}}{2} \right) E_y = \frac{\partial H_x}{\partial z} - \frac{\partial H_z}{\partial x}. \tag{3.5.9}$$

This is valid only if $H_x^1 = H_x^2$ and $H_z^1 = H_z^2$ i.e $\mu_1 = \mu_2$ in equations 3.5.5 - 3.5.6. Consequently, the equations 3.2.8 and 3.2.9 have to be modified in the following form

$$C_a(i,j,k) = \frac{1 - R^{\frac{\sigma_{eff1}(i,j,k) + \sigma_{eff2}(i,j,k)}{\epsilon'_{r1}(i,j,k) + \epsilon'_{r2}(i,j,k)}}}{1 - R^{\frac{\sigma_{eff1}(i,j,k) + \sigma_{eff2}(i,j,k)}{\epsilon'_{r1}(i,j,k) + \epsilon'_{r2}(i,j,k)}}} \tag{3.5.10}$$

$$C_b(i,j,k) = \frac{R_a}{\frac{\epsilon'_{r1}(i,j,k) + \epsilon'_{r2}(i,j,k)}{2} + R^{\frac{\sigma_{eff1}(i,j,k) + \sigma_{eff2}(i,j,k)}{2}}} \tag{3.5.11}$$

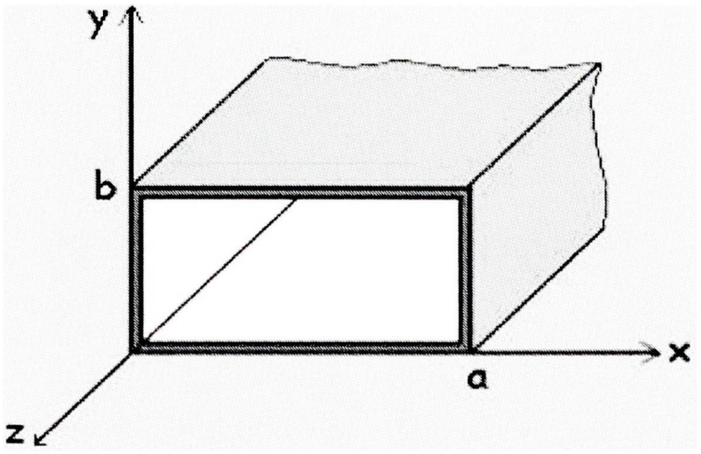

Figure 3.6.1: A rectangular waveguide

Equations for the remaining two electric field components, E_x and E_z, can be derived in a similar way. Values for ϵ_r' and σ_{eff} are specified at cell centres as $\epsilon_r'(i,j,k)$ and $\sigma_{eff}(i,j,k)$. Continuity across the interface of the tangential field is implemented automatically.

It is well known that in processing materials in cavity type-ovens, the number of modes and hence the field distribution in the heating zone, changes with and without the sample present in the cavity. The FD-TD scheme may be used to calculate the number of modes with and without the sample, the field distribution in each case, and may even provide some guidelines to the optimum size of the sample that may be heated uniformly and in the shortest period of time[30]. The FD-TD solution procedure has the unique advantage of dealing accurately and routinely with dielectric interfaces and inhomogeneities in the properties of the microwave processed samples.

§3.6 Results for electromagnetic field distribution in a single-mode cavity

A rectangular waveguide ahown in Figure 3.6.1 with dimensions a and b (assume $a > b$) and the parameters ϵ and μ is considered. If the wave propagates in the $+z$

direction, the electric field intensities in the frequency domain can be expressed as [12]:

$$E_x^+ = A_{mn}\frac{\beta_y}{\epsilon}cos(\beta_x x)sin(\beta_y y)e^{-j\beta_z z} \tag{3.6.1}$$

$$E_y^+ = -A_{mn}\frac{\beta_x}{\epsilon}sin(\beta_x x)cos(\beta_y y)e^{-j\beta_z z} \tag{3.6.2}$$

$$E_z^+ = 0 \tag{3.6.3}$$

where β_x and β_y represent the mode wave numbers or eigenvalues in the x and y directions, respectively

$$\beta_x = \frac{m\pi}{a}, \quad \beta_y = \frac{n\pi}{b}. \tag{3.6.4}$$

β_z is the phase constant and can be expressed as [69]

$$\beta_z = 2\pi\sqrt{\epsilon\mu}\sqrt{f^2 - (f_c)_{mn}^2} \tag{3.6.5}$$

where $(f_c)_{mn}$ is the cutoff frequency given by[12]

$$(f_c)_{mn} = \frac{1}{2\pi\sqrt{\epsilon\mu}}\sqrt{(\frac{m\pi}{a})^2 + (\frac{n\pi}{b})^2}. \tag{3.6.6}$$

This wave is called TE_{mn}^z mode where m denotes the number of half cycle variations of the field in the x - direction and n denotes the number of half cycle variations of the field in the y - direction.

The propagation can occur only when the operating frequency, f, is greater than $(f_c)_{mn}$. If the operating frequency is smaller than $(f_c)_{mn}$, the fields are attenuated and the waveguide serves as a filter. When the operating frequency equals $(f_c)_{mn}$ i.e $\beta_z = 0$, the standing wave pattern represents the resonant condition.

To assess the variation of the electric field in a typical microwave cavity, a simple two–dimensional single mode cavity operating in the TE_{105} mode is examined. Microwave radiation enters the cavity along a single input plane at the right side of the cavity.

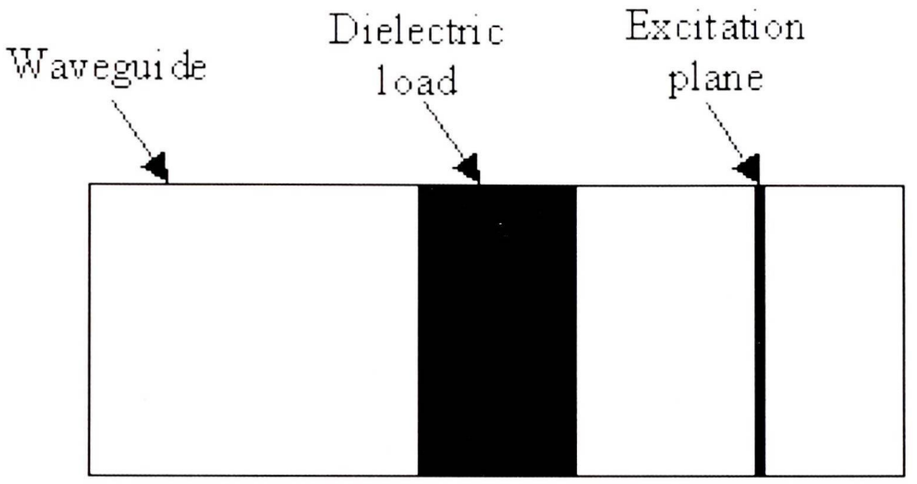

Figure 3.6.2: A 2-D dielectric loaded waveguide

The source is sinusoidally distributed in space and time with a peak amplitude of 100 kVm^{-1}. The input operates at 2.45 GHz and is positioned one-fifth of the guide wavelength from the right wall. The waveguide consists of perfectly conducting walls and its size is set to be

$$\frac{\lambda\sqrt{29}}{4} \times 2\frac{\lambda\sqrt{29}}{4} \quad i.e. \quad (16.485\,cm \times 32.97\,cm). \tag{3.6.7}$$

Mesh dimensions 30×60 are used to discretise the region, with mesh size

$$\delta = \frac{\lambda\sqrt{29}}{120}. \tag{3.6.8}$$

A schematic of the waveguide that includes a dielectric slab placed inside is shown in Fig.3.6.2. Figure 3.6.3 illustrates the root-mean-square value of the electric intensity $|E_{max}|$ in an empty cavity. The five high peak values indicate that forward and backward waves are in phase.

A dielectric slab of thickness $3.297\,cm$ and $\epsilon = 2 - j0.5$ is now placed between $13.188\,cm$ and $19.7892\,cm$ with respect to the right end of the cavity to coincides with one of the peaks of the electric field (see Figure 3.6.2) . Due to absorbing effect of the dielectric the peak sizes are now unequal and the modal pattern has changed significantly. There are six peaks now, as shown in Figure 3.6.4.

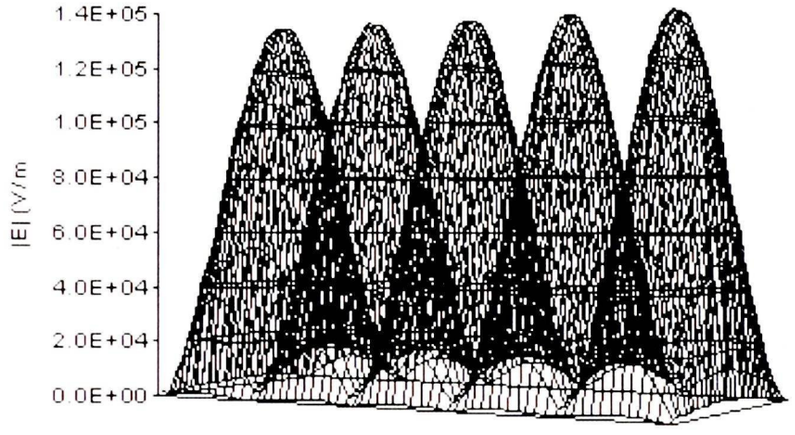

Figure 3.6.3: Electric field distribution for an unloaded cavity - TE_{105} mode

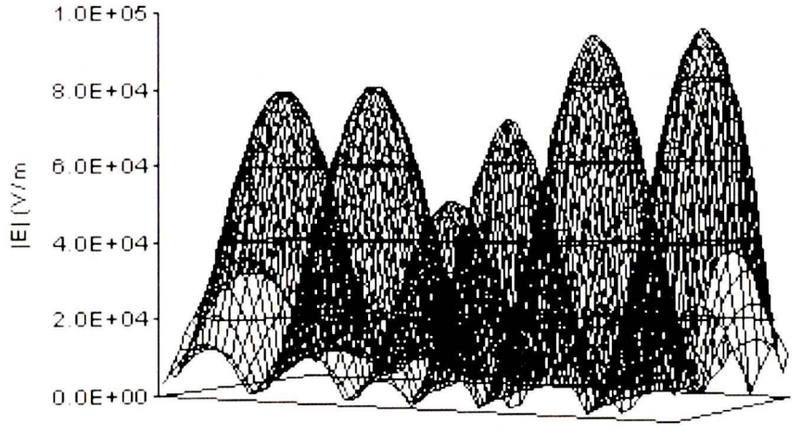

Figure 3.6.4: Electric field distribution for a loaded cavity - TE_{105} mode

§3.7 Results for electromagnetic field distribution in a multi-mode cavity

If the front and back end of the waveguide are closed and the walls are perfect conductors, the waves will bounce off the cavity walls. The field distribution in such a cavity will be determined in a similar way as for waveguides, with an additional boundary condition imposed on the front end[75]. The cutoff frequency for the TE^z_{mnp} mode in a cavity is given as

$$(f_r)_{mnp} = \frac{1}{2\sqrt{\mu\epsilon}}\sqrt{(\frac{m}{a})^2 + (\frac{n}{b})^2 + (\frac{p}{c})^2} \tag{3.7.1}$$

where c is the cavity dimension in the z direction. If the operating frequency is equal to the cutoff frequency then resonance conditions occur.

TE^z_{101} is the mode with the lowest order when $c > a > b$ and its resonant frequency is

$$(f_r)_{101} = \frac{1}{2\sqrt{\mu\epsilon}}\sqrt{(\frac{1}{a})^2 + (\frac{1}{c})^2} \tag{3.7.2}$$

When the cavity is loaded with a dielectric material, the resonant patterns will be significantly distorted. It will depend on the size, location and properties of the dielectric material. The following example investigates the impact of dielectric material placed inside the 2-D cavity on the electric field distribution. Figure 3.7.1 shows a schematic of the waveguide and cavity and includes a square specimen placed at the cavity centre. The cavity size is set to

$$a = \frac{5}{2}\sqrt{2}\lambda \quad i.e \quad (43.29\,cm \times 43.29\,cm) \tag{3.7.3}$$

thus operating in the TE_{505} mode. The walls of the cavity and waveguide are modelled as perfect electrical conductors. The computational domain is divided into 50×50 cells in the cavity and 10×10 cells in the waveguide. The mesh size is

$$\delta = \frac{\sqrt{2}}{40}\lambda \tag{3.7.4}$$

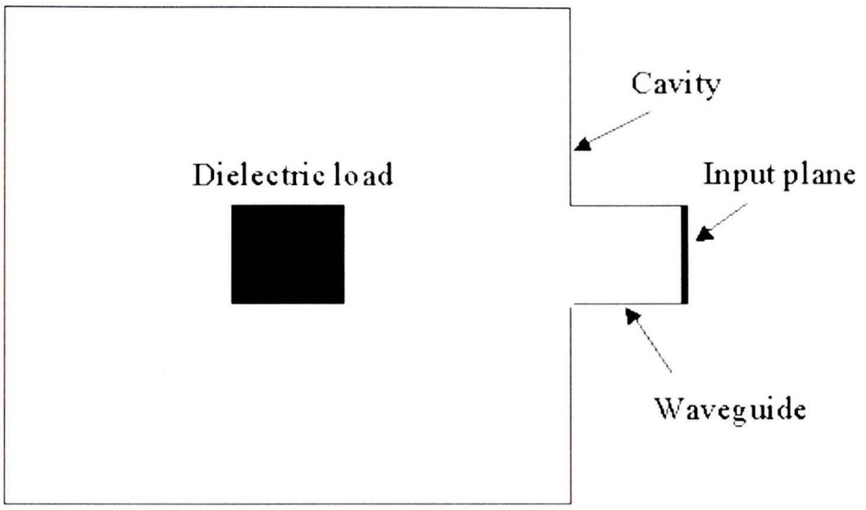

Figure 3.7.1: A microwave enclosure excited in TE_{505} mode

and time step is

$$\Delta t = \frac{\delta}{\sqrt{2}C_{max}} \tag{3.7.5}$$

where $C_{max} = (\epsilon\mu)^{-1/2}$ is the local electromagnetic wave speed. The excitation source is modelled as time harmonic and root-mean-square value $|E_{max}|$ is computed. Figure 3.7.2 shows the resulting square modal patterns corresponding to the 2.45 GHz resonant frequency after 10000 time steps. In this case the cavity is highly resonant and supports nearly perfect standing waves. If the frequency changes, the resonant behaviour will disappear as shown in Figure 3.7.3.

The total averaged power absorbed per unit depth can be calculated over each cell in the material sample, i.e.

$$Q_{total} = \sum_i \sum_j \sigma_{eff} |E_{max}|^2 \Delta x \Delta y. \tag{3.7.6}$$

In order to illustrate the effect of the change in dielectric properties, a parametric study was performed with an $8.658\,cm \times 8.658\,cm$ load placed at the centre of the enclosure.

$\epsilon_r' \setminus \sigma_{eff}$	0.01	0.06	0.1	0.4	0.7	1.0
2.0	0.778	0.720	0.664	0.440	0.519	0.663
4.0	1.000	0.727	0.709	0.492	0.489	0.579
8.0	0.418	0.651	0.583	0.469	0.438	0.461
14.0	0.191	0.280	0.285	0.255	0.269	0.278

Table 3.1: Dimensionless power absorption in an $8.658\,cm \times 8.658\,cm$ sample

Table 3.1 shows the total electromagnetic power absorbed by this load for a range of dielectric properties values. The power is normalized with respect to the maximum value obtained during the simulations. The power absorbed by the sample with $\epsilon_r' = 2.0$ and $\epsilon_r' = 4.0$ exhibits a decrease with the increase of electrical conductivity. This indicates that the resonance in these cases takes place at low σ_{eff} (see Figure 3.7.4). The resonance seems to disappear around $\sigma_{eff} = 0.1\ S/m$, but the increase in absorption is detected near the maximum value of σ_{eff}. For $\epsilon_r' = 8.0$ the resonance occurs at low σ_{eff} but it is not as strong as in the pervious cases (see Figure 3.7.5). The power absorbed when $\epsilon_r' = 14.0$ indicates resonance around $\sigma_{eff} = 0.1\ S/m$. Table 3.7 presents the dimensionless power distribution for different load sizes with different dielectric permittivities and fixed electric conductivity $\sigma_{eff} = 0.2\ S/m$. It can be noticed that the power steadily increase until the critical dimension is reached, which in this case 31.05×31.05. Electromagnetic waves cannot propagate when the distance between the sides of the load and the cavity walls is smaller than a half wavelength $\lambda_0/2 = 6.122\,cm$.

Sample dimensions (cm)$\backslash\epsilon_r'$	2.0	6.0	10.0
24.24×24.24	0.282	0.273	0.186
25.97×25.97	0.386	0.443	0.339
27.71×27.71	0.557	0.626	0.508
31.05×31.05	1.000	0.760	0.503
34.63×34.63	0.357	0.194	0.095
38.10×38.10	0.237	0.174	0.090

Table 3.2: Dimensionless power absorption sample

Similar analysis can be performed for other higher modes. Clemens et al.[69] investigated resonant behaviour using TE_{303} mode. Figures 3.7.6 and 3.7.7 show excellent agreement with their results.

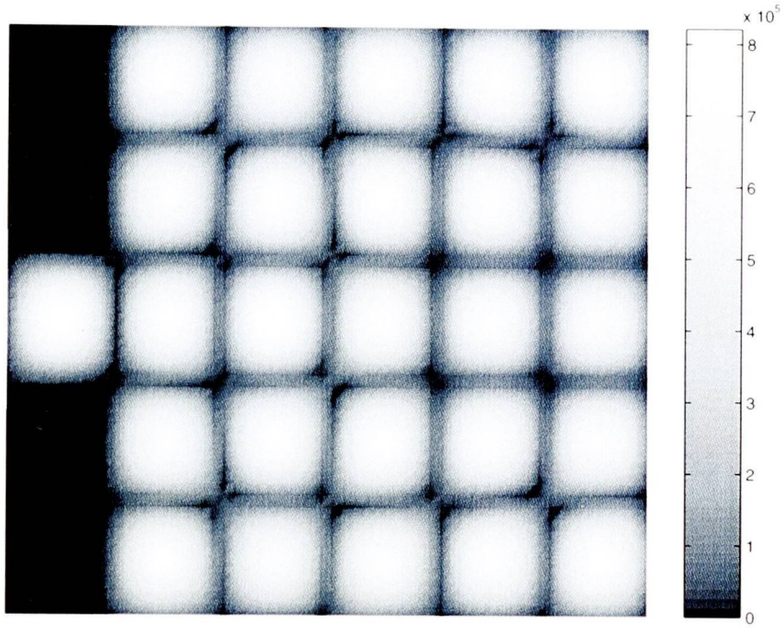

Figure 3.7.2: Electric field (V/m) distribution in an unloaded cavity at 2.45 GHz - TE_{505} mode

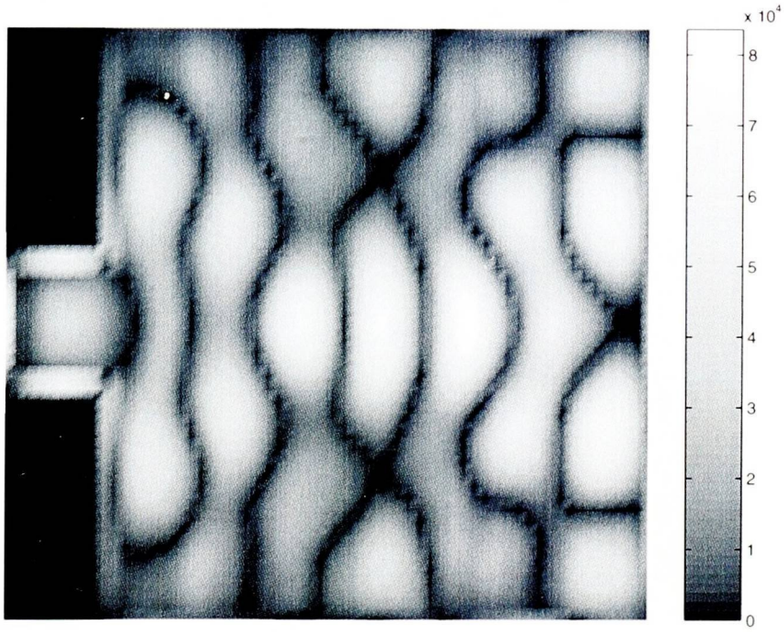

Figure 3.7.3: Electric field (V/m) distribution in an unloaded cavity at 2.205 GHz - TE_{505} mode

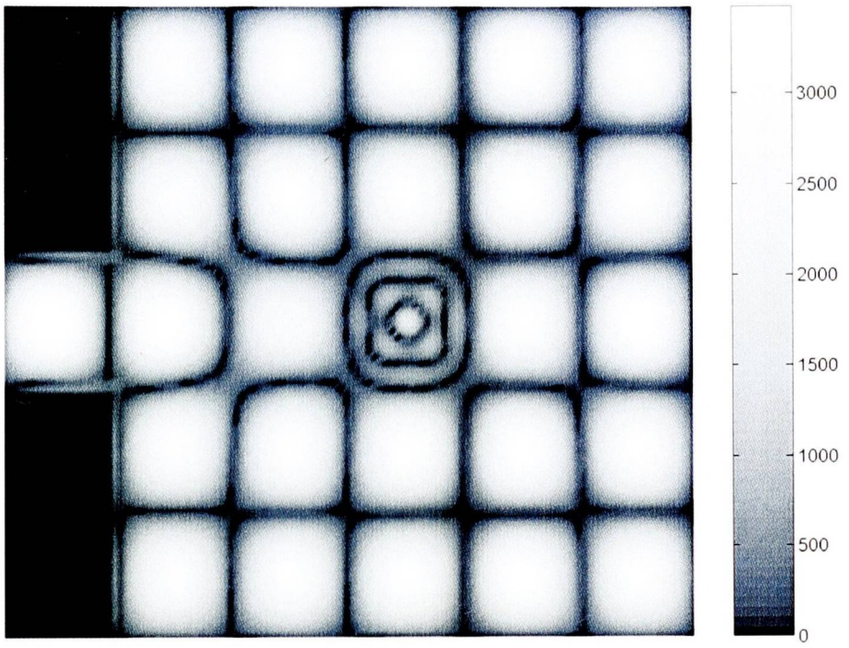

Figure 3.7.4: Electric field (V/m) distribution in a loaded cavity with sample properties $\epsilon'_r = 4.0$ and $\sigma_{eff} = 0.01(S/m)$ at 2.45 GHz - TE_{505} mode

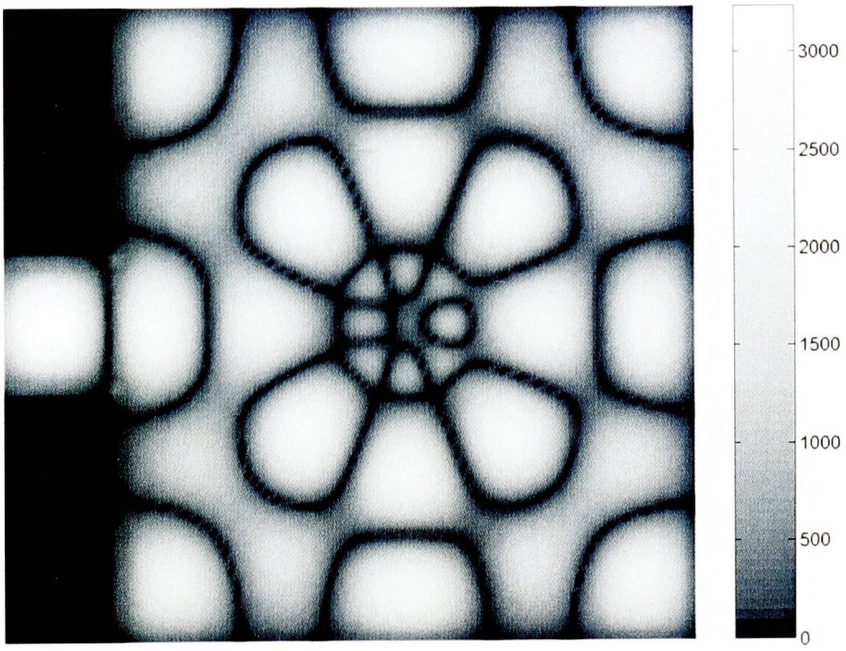

Figure 3.7.5: Electric field (V/m) distribution in a loaded cavity with sample properties $\epsilon'_r = 8.0$ and $\sigma_{eff} = 0.06(S/m)$ at 2.45 GHz - TE_{505} mode

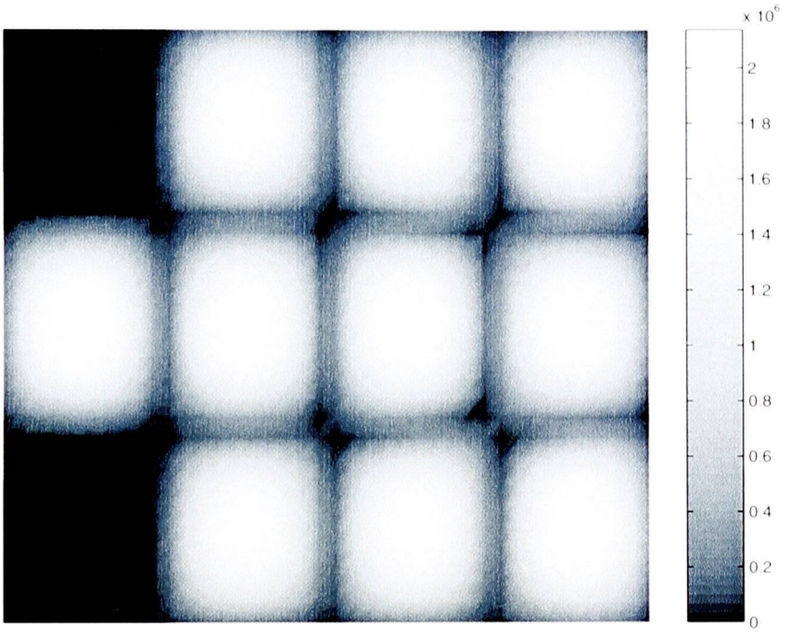

Figure 3.7.6: Electric field (V/m) distribution in an unloaded cavity at 2.45 GHz - TE_{303} mode

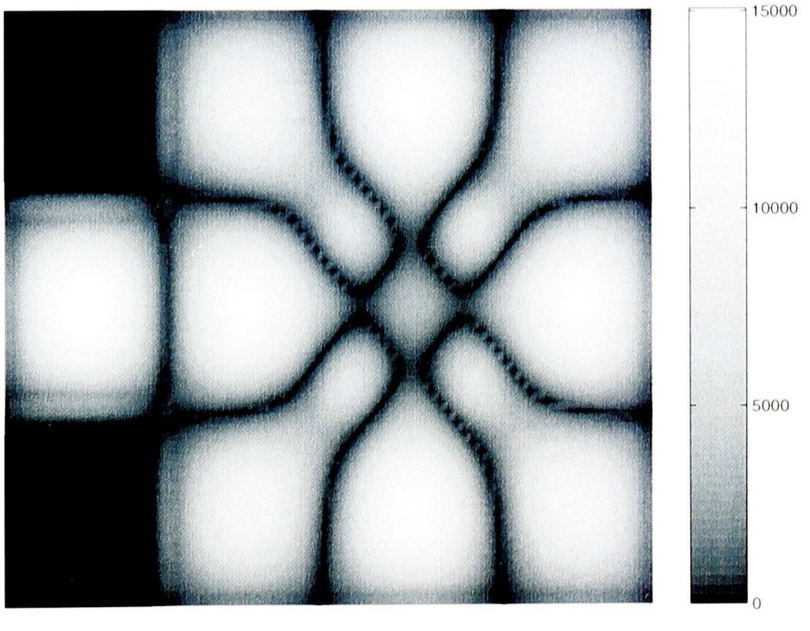

Figure 3.7.7: Electric field (V/m) distribution in a loaded cavity with sample properties $\epsilon'_r = 4.0$ and $\sigma_{eff} = 0.02(S/m)$ at 2.45 GHz - TE_{303} mode

CHAPTER

FOUR

Heat and Mass Transfer During Microwave Heating

The full two-phase flow in porous media is solved from the fluid and heat transfer equations, together with Darcy's law and change of phase.

When the laws governing the physical phenomena of fluid flow and heat transfer have been expressed in mathematical form, they are usually in terms of partial differential equations. It will be shown in this chapter that all these equations can be generalized into a single general differential equation, which expresses the transport of any conserved variable in a flow field.

In order to understand the unique character of the microwave heating phenomenon, an understanding of how electromagnetic field propagates and is absorbed by materials in needed. Hence, the mathematical model coupling the electromagnetic power deposition in materials, or heat generation, with the transport of heat due to conduction, convection, and radiation will be discussed.

This chapter first introduces the general equations that describe heat and mass transfer in two phase wet materials. It proceeds with the outline of the Finite Volume techniques employed in the discretisation of a conservation equation on a structured mesh. In order to illustrate the heat and mass transfer phenomena during microwave heating, an 1-D example of free-drying has been analyzed in the last section of the

chapter.

§4.1 Microwave power absorption

The power flux associated with a propagating electromagnetic wave is represented by the Poynting vector **S** and the average flux for harmonic fields is given [1]

$$\mathbf{S} = \frac{1}{2}\mathbf{E} \times \mathbf{H}^* \tag{4.1.1}$$

where $\mathbf{H}^*$ is a conjugate vector of **H**. The Poynting theorem allows the evaluation of the power dissipated in the medium. It is expressed as

$$\oint_S \mathbf{S} \cdot \mathbf{n} dS = -\frac{1}{2}\omega\epsilon_0\epsilon''_{eff}\int_V \mathbf{E}\cdot\mathbf{E}^* dV + \frac{i\omega}{2}\int_V (\epsilon_0\epsilon'_r\mathbf{E}\cdot\mathbf{E}^* - \mu_0\mu''_{eff}\mathbf{H}\cdot\mathbf{H}^*)dV \tag{4.1.2}$$

and states that the net power flow across a surface S enclosing a volume V equates the power dissipated in the medium (real part) to that stored in electric and magnetic fields (imaginary part). Applying the divergence theorem to equation (see Section 4.7.1.2) the point form of the Pointing theorem is

$$\nabla \cdot \mathbf{S} = -\frac{1}{2}\omega\epsilon_0\epsilon''_{eff}\mathbf{E}\cdot\mathbf{E}^* + \frac{i\omega}{2}(\epsilon_0\epsilon'_r\mathbf{E}\cdot\mathbf{E}^* - \mu_0\mu''_{eff}\mathbf{H}\cdot\mathbf{H}^*) \tag{4.1.3}$$

In order to estimate the microwave power absorption in lossy materials, a new variable, Q, called heating function, is defined. It represents a local volumetric heating rate and is related to the electric and magnetic fields inside a material [1]:

$$Q = \frac{1}{2}\omega\epsilon_0\epsilon''_{eff}|\mathbf{E}|^2 + \frac{1}{2}\omega\mu_0\mu''_{eff}|\mathbf{H}|^2. \tag{4.1.4}$$

As it can be seen from the previous chapter, the electric field distribution **E** can very significantly with position. In a similar way, **H** will have complex patterns. However, since in this work only electric polarization is considered, there are no

magnetic losses and the second term on the right-hand side of Equation 4.1.4 is negligible. This assumption valid for dielectric materials, which represent the great majority of processing applications.

In most cases microwave devices use time harmonic sources. The time variations of $\mathbf{E}$ in a sinusoidal cycle are extremely fast and (on the order of 10^{-11} and 10^{-12} sec). Since the thermal scales are many order of magnitude larger (usually on the order of seconds), there is no reason to follow such quick changes. Instead, the peak amplitude values of the electric field intensity $|E_{max}|$ are used to evaluate power density. The Equation 4.1.4 can be now rewritten as

$$Q = \frac{1}{2}\omega\epsilon_0\epsilon''_{eff}|E_{max}|^2 = \frac{1}{2}\sigma_{eff}|E_{max}|^2. \tag{4.1.5}$$

§4.2 Porosity and Representative Elementary Volume

A porous medium can be defined as a portion of space occupied by multiphase matter[76]. There maybe be gaseous and/or liquid phases. It is useful to define a *representative elementary volume* (REV) as a physical (or material) point of the porous medium that contains all phases (see Figure 4.2.1). The solid phase must be present inside each REV. The space within the porous medium that is not solid is referred to as *void space* or (*pore space*). The following equation in valid for a REV

$$r_s + r_l + r_g = 1 \tag{4.2.1}$$

where r_s, r_l, and r_g are solid, liquid, and gas volume fractions respectively

$$r_s = \frac{V_s}{V}, \quad r_l = \frac{V_l}{V}, \quad r_g = \frac{V_g}{V} \tag{4.2.2}$$

Porosity ,ϕ, is defined as the ratio of volume of the void space and the bulk volume

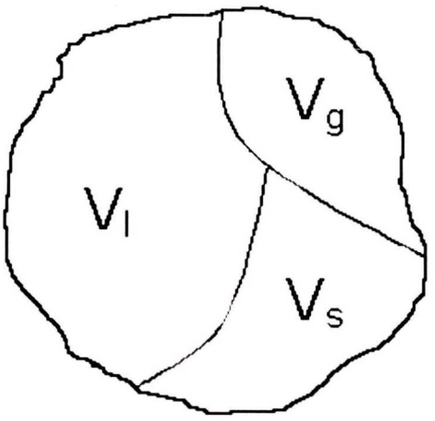

Figure 4.2.1: Representative elementary volume

of the porous medium

$$\phi = \frac{V_g + V_l}{V} = \frac{r_g + r_l}{r_s + r_l + r_g}. \tag{4.2.3}$$

When the void space of the porous medium is filled by two or more immiscible fluids (liquids or gases), the *saturation* (or *degree of saturation*) at a point, with respect to a particular fluid, is defined as the fraction of the void volume of the porous medium occupied by that particular fluid[76]. In the theory of unsaturated flow, the (volumetric) *water content* (or moisture content) is defined as

$$M = \frac{V_l}{V_l + V_g} = \frac{r_l}{r_l + r_g}. \tag{4.2.4}$$

§4.3 The general conservation equation

The transport equations for all conserved variables Φ, in a multiphase system, may be cast in a universal form as follows:

$$\frac{\partial(\rho_i r_i \Phi)}{\partial t} + div(\rho_i r_i \mathbf{u}_i \Phi - \Gamma_\Phi r_i grad(\Phi)) = S_\Phi + S_{IP} \tag{4.3.1}$$

where Γ_Φ is the exchange coefficient for Φ. The LHS terms in the equation relate to the processes of time variance, convection and diffusion respectively, whilst the RHS contains volumetric source terms within each phase S_Φ and interphase transport

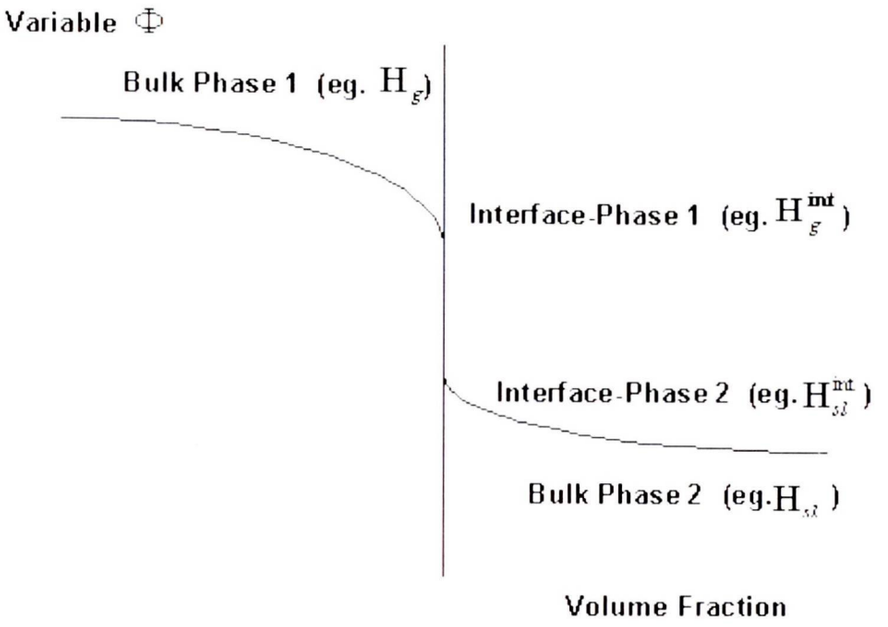

Figure 4.3.1: The concept of the interface value

terms S_{IP}. The subscript i refers to each individual phase.

The equations describing the state of a phase are basically the equations of motion, generalized to allow for the facts that each of the phases occupies only a part of the space, given by the volume fraction. The phases are exchanging mass, energy and all other properties. The resulting system is then solved numerically by iteration. Figure 4.3.1 shows the interface between two phases. Each phase is regarded as having its own distinct velocity components, its own temperature, enthalpy and mass. Phase enthalpies are linked by interface heat transfer, phase velocities by interface momentum transfer and phase concentrations by interphase mass transfer.

Let Φ^{int} be the value of Φ at the interface between the i and j phase. It can be a function of space, time, or local bulk phase values. It is a property, and not a variable obtained from a conservation equation.

In terms of a gas-liquid system, H_g^{int} and H_l^{int} represent the saturation enthalpies of gas and liquid at the local temperature and pressure. These can be obtained from the thermodynamic tables for the liquid in question.

§4.4 The Energy Equation

Substituting Φ in Equation 4.3.1 to be the specific enthalpy of the i^{th} phase. H_i and Γ_Φ to be the ration of the thermal conductivity and the specific heat of the i^{th} phase (i.e $\Gamma_\Phi = \frac{k_i}{C_{pi}}$), the general conservation equation become the energy equation for the phase i

$$\frac{\partial(\rho_i r_i H_i)}{\partial t} + \nabla \cdot (\rho_i r_i \mathbf{u}_i H_i - \frac{k_i}{C_{pi}} r_i \nabla \cdot H_i) = S_H + S_{IP} \tag{4.4.1}$$

Using the volume averaging in porous medium as described in Section 4.2, the Equation 4.4.1 can be split into two equations corresponding to two "phases" [77]. The first phase consists of solid and liquid and the second one is the gas phase

$$\overline{\rho}_{sl} \frac{\partial H_{sl}}{\partial t} + \nabla \cdot (\overline{\rho}_{sl} \mathbf{u}_l \frac{C_{pl}}{C_{psl}} H_{sl} - \overline{k}_{sl} \nabla \cdot T_{sl}) = Q + S_{sl}^{int} \tag{4.4.2}$$

$$\overline{\rho}_g \frac{\partial H_g}{\partial t} + \nabla \cdot (\overline{\rho}_g \mathbf{u}_g H_g - \overline{k}_g \nabla \cdot T_g) = S_g^{int} \tag{4.4.3}$$

where the thermal conductivity, k, is averaged for each phase as follows

$$\overline{k}_{sl} = (1 - \phi) k_s + \phi M k_l \tag{4.4.4}$$

$$\overline{k}_g = \phi (1 - M) k_g \tag{4.4.5}$$

Specific heat C_p and density ρ are averaged in a similar way. The heating function is included in the solid-liquid HTE. There will be an interphase transfer between the gas and solid-liquid phases, represents by the interface source S_i^{int} defined as

$$S_i^{int} = h_{ij} A_s (H_i^{int} - H_i) \tag{4.4.6}$$

where h_{ij} is a bulk-to-interface heat transfer coefficient, A_s is the total interface area and H^{int} are interface enthalpies.

§4.5 Mass transfer equations

For mass conservation in the flow field an additional equation, namely, the continuity equation should be satisfied, the equation is

$$\frac{\partial \rho}{\partial t} + \nabla(\rho \mathbf{u}) = 0 \tag{4.5.1}$$

where $\mathbf{u}$ is the resultant velocity. In the case of two phase flow each phase will have to satisfy a separate continuity equation. Gas phase continuity equation is given by

$$\frac{\partial(\rho_g r_g)}{\partial t} + \nabla \cdot (\rho_g r_g \mathbf{u}_g) = \dot{m}. \tag{4.5.2}$$

and the liquid phase continuity equation by

$$\frac{\partial(\rho_l r_l)}{\partial t} + \nabla \cdot (\rho_l r_l \mathbf{u}_l) + \dot{m} = 0. \tag{4.5.3}$$

r_g and r_l are gas and liquid volume fractions respectively. The interface mass transfer rate, $\dot{m}$, is determined from the balance of heat through the interface between the phases[31]

$$\dot{m} = \frac{h_1^m (H_1^{int} - H_1) + h_2^m (H_2^{int} - H_2)}{H_1^{int} - H_2^{int}} \tag{4.5.4}$$

where h_1^m and h_2^m are bulk–to interface mass transfer coefficients.

§4.6 Momentum equations

Momentum equations for the liquid-solid and gas phases can be obtained by substituting the phase velocity for Φ and the phase viscosity for Γ_Φ. The equations obtained are

$$\frac{\partial(\rho_l r_l \mathbf{u}_l)}{\partial t} + \nabla(\rho_l r_l \mathbf{u}_l \mathbf{u}_l - \nu_l r_l \nabla \mathbf{u}_l) = -\nabla p_l + S_{lu} \tag{4.6.1}$$

$$\frac{\partial(\rho_g r_g \mathbf{u}_g)}{\partial t} + \nabla(\rho_g r_g \mathbf{u}_g \mathbf{u}_g - \nu_l r_g \nabla \mathbf{u}_g) = -\nabla p_g + S_{gu} \tag{4.6.2}$$

where p_l and p_g are liquid and gas pressures and ν_l and ν_g liquid and gas viscosities, respectively. It should be noticed that since the solid density and solid volume fraction do not change in time and space, they will be lost during the differentiation and consequently the momentum equation for the solid-liquid phase will become only the liquid momentum equation 4.6.6.

In the modelling of the microwave heating process in porous media, where both convection and diffusion terms are considered, the momentum equations acquire an extra term, which have the desired effects for the modelling of microwave heating process. It is called the Darcy resistance terms, which can be treated as a source term (denoted as S_{lu} and S_{gu} in the Equations 4.6.6 and 4.6.7). The Darcy source term are used to resist motion of both gas and fluid in a porous medium. These source terms can be expressed as

$$S_{lu} = -\frac{\nu_l}{K_l}\mathbf{u}_l, \qquad S_{lg} = -\frac{\nu_g}{K_g}\mathbf{u}_g \tag{4.6.3}$$

where K_l and K_g are the liquid and gas permeabilities. They change with liquid saturation (see Section 7.3) and this dependencies are shown in Figure 7.4.2.

The liquid and gas pressures are connected through the capillary pressure p_c as[77]

$$p_l = p_g - p_c. \tag{4.6.4}$$

The capillary pressure depends on both moisture content and temperature, i.e

$$p_c = p_c(M, T). \tag{4.6.5}$$

Substituting the liquid pressure by the Equation 4.6.4, the Equations 4.6.6 and 4.6.7

become

$$\mathbf{u}_l = -\frac{K_l}{\nu_l}(\nabla p_g + l_r \nabla M + l_T \nabla T_l) \tag{4.6.6}$$

$$\mathbf{u}_g = -\frac{K_g}{\nu_g}\nabla p_g \tag{4.6.7}$$

in which

$$l_r = -\frac{\partial p_c(M, T_l)}{\partial M} \tag{4.6.8}$$

and

$$l_T = -\frac{\partial p_c(M, T_l)}{\partial T_l}. \tag{4.6.9}$$

§4.7 Energy boundary conditions

The energy boundary condition on the material's surface can be expressed as

$$-k\frac{\partial T}{\partial n} = h_c(T_s - T_a) + \sigma_{rad}\epsilon_{rad}(T_s^4 - T_a^4) - \dot{m}L \tag{4.7.1}$$

where T_s is the load surface temperature, T_a is the convective air temperature, n represents the normal to the surface, h_c is the convective heat transfer coefficient, σ_{rad} is the Stefan–Boltzmann constant, ϵ_{rad} is the radiative surface emissivity and L is the latent heat of vaporization of the evaporated liquid. The first term in the equation represents the natural convection by which the load is cooled. The second term is the surface radiation and is important as a cooling mechanism at high load temperatures, or as a heating mechanism if susceptors are used. Since materials with a high moisture content are being observed in this study, the last term, evaporative cooling will have the strongest impact on the temperature profile.

§4.7.1 Finite Volume Method

The Finite Volume (FV) method[51] is almost universally used in problems involving fluid flow with heat and mass transfer. Consequently there are many FV codes readily available to use in the microwave heating problem, both commercial and public-domain[78]. In the work presented, the code PHOENICS[29] (Parabolic Hyperbolic Or Elliptic Numerical Integration Code Series) was chosen mainly for the following reasons:

- for its ability to handle the two-fluid (water-vapour) transport using the IPSA[79] algorithm;
- for the facility for easy insertion of user Fortran routines to handle the physics of the problem and the coupling with the electro-magnetically induced heat source.
- PHOENICS continues to use a structured grid, albeit of multi-block character, augmented by fine-grid embedding, because this provides sufficient ability to fit small-scale flow features without the computational overhead of fully-unstructured grids. This feature also facilitates the coupling between FD-TD and FV which will be described in Chapter 5.

A Control Volume formulation is used for discretisation of the generalized governing equation[80]. The basic idea of the control volume formulation is easy to understand and lends itself to direct physical interpretation. The calculation domain is divided into a number of non-overlapping control volumes such that there is one control volume surrounding each grid point. A cross section of a control volume in the x, y-plane is shown in Figure 4.7.1. The control variable P is located at the cell center and surrounded by four neighboring cell centers E, W, N, S. In three dimensions it has two more neighboring cells H, L. Integrating the general differential equation

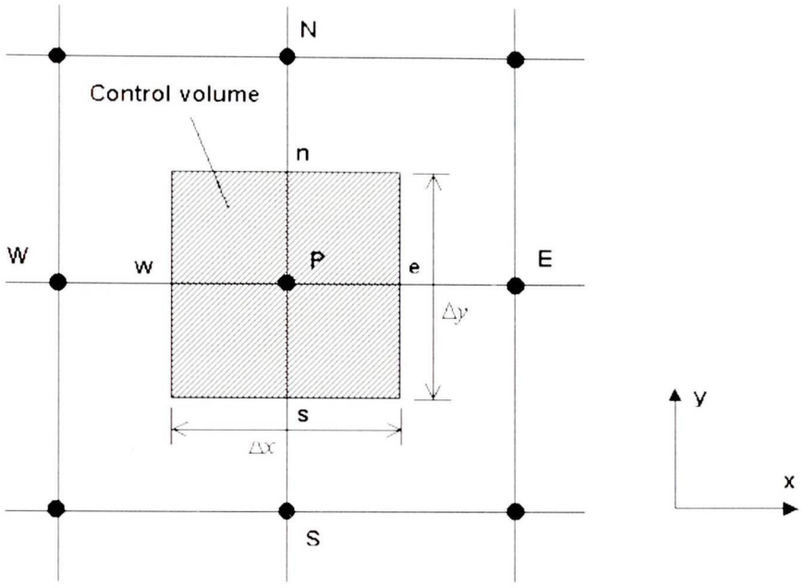

Figure 4.7.1: Two dimensional control volume

4.3.1 over control volume gives

$$\int\int\int_V \frac{\partial(\rho_i r_i \Phi)}{\partial t} dV + \int_S \rho_i r_i \mathbf{u}_i \Phi ds_i - \int_S \Gamma_\Phi r_i \frac{\partial \Phi}{\partial n_i} ds_i = \int\int\int_V (S_\Phi + S_{IP}) dV \tag{4.7.2}$$

where s_i represents the components of the outward normal area vector, n_i is the co-ordinate direction.

Each of the terms in the equation 4.7.2 will be discretized separately.

§4.7.1.1 Transient term

The transient term is integrated over time and a control volume:

$$\int\int\int_V \frac{\partial(\rho_i r_i \Phi)}{\partial t} dV = \frac{(\rho_i r_i \Phi)_P - (\rho_i r_i \Phi)_P^o}{\Delta t} V. \tag{4.7.3}$$

The superscript ^{o} denotes the old time step value, $V$is the volume of the control volume, and Δt is the time step.

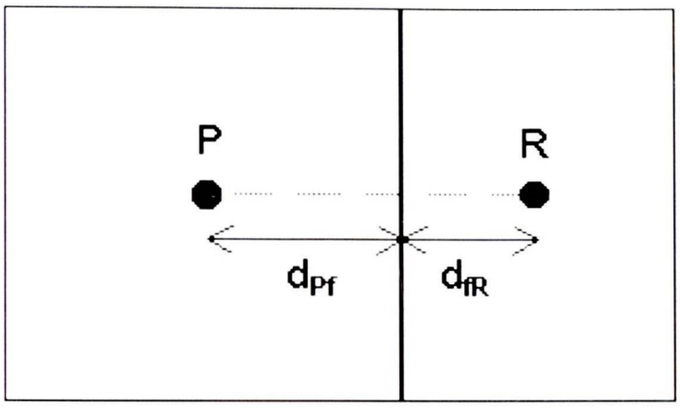

Figure 4.7.2: Two adjacent control volumes

§4.7.1.2 Diffusion Term

In order to discretize the diffusion term, the first step is to use the divergence theorem

$$\int_V \mathrm{div}(\mathbf{F})\, dV = \int_S \mathbf{F} \,.\, \mathbf{n}\, dS \tag{4.7.4}$$

which converts the volume integral into the surface integral

$$\int_V \mathrm{div}(\Gamma_\Phi r_i \mathrm{grad}(\Phi))\, dV = \int_S \Gamma_\Phi\, r_i \mathrm{grad}(\Phi) \,.\, \mathbf{n}\, dS \tag{4.7.5}$$

where $\mathbf{n}$ is the unit outward normal to the surface. Taking into account that the term $\mathrm{grad}(\Phi) \,.\, \mathbf{n}$ is equal to the gradient of Φ in the direction of the normal, the equation 4.7.5 can be simplified. The surface of any control volume consists of a set of faces (four in two-dimensions and six in three dimensions). Equation (4.7.5) can be expressed as a sum of surface integrals over each face bounding the control volume as follows

$$\sum_f \int_f \Gamma_\Phi\, r_i \frac{\partial \Phi}{\partial n}\, dS \tag{4.7.6}$$

In this work orthogonal meshes are considered, so the line that connects two different nodes will be either parallel or normal to face (see Figure 4.7.2). If the distance between the observed node P and its neighboring node R is denoted as d_{RP} then the

normal gradient in the equation 4.7.6 can be approximated as

$$\frac{\partial \Phi}{\partial n} \simeq \frac{\Phi_R - \Phi_P}{d_{RP}} \tag{4.7.7}$$

where d_{RP} is the distance between the centers of elements R and P. Hence the discretised form of equation (4.7.5) is

$$\sum_f (\Gamma_\Phi)_f \, r_i \, A_f \left(\frac{\Phi_R - \Phi_P}{d_{RP}} \right) \tag{4.7.8}$$

where A_f is the area of face f.

The interphase value of Γ_Φ can be calculated in two ways. It can be obtained by arithmetic averaging of the values of the neighboring cells (usually used when momentum equations are being solved, i.e $\Gamma_\Phi = \nu$)

$$(\Gamma_\Phi)_f = \alpha_f (\Gamma_\Phi)_P + (1 - \alpha_f)(\Gamma_\Phi)_R \tag{4.7.9}$$

$$\alpha_f = \frac{d_{FR}}{d_{FR} + d_{PF}}. \tag{4.7.10}$$

If one of the fluxes in Equation 4.7.9 is equal to zero the interface flux will still exist even though its value has to be zero. Similar problems will occur when one of the values is relatively small compared to the other one. For these reasons, it is better to use the harmonic mean in the HTE, where momentum Γ_Φ represents the conductivity of the fluid

$$(\Gamma_\phi)_f = \frac{(\Gamma_\Phi)_R (\Gamma_\Phi)_P}{(\alpha_f \Gamma_\Phi)_P + (1 - \alpha_f)(\Gamma_\Phi)_R} \tag{4.7.11}$$

If either of the $(\Gamma_\Phi)_R$ and $(\Gamma_\Phi)_P$ is equal to 0, the equation 4.7.11 gives $(\Gamma_\phi)_f = 0$. If for example, $(\Gamma_\Phi)_P >> (\Gamma_\Phi)_R$ then $(\Gamma_\phi)_f \approx (\Gamma_\phi)_R / \alpha_f$ as required.

§4.7.1.3 Convection Term

In porous media the convection term is negligible and does not play an important role. For completeness purposes, its discretisation will be briefly discussed in this section.

The divergence theorem will be used again to transform the volume integral of the convection term into a surface integral

$$\int_V \mathrm{div}(\rho_i\, r_i\, \mathbf{u}_i\, \Phi)\, dV \;=\; \int_S \rho_i\, r_i\, (\mathbf{u}_i \,.\, \mathbf{n})\, \Phi\, dS \tag{4.7.12}$$

In a similar way as with the diffusion term, the surface integral is split into a set of integrals over each of the faces bounding the control volume and each of the values in the integrand are estimated on the face and leads to

$$\sum_f \rho_{if}\, r_i\, (\mathbf{u}_i \,.\, \mathbf{n})_f\, A_f \Phi_f \tag{4.7.13}$$

In this equation the value of ρ_f may be given the value in the upwind element [80]. Thus

$$\begin{aligned} \rho_{if} &= \rho_P, \qquad (\mathbf{u}_i \,.\, \mathbf{n})_f > 0.0 \\ \rho_{if} &= \rho_R, \qquad (\mathbf{u}_i \,.\, \mathbf{n})_f < 0.0 \end{aligned} \tag{4.7.14}$$

If we use arithmetic averaging for calculation of the face value of Φ

$$\Phi_f = \alpha_f \Phi_P + (1 - \alpha_f)\Phi_R \tag{4.7.15}$$

The final discretised form convection term then becomes

$$\sum_f \rho_{if}\, r_i\, (\mathbf{u}_i \,.\, \mathbf{n})_f\, A_f\, [\alpha_f \Phi_P + (1 - \alpha_f)\Phi_R] \tag{4.7.16}$$

§4.7.1.4 Source Term

Let S_{ti} denote the total source term for the phase i

$$S_{ti} = S_\Phi + S_{IP}. \tag{4.7.17}$$

When the source term is discretised it is initially expressed in a linearised form[51]

$$S_{ti} = S_C - S_P\Phi \tag{4.7.18}$$

where the values of S_C and S_P are to prevail over the control volume and can be functions of any stored value including Φ. To maintain diagonal dominance of the resulting equation, the value of S_P must be negative. The equations used to evaluate the values of S_C and S_P can significantly affect both the rate of convergence and stability of the solution procedure. For speed as large a portion of the source as possible should be placed in the linear, $S_P\Phi$, part. This speed will be compromised if the size of S_c is also increased. Stability will be affected if changes in any aspect of the solution results in large changes in the value of S_C and S_P.

When the linearised source term is integrated over the control volume all terms are evaluated at the centre of the element to give a contribution[29]

$$V(S_C - S_P\Phi) \tag{4.7.19}$$

§4.8 Differencing Schemes

By adding together all descretised terms described in previous section, it is possible to obtain the final discretised form of Equation 4.7.2.

Firstly, let us consider only the convection and diffusion terms, and use arithmetic averaging in the evaluation of the face value of Φ in the convection term. The

discretised equation becomes

$$\sum_f A_f \left[\rho_{if}\, r_i (\mathbf{u}_i \,.\, \mathbf{n})_f \Phi_f + (\Gamma_\Phi)_f\, r_i \left(\frac{\Phi_P - \Phi_R}{d_{PR}} \right) \right] \;=\; 0 \tag{4.8.1}$$

The quantities F_f and D_f are now introduced [51]

$$F_f \;=\; A_f\, \rho_{if}\, r_i (\mathbf{u}_i \,.\, \mathbf{n})_f \tag{4.8.2}$$

$$D_f \;=\; \frac{A_f (\Gamma_\Phi)_f r_i}{d_{PR}}. \tag{4.8.3}$$

F_f is the strength of the convection of Φ and D_f is the diffusion conductance. The Peclet number, P_f, [51] can be defined as

$$P_f = \frac{F_f}{D_f} = \frac{\rho_{if} (\mathbf{u}_i \,.\, \mathbf{n})_f}{(\Gamma_\Phi)_f} \tag{4.8.4}$$

Now (4.8.1) can be rewritten as

$$a_P \Phi_P \;=\; \sum_{nb} a_{nb}\, \Phi_{nb} \tag{4.8.5}$$

where the summation is over all neighbouring elements. PHOENICS uses the hybrid scheme[79]. The following approximations are used

$$\frac{a_{nb}}{D_f} = -P_f, \quad P_f < -2 \tag{4.8.6}$$

$$\frac{a_{nb}}{D_f} = 1.0 - 0.5 P_f, \quad |P_f| < 2 \tag{4.8.7}$$

$$\frac{a_{nb}}{D_f} = 0.0, \quad P_f > 2. \tag{4.8.8}$$

This means that the coefficients in Equation (4.8.5) are

$$a_{nb} = \max(-F_f, D_f, -\frac{F_f}{2}, 0) \tag{4.8.9}$$

$$a_P = \sum_{nb} a_{nb} + \sum_f F_f \tag{4.8.10}$$

It should be noted that when the Peclet number is in the range -2 to 2 then the hybrid scheme reduces to central difference scheme and outside this range it uses a modification of the upwind scheme where the diffusion has been set to zero.

The ideas contained in this section can now be combined to discretise the full conservation equation for a scalar, Equation 4.3.1. Combining the discretised forms of each term in the equation gives

$$\frac{(\rho_P r_i \Phi_P - \rho_P^0 r_i^0 \Phi_P^0)V}{\Delta t} + \sum_f \left[\rho_{if} r_i \left(\mathbf{u}_i \,.\, \mathbf{n}\right)_f \, \Phi_f \, A_f \; - \; \left(\Gamma_\Phi\right)_f \left(\frac{\Phi_R - \Phi_P}{d_{PR}}\right) A_f \right] = (S_C - S_P \Phi_P)V \tag{4.8.11}$$

The preceding equation can be written as

$$\frac{(\rho_i r_i \Phi_P - \rho_P^0 r_i^0 \Phi_P^0)V}{\Delta t} + \sum_f \left[\{ D_f \, A(|P_f|) + max(-F_f, \, 0) \} \, (\Phi_P - \Phi_R) + F_f \, \Phi_P \right] = (S_C - S_P \Phi_P)V \tag{4.8.12}$$

where the formula for the function $A(|P_f|)$ for the hybrid scheme is

$$A(|P_f|) = \max(0, 1 - 0.5|P_f|). \tag{4.8.13}$$

The continuity equation

$$\frac{\partial(\rho_i r_i)}{\partial t} + \mathrm{div}(\rho_i r_i \mathbf{u}_i) \; = \; 0 \tag{4.8.14}$$

can similarly be discretised to give

$$\frac{(\rho_P r_i - \rho_P^0 r_i^0)V}{\Delta t} + \sum_f F_f = 0 \tag{4.8.15}$$

Multiplying equation (4.8.15) by Φ_P and substituting into equation (4.8.12) gives an equation of the form

$$a_P \Phi_P = \sum_{nb} a_{nb} \Phi_{nb} + b_P \tag{4.8.16}$$

where the summation is over all elements which share a face with element P. The coefficients in equation 4.8.16 are calculated from the formulae

$$a_{nb} = D_f A(|P_f|) + \max(-F_f, 0.0) \tag{4.8.17}$$

$$b_P = S_C V + \frac{\rho_P^0 r_i^0 \Phi_P^0}{\Delta t} V \tag{4.8.18}$$

$$a_P = \sum_{nb} a_{nb} + \frac{\rho_P^0 r_i^0 V}{\Delta t} + S_P V \tag{4.8.19}$$

Set of equations 4.8.17-4.8.19 represent the final form of the discretised equation which can now be solved.

§4.9 Momentum - Pressure Coupling

If the pressure is given, the solution of the momentum equations 4.6.6-4.6.7 can be obtained by employing the formulation completed in the following section for the general variable Φ. In the momentum equations, Φ stands for the relevant velocity component, and Γ_Φ and S_Φ are to be given their appropriate meanings[51]. The final

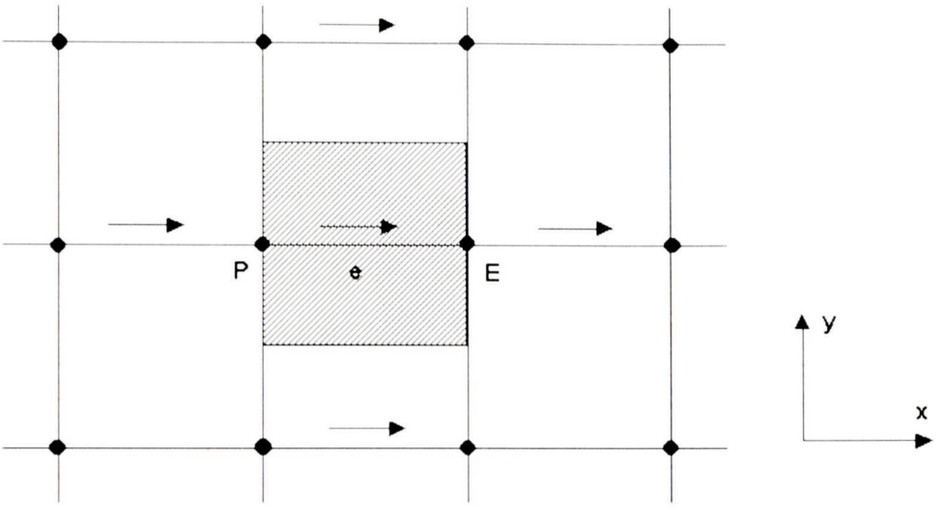

Figure 4.9.1: Control volume for u

discretised Equation 4.8.16 can be now be expressed for u velocity component as:

$$a_e u_e = \sum_{nb} a_{nb}\, u_{nb} + b + (p_P - p_E) A_e \tag{4.9.1}$$

The neighbour coefficients a_{nb} account for the combined convection-diffusion influence at the control volume faces. The term b is defined in the same manner as b_P in the Equation 4.8.16, but the pressure gradient is not included in the source term quantities S_C and S_P. Since the pressure field is also to be ultimately calculated, it needs to be included in the momentum equations source term. The term $(p_P - p_E)A_e$ is the pressure force acting on the u control volume and A_e is the area on which the pressure difference acts (see Figure 4.9.1). The momentum equations for the other directions are handled in a similar manner.

However, in order to solve the momentum equations, the pressure field has to be known or somehow estimated. If the pressure is not correct, the velocities consequently will not satisfy the continuity equation. If we denote the guessed pressure as p^* and the imperfect velocities as u^*, v^*, w^* the following discretized equations can be written

$$a_e u_e^* = \sum_{nb} a_{nb}\, u_{nb}^* + b + (p_P^* - p_E^*) A_e \tag{4.9.2}$$

$$a_n v_e^* = \sum_{nb} a_{nb}\, v_{nb}^* + b + (p_P^* - p_N^*) A_n \tag{4.9.3}$$

$$a_t w_t^* = \sum_{nb} a_{nb}\, w_{nb}^* + b + (p_P^* - p_T^*) A_t. \tag{4.9.4}$$

The estimation of the guessed pressure needs to be accurate so that the resulting velocity will get closer to satisfying the continuity equation. If the pressure is expressed as

$$p = p^* + p' \tag{4.9.5}$$

the term p' is called the pressure correction. The velocity components can be introduced in a similar manner

$$u = u^* + u' \tag{4.9.6}$$

$$v = v^* + v' \tag{4.9.7}$$

$$w = w^* + w' \tag{4.9.8}$$

If we subtract Equation 4.9.2 from Equation 4.9.1 we obtain

$$a_e u_e' = \sum_{nb} a_{nb}\, u_{nb}' + b + (p_P' - p_E') A_e \tag{4.9.9}$$

If the term $a_{nb}\, u_{nb}'$ is neglected the last equation can be rewritten as

$$a_e u_e' = (p_P' - p_E') A_e \tag{4.9.10}$$

or

$$u_e' = \frac{A_e}{a_e}(p_P' - p_E'), \qquad d_e = \frac{A_e}{a_e}. \tag{4.9.11}$$

Equation 4.9.11 is the velocity correction formula. The velocity components using the above approach can be expressed as

$$u_e = u_e^* + \frac{A_e}{a_e}(p'_P - p'_E) \tag{4.9.12}$$

$$v_e = v_n^* + \frac{A_n}{a_n}(p'_P - p'_N) \tag{4.9.13}$$

$$w_e = w_t^* + \frac{A_t}{a_t}(p'_P - p'_T) \tag{4.9.14}$$

The next step is to obtain a discretization equation for p'. The continuity equation

$$\frac{\partial \rho}{\partial t} + \text{div}\,(\rho \mathbf{u}) = 0 \tag{4.9.15}$$

discretises in the form

$$\frac{(\rho_P - \rho_P^0)V}{\Delta t} + \sum_f A_f\,(\rho \mathbf{u}\,.\,\mathbf{n})_f = 0 \tag{4.9.16}$$

where the superscript 0 signifies the previous time step value, Δt is the time step and the summation is over all faces of the control volume signified by the subscript P.

Finally substituting Equations 4.9.12-4.9.14 into the discretised continuity equation (4.9.16) gives

$$\sum_f \rho_f A_f^2 \frac{n_i^2}{a_i}(p'_P - p'_A)_f = \frac{(\rho_P^0 - \rho_P)V}{\Delta t} - \sum_f A_f \rho_f (\mathbf{u}^*.\mathbf{n})_f \tag{4.9.17}$$

where the subscript, i, in the first term indicates a summation over the three coor-

dinate directions. The above equation can be written in the form

$$a_P p'_P + \sum_{nb} a_{nb} p'_{nb} = b_P \tag{4.9.18}$$

where the summation in equation (4.9.18) is over all elements sharing a face with element P and

$$a_{nb} = -\rho_f A_f^2 \sum_{i=1}^{3} \frac{n_i^2}{a_i} \tag{4.9.19}$$

$$a_P = -\sum_{nb} a_{nb} \tag{4.9.20}$$

$$b_P = \frac{(\rho_P^0 - \rho_P)V}{\Delta t} - \sum_{f} A_f \rho_f (\mathbf{u}^*.\mathbf{n})_f \tag{4.9.21}$$

These equations for the coefficients lead to a set of linear equations with weak diagonal dominance, the diagonal being at least as large as the sum of absolute values the off diagonal elements. Boundary conditions, or a fixed reference pressure point, will guarantee diagonal dominance on some rows. Consequently, the matrix equation can be solved using the same iterative techniques which are employed to obtain the solution for any solved scalar variable[51].

The above described procedure for momentum pressure coupling in knows as Semi-Implicit Method for Pressure-Linked Equations[51] (SIMPLE algorithm). It ca be briefly summarized as following:

- Guess the pressure field p^*
- Solve the momentum equations 4.6.6-4.6.7 to obtain $u*, v*, w*$
- Solve the p' equation
- Calculate the pressure p and the velocities u, v, w using Equations 4.9.5 and

4.9.7-4.9.8 respectively

- . Solve any other equations which might affect fluid properties, source terms, etc (e.g temperature, concentration etc)

- Treat the corrected pressure p as a new guessed pressure p^* and repeat the procedure until a converged solution is obtained.

§4.10 Overrelaxation and underrelaxation

When an iterative scheme is employed to handle nonlinearity, it is often desirable to speed up or to slow down the changes in the values of the dependent variable. When changes are accelerated the process is called overrelaxation and when they are slowed down it is called underrelaxation. When a line-by-line method is used, underrelaxation is very useful. Its use avoids divergence in the iterative solution.

The general discretisation equation 4.8.16 can be rewritten as is given in the following form:

$$\Phi_P = \frac{\Sigma a_{nb}\Phi_{nb} + b_P}{a_P} \tag{4.10.1}$$

Further, $\Phi_P^\diamond$ will denote the value of Φ_P from the previous iteration. If the $\Phi_P^\diamond$ is added to the right-hand side and also subtracted, the last equation becomes

$$\Phi_P = \Phi_P^\diamond + (\frac{\Sigma a_{nb}\Phi_{nb} + b}{a_P} - \Phi_P^\diamond) \tag{4.10.2}$$

where the contents of the parentheses represent the changes in Φ_P produced by the current iteration. This change can be modified by the introduction of the relaxation factor α, so that

$$\Phi_P = \Phi_P^\diamond + \alpha(\frac{\Sigma a_{nb}\Phi_{nb} + b}{a_P} - \Phi_P^\diamond) \tag{4.10.3}$$

or

$$\frac{a_P}{\alpha}\Phi_P = \Sigma a_{nb}\Phi_{nb} + b + (1-\alpha)\frac{a_P}{\alpha}\Phi_P. \qquad (4.10.4)$$

When the iterations converge, Φ_P becomes equal to $\Phi_P^\diamond$, and implies that the converged values of Φ do satisfy the original equation 4.8.16. Any relaxation scheme must produce the final converged solution, although it can be obtained by the use of arbitrary relaxation factors.

When the relaxation factor α in the Equation 4.10.3 is between 0 and 1, its effect is underrelaxation; that is, the values of Φ_P stay closer to $\Phi_P^\diamond$. For a vary small value of α, the changes in Φ_P become very slow. For $\alpha > 1$ it becomes overrelaxation.

There are no general rules for choosing the best value of α. The optimum value depends upon many factors, such as nature of the problem, the number of grid points, the grid spacing, and the iterative procedure used. Usually, a suitable value of α can be found by experience and from exploratory computations for the given problem.

§4.11 Results for a sublimation-condensation model for freeze drying of unsaturated porous media

A one-dimensional sublimation-condensation model for freeze drying of unsaturated porous media is described in this section. The governing equations were solved using an implicit finite difference scheme with a time-variable time step[56]. Figure 4.11.1 shows a porous media slab to be freeze-dried with microwave heating. There are two different regions inside the material to be identified: the dried region and sublimation-condensation region separated by the sublimation front.

The 1-D heat and mass transfer equations are used to describe the heat and mass transfer. The heating function included as a source term in the heat transfer equation

is assumed constant.

On the sublimation-condensation region the convection term in the vapour continuity equation has been ignored and the interphase mass source term, $\dot{m}$, is expressed in the following form[56]

$$\dot{m} = -\frac{\partial J_S}{\partial x} + I. \tag{4.11.1}$$

The vapor source term I is

$$I = u_{sat}\frac{\partial M}{\partial t} \tag{4.11.2}$$

where the moisture content of the saturated porous medium is $u_{sat} = 685kg/m^3$[56]. The vapor flow J_s has two terms based on Darcy's and Fick's laws

$$J_S = -\frac{K_g\rho_g}{k_g}\frac{\partial p}{\partial x} - (1-M)\rho_g D\frac{\rho_g}{\partial x} \tag{4.11.3}$$

where diffusivity $D = 2.51 \times 10^{-5} \times (1.013 \times 10^5/P)$[56].

The length of the slab $l = 0.008\,m$ was divided into 200 control volumes. The initial saturation 0.7, electric field amplitude $120\,V/cm$ and reference pressure $15\,Pa$ were chosen.

Figures 4.11.2 to 4.11.4 show the distributions of pressure, vapour of the material at different times, respectively. From figures 4.11.2 and 4.11.3 it can be concluded that the pressure and vapour density follow similar patterns. The gradients of pressure and vapour density are large in the sublimation-condensation period initially, then decrease and become smaller than those in the dried region. Even though the gradients are much larger in the dried region, the vapor transfer exists in the sublimation-condensation region (Equation 4.11.3). The fact that the pressure (see Figure 4.11.3 and vapor density (see Figure 4.11.2) decrease from the material centre towards the sublimation front indicates that the vapor will be removed from the sublimation-

condensation region. As the result, the ice in the sublimation-condensation region will sublimate and saturation in this region will decrease (see Figure 4.11.4). It can be noticed that the saturation is nearly uniform in the sublimation-condensation region though it is larger near the sublimation front than in the centre. All the vapor sublimated in the sublimation-condensation region joins the man flow in the dried region. So the drying rate during microwave freeze drying of saturated porous media consists of two flows associated with sublimation front and sublimation-condensation region.

This example has been validated against computational results for a similar problem obtained by Wang and Shi[56].

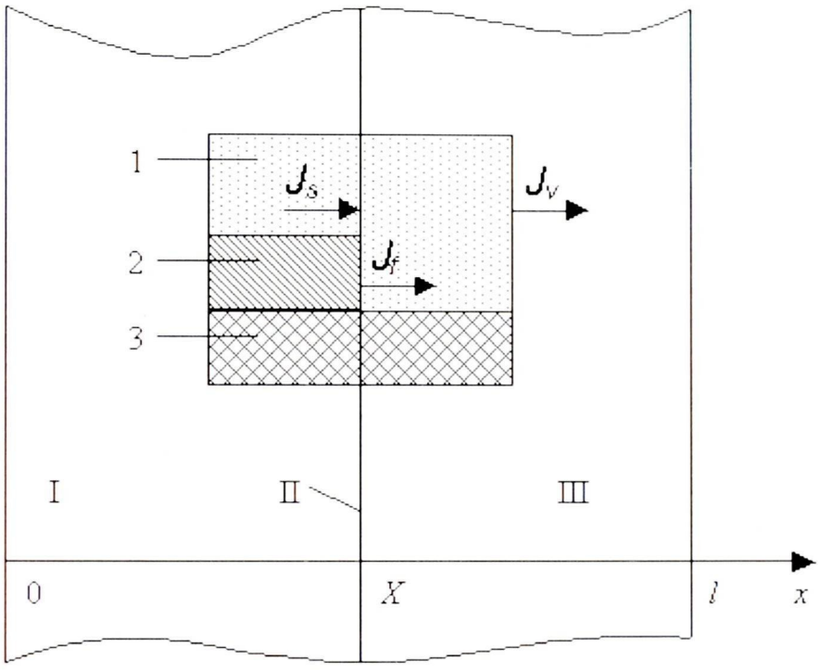

Figure 4.11.1: 1-D sublimation-condensation model. I-Sublimation-condensation region; II-Sublimation front; III-Dried region; 1-vapor $(\phi(1-M))$; 2-ice (ϕM); 3-solid body $(1-\phi)$.

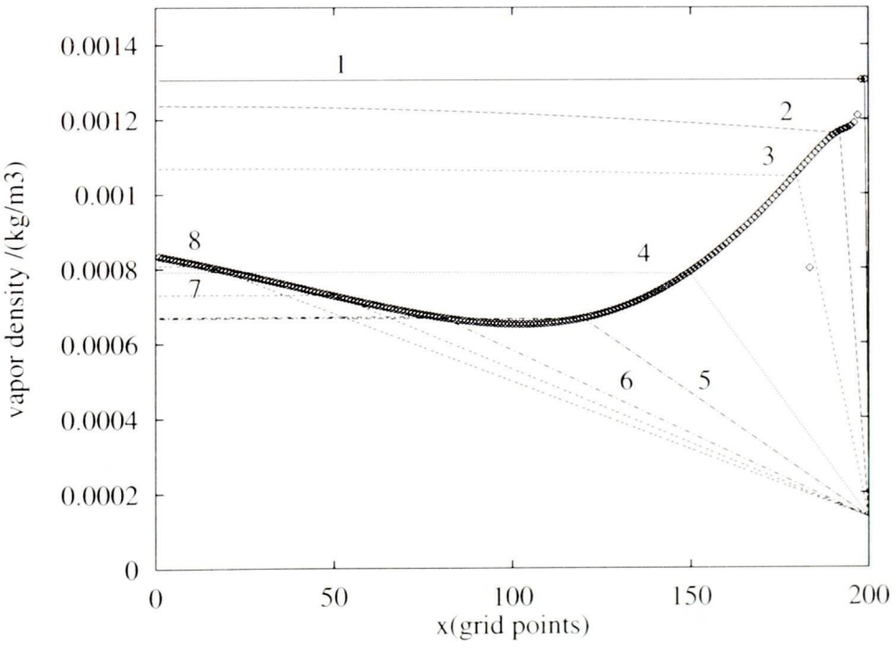

Figure 4.11.2: Vapour density profile in drying $t(sec)$: 1–0, 2–0.1, 3–9, 4–76, 5–572, 6–2714, 7–4950, 8-7489.

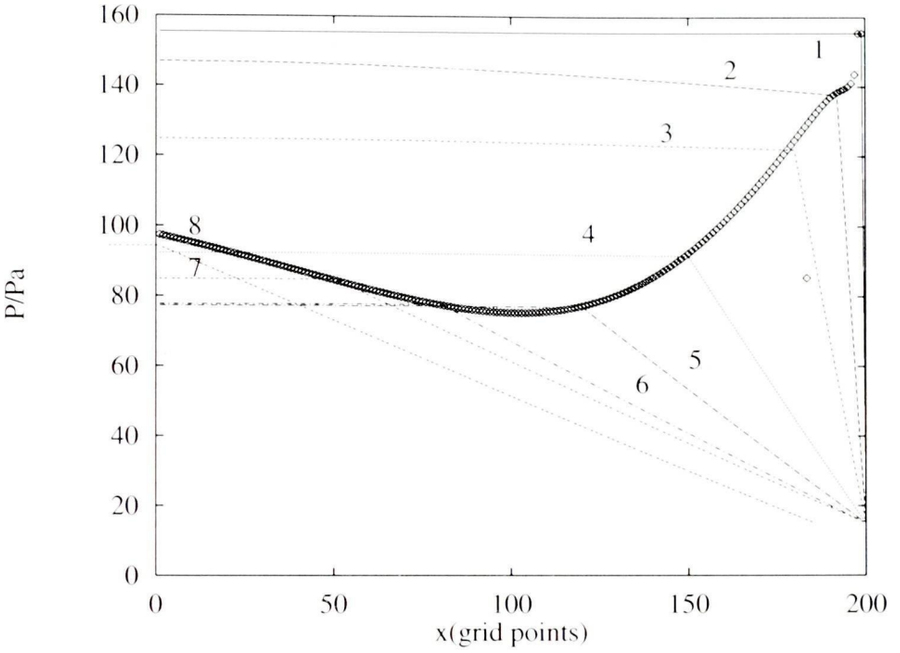

Figure 4.11.3: Pressure profile in drying $t(sec)$: 1–0, 2–0.1, 3–9, 4–76, 5–572, 6–2714, 7–4950, 8-7489.

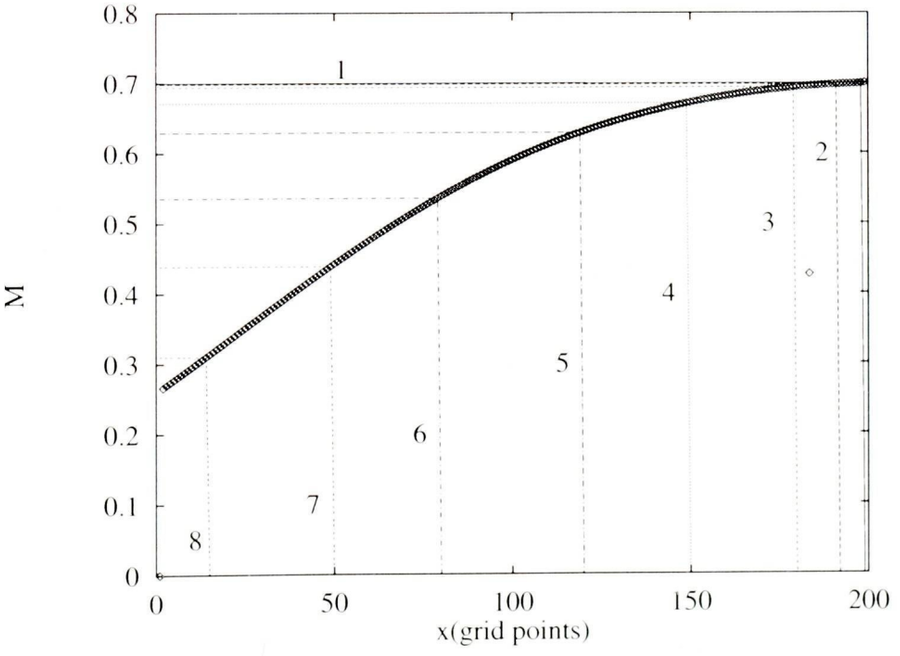

Figure 4.11.4: Saturation profile in drying $t(sec)$: 1–0, 2–0.1, 3–9, 4–76, 5–572, 6–2714, 7–4950, 8-7489.

CHAPTER

FIVE

Solution technique

In this section a detailed algorithm that couples microwave power dissipation with heat and mass transfer is presented. The coupling is through dielectric properties which are assumed to be both temperature and moisture dependent.

The rate of change of temperature inside the material depends upon the power density, which relates to the input microwaves, and also the thermal properties of the material. In Section 5.2 the criteria for determining when the power distribution has reached a steady state are investigated. Different approaches are suggested together with the description of the stability condition for the time step in FD-TD.

Changes in dielectric properties according to temperature and moisture distribution influences the electromagnetic distribution. In section 5.3 we propose a method to determine when the microwave power should be recalculated.

The chapter ends with some computational issues in section 5.6.

§5.1 Calculation of the dissipated power

With the FD-TD scheme, the electric and magnetic fields are calculated simultaneously, and hence the dissipated power can easily be found from the **E** vector. However, the three Cartesian components are not known at the same point, but they are spread over the unit cell of the Yee's lattice. The dissipated power is localized in the centre of each cell and is calculated through linear interpolation of the electric field components located at the vertices of the unit cell. The power density per m^3 in a point $(i+\frac{1}{2})\delta$, $(j+\frac{1}{2})\delta$, $(k+\frac{1}{2})\delta$ is found from the following expression:

$$\begin{aligned}
P_y^{n+1}(i+\frac{1}{2},j+\frac{1}{2},k+\frac{1}{2}) &= \frac{1}{32}\sigma(i+\frac{1}{2},j+\frac{1}{2},k+\frac{1}{2}) \\
\times[E_x^{n+1}(i+\frac{1}{2},j,k) &+ E_x^{n+1}(i+\frac{1}{2},j+1,k) \\
+E_x^{n+1}(i+\frac{1}{2},j,k+1) &+ E_x^{n+1}(i+\frac{1}{2},j+1,k+1) \\
+E_y^{n+1}(i,j+\frac{1}{2},k) &+ E_y^{n+1}(i+1,j+\frac{1}{2},k) \\
+E_y^{n+1}(i,j+\frac{1}{2},k+1) &+ E_y^{n+1}(i+1,j+1,k+\frac{1}{2} \\
+E_z^{n+1}(i+\frac{1}{2},j,k) &+ E_z^{n+1}(i+\frac{1}{2},j+1,k) \\
+E_z^{n+1}(i+\frac{1}{2},j,k+1) &+ E_z^{n+1}(i+\frac{1}{2},j+1,k+1)]
\end{aligned} \tag{5.1.1}$$

where $n+1$ denotes the $(n+1)^{th}$ full-cycle interval of time stepping. Because the fields and the power density are obtained in an iterative manner, the measures of convergence have to introduced. Different convergence criteria will be discussed later in this chapter.

§5.2 Stability condition

The accuracy of the solution of Equation 5.1.1 is influenced by the choice of δ and Δt. The space increment must be a small fraction of the wavelength and overall dimensions of the structure[43]. The time increment must satisfy the following stability

condition[37]

$$\Delta t \leq \frac{C_{max}}{(\frac{1}{\Delta x^2} + \frac{1}{\Delta y^2} + \frac{1}{\Delta z^2})^{\frac{1}{2}}}. \tag{5.2.1}$$

Recently an ADI version of FD-TD has been shown to be unconditionally stable [51]. In our simulations, the time step was set to be 95% of the minimum time step for the mesh and material. When the step size δ is the same in all directions, the stability condition is

$$\Delta t \leq \frac{C_{max}\delta}{\sqrt{N}} \tag{5.2.2}$$

where N is the number of spatial dimensions in the problem.

§5.3 Coupling Algorithm

The coupling algorithm is shown in Fig.5.3.1 and is similar to that of Turner's[36]. It can be summarized as follows: the FD-TD solver is run until the steady state (pure time harmonic) is sufficiently well approximated and the power distribution Q, computed from the peak field amplitudes, has converged. The temperature distribution and moisture content then evolve according to this power distribution until the electric properties of the medium have changed significantly. The electromagnetic solver is then re–run, taking into account the new electrical properties. Once the steady state is reached again, the whole procedure is repeated until the required heating time is reached. To solve the coupling of the microwave and thermal and mass transfer models numerically, there are two technical issues that have to be discussed. The first one concerns how long the average power density will take to reach the steady state and the second one addresses the issue of when to update the electromagnetic field information.

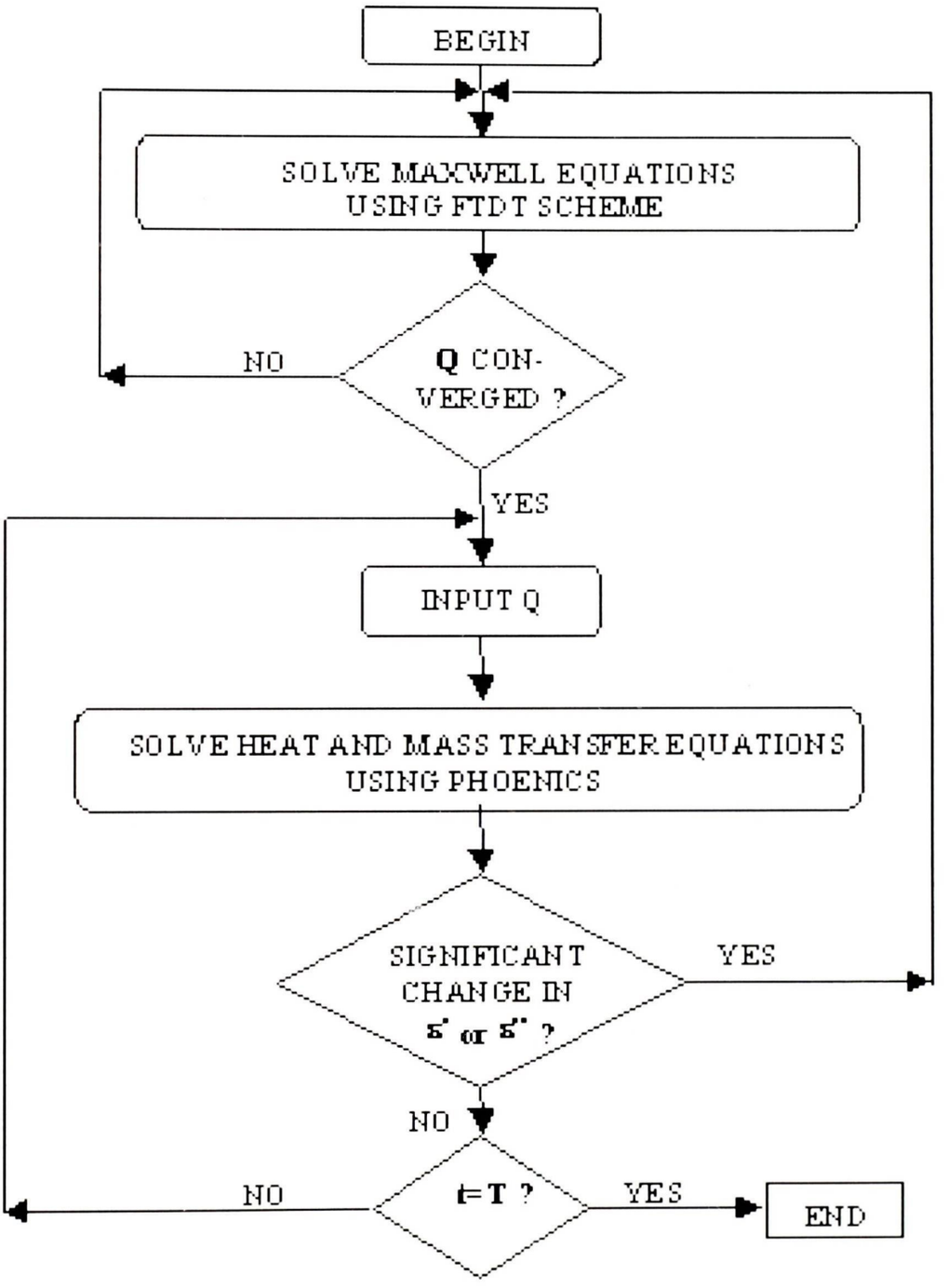

Figure 5.3.1: Coupling algorithm

§5.3.1 Criteria for determining the steady state information

There are three main criteria that exist in literature for determining when the electromagnetic field distribution has become time harmonic so that the power function information can be inserted as a source term in the HTE.

§5.3.1.1 Criteria based on the ratio of the heating system dimension and the wavelength

Zhao and Turner[18] suggested that the average power distribution be dependent on the length of the time the wave takes to travel from the input boundary to the end of the heating system. In other words, it depends approximately on the ratio of the dimension of the heating system and the wavelength

$$B_p = 2(\frac{D_{max}}{\lambda}) \tag{5.3.1}$$

where D_{max} is the maximum dimension of the geometry of the heating system, i.e the minimum distance between the input plane and the end of the heating system. λ is the wavelength in the system and B_p is the approximate number of microwave periods necessary for the microwaves to complete one cycle. This factor effectively corresponds with the time that the microwaves take to propagate from the input boundary to the end of the heating system and travel back to the input boundary. For a frequency of 2.45 GHz, the minimum time required to obtain the steady-state average power distribution, is in the order of 10^{-8} seconds. It should be noted that the approximation 5.3.1 has been found to be within 10% accuracy for all test cases[18].

§5.3.1.2 Criteria based on phase information

In reference [74] a more complicated method for the derivation of the sinusoidal state

amplitude and phase is discussed. The method will be summarized in this section.

It is possible to observe the peak positive and negative values of the field over a complete cycle of the incident wave. This particular algorithm has an uncertainty of one time step or less, and operates where the sign of the waveform time derivative changes from positive to negative, or negative to positive. Notation used:
N_{CYCLE}– the number of complete cycles of the sinusoidal incident wave that the FT–DT is time–stepped.
$N_C = \frac{1}{f\Delta t}$ - the number of time steps spanning one complete cycle of the sinusoidal incident wave
$N_{HC} = \frac{N_C}{2}$- the number of time–steps spanning one–half cycle of the sinusoidal incident wave
$N^C_{MAX} = N_{CYCLE} \times N_C$ - the total number of time steps that the FD-TD program is time-stepped
$N^{HC}_{MAX} = N_{CYCLE} \times 2 \times N_{HC}$-total number of time steps dividable by half cycle number , so the error is $\pm\,\Delta t$
N_{MAX}–max number of time–steps
Let F denote the time derivative a field component. Every time step, the algorithm tests for a change of sign of the time derivatives. If a change of sign is detected, the latest computed value of F is stored. Note that this value can be either positive or negative. If, further, the new sign of the time derivative is negative, indicating that a "peak" of the F waveform has just occurred, the time step number , NA, is stored in the array. The algorithm also tests to determine when half-cycle and full-cycle intervals of time-stepping have passed. Each half-cycle, the stored values of the functions are printed and reset to zero. Each full-cycle, the stored values of NA are printed and reset. Therefore, the desired zero–to peak value of F is determined by subtracting the last printed value of F from the immediately preceding printed value of F, taking the absolute value and then dividing by two. Also the desired relative change of NA from some fixed reference value at a specific point. This methodology avoids any ambiguity due to either a possible DC offset of the waveform F or the repetitive nature of the F transform.

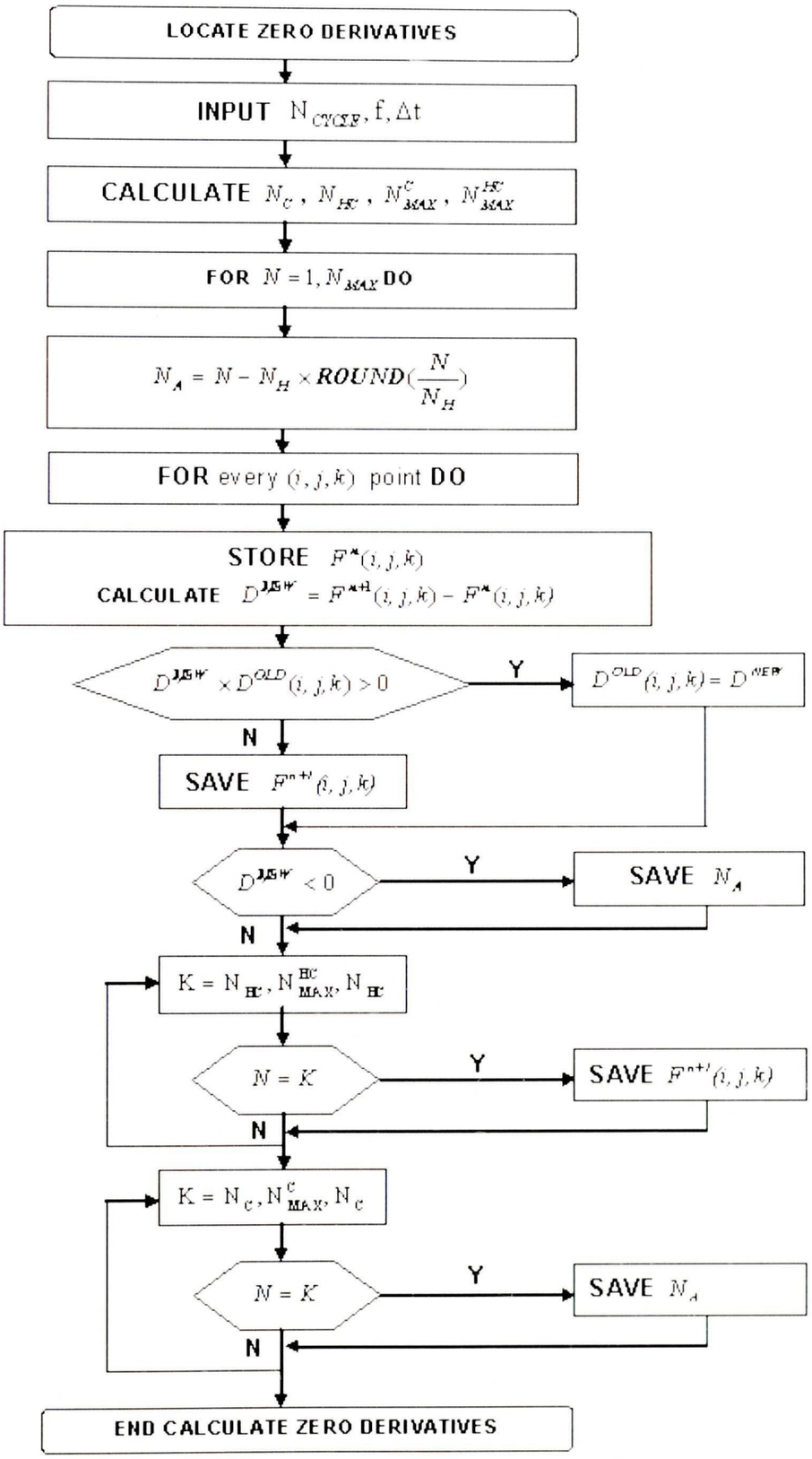

Figure 5.3.2: Algorithm for testing the time harmonic solution based on the phase information

In order to achieve a steady state sinusoidal solution in the FD-TD method, the information about the peak positive and negative excursions of the fields over a complete cycle of the incident wave have to be observed. Every time step, the desired field waveform E_x, E_y and E_z components are checked for the change of sign of the time derivative respectively.

§5.3.1.3 Criteria based on the numerical integration of a time-dependent signal over one period

De Pourcq[43] suggested a simple algorithm for derivation of the sinusoidal steady-state amplitude.

After turning on the sinusoidal steady state source at $t = 0$, he assumes that the steady-state is reached at t_0. Then a function $f(t)$ can be written as

$$f(t) = a + A\,cos(\omega t + \theta) \tag{5.3.2}$$

where a is the DC component, A is the amplitude and θ is the phase. These three variables can be derived from the following expressions

$$\frac{1}{T}\int_{t0}^{t0+T} f(t)dt = a \tag{5.3.3}$$

$$\frac{1}{T}\int_{t0}^{t0+T} f(t)cos(\omega t)dt = \frac{A}{2}cos\theta \tag{5.3.4}$$

$$\frac{1}{T}\int_{t0}^{t0+T} f(t)sin(\omega t)dt = -\frac{A}{2}sin\theta \tag{5.3.5}$$

where $T = N\Delta t$ is the signal period. The left-hand side of the Equations 5.3.3-5.3.5 is calculated by means of a numerical integration, which is based on the linear interpolation of $f(t)$ in each time interval Δt. When they are discretised the Equations

5.3.3-5.3.5 take the following form

$$\frac{1}{N}\sum_{i=1}^{N} f(t_i) = a \tag{5.3.6}$$

$$\frac{N}{\pi^2}(1 - cos(\omega\Delta t))\sum_{i=1}^{N} f(t_i)cos(\omega t_i) = Acos\theta \tag{5.3.7}$$

$$\frac{N}{\pi^2}(1 - cos(\omega\Delta t))\sum_{i=1}^{N} f(t_i)cos(\omega t_i) = Acos\theta \tag{5.3.8}$$

The summation in Equations 5.3.6-5.3.8 is performed by adding the new terms at each time step and the sum is kept in store.

§5.3.1.4 Criteria based on the relative change in the total sum of the power distribution

This approach is based of checking each time step the convergence of the total sum of the heating function over the entire biomaterial i.e.

$$I^n = \int_V dV = \frac{1}{2}\sum_{i,j,k} \sigma_{eff}(i,j,k)|E_{max}(i,j,k)|^2 \Delta x_i \Delta y_j \Delta z_k. \tag{5.3.9}$$

This approach was favored here for obtaining the results. It proved to be very reliable and reduced significantly the cost by stopping the electromagnetic solver once the time harmonic solution has been reached. In this work the relative change of 1% was used.

§5.3.2 Update of electromagnetic field information

The second issue to be addressed in the coupling algorithm is how to update the electromagnetic field information for this nonlinear process. There are many issues

related to determining when the microwave power should be recalculated. Since ϵ'_r basically characterizes the phase of the microwaves interacting with the material and ϵ''_{eff} determines the penetration depth and the attenuation of the microwaves, the relative permittivity ϵ'_r will dominate the electromagnetic field behavior inside the system. Once the microwave heating is set, the only factor that can change during the heating process is the properties of the material. Since a small change in dielectric properties can induce a significant change in power distribution, the maximum percentage change in the dielectric property will be the most significant factor in controlling the nonlinear process. This factor is defined as

$$\psi = \mathbf{max}_{i \in P} \left(\frac{\mid \epsilon_i^{n+1} - \epsilon_i^n \mid}{\mid \epsilon_i^n \mid} \right) \tag{5.3.10}$$

where ψ is a factor (%). The condition

$$\psi \geq \psi_c \tag{5.3.11}$$

determines when the microwave power should be recalculated. The smaller ψ_c value the more accurate the temperature solution. Care should be taken with this constraint because it is very expensive in terms of CPU time, to compute the microwave power distribution in comparison to the time for calculating the temperature and moisture distribution. Generally, for optimal processing times, it is recommended that ψ_c takes a value in the range between 1% and 10%.

§5.4 Mesh mapping

The cavity and the waveguide are meshed for the FD-TD computation with a tensor–product cartesian mesh. Since the conductivity of air is approximated to be zero, the heating function (see Equation 4.1.5) will have non-zero values only for the biomaterial region. For this reason, the FV mesh used for calculating the heat and mass transfer has to be constructed only for the region of the biomaterial. Since the two meshes are independent, a transfer function (conserving the total Q for the

biomaterial) is used to map the heating function Q from the FD-TD mesh to the heat and mass transfer mesh[81]. The schematic picture of the mapping is shown in Figure 5.4.1. The mapping is straight forward because both the FD-TD and FV meshes are structured and cell-centered.

§5.4.1 Computational Considerations

Finite difference simulations with Yee's algorithm are computationally intensive. The maximum step size for stable results is $\lambda/10$ which, at optical wavelengths of approximately $1\,\mu m$ is $0.1\,\mu m$. The modelling of structures with dimensions of typical cells requires the storage of large arrays. In a three-dimensional simulation, arrays for 6 field components, ϵ, and σ must be stored in memory. In addition all 6 field components and the incident source must be computed at all grid points for each time step. The approximate amount of memory required for a simulation is

$$App.Mem = N_x N_y N_z[(6 \times 8) + 8] \tag{5.4.1}$$

where N_x, N_y, and N_z are the array dimensions in each direction. Equation 5.4.1 assumes that the 6 field components and permittivity are stored as double precision floating point values requiring 8 bytes of memory each. A three-dimensional simulation of a volume $15\,\mu m$ on a side ($N = 200$) would require $450\,Mb$ of memory according to Equation 5.4.1. The actual amount of memory will be greater than this since it does not take into consideration storage of variables for boundary conditions and far field transform.

A two-dimensional simulation on the other hand, requires storage of arrays for 3 field components and permittivity with only N^2 elements, as opposed to N^3 elements in three dimensions. Large areas ($\sim 50\,\mu m$ on a side) can be simulated with modest storage requirements ($< 100\,Mb$).

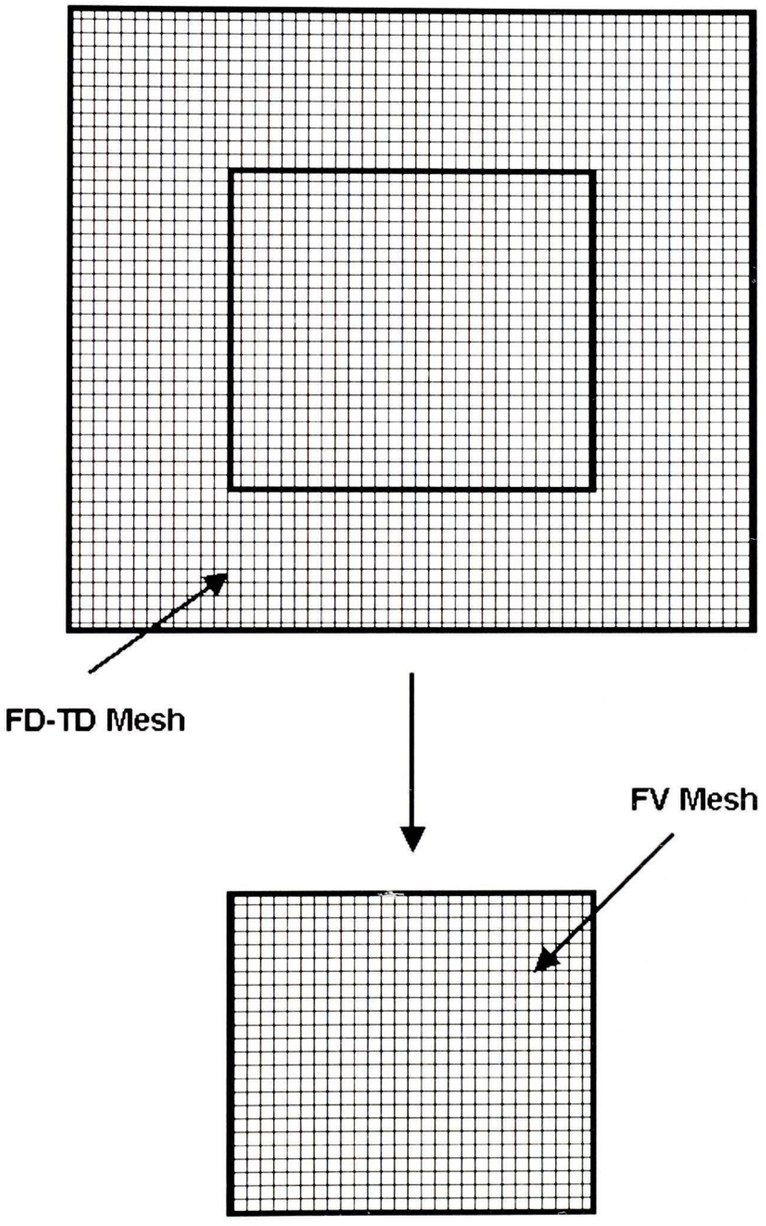

Figure 5.4.1: Mapping between FD-TD and FV meshes

CHAPTER

SIX

2-D Computational Results

In this chapter 2-D computational results are presented. In the first section examples of electromagnetic field components obtained from the Yee's scheme are compared with analytical solutions for uniform and non-uniform structured meshes.

The chapter continues with the power distribution in a 2-D cavity obtained using different structured uniform and non-uniform meshes. The 2-D electromagnetic solver is then coupled to a thermal model through temperature dependent dielectric properties. The temperature distribution is obtained using the Theta differencing scheme for the FV method. The temperature distribution in a biomaterial using this author's coded coupled 2-D model is compared with the one obtained using PHOENICS to solve the heat transfer equations. Finally, in the last section of this chapter a fully coupled 2-D electromagnetic-heat-mass transfer with temperature and moisture dependent dielectric properties is discussed.

§6.1 Validation Example

In this section the results for electro-magnetic field components obtained using the Yee's scheme are compared with the results obtained analytically[82]. A two-dimensional case, of uniform cross section with normalized dimensions 1×1 is considered. The simplest TE mode of propagation in a rectangular wave guide is observed. The walls were taken to be perfect conductors and $\epsilon_r' = 1$. For all calculations the impedance is normalized

$$Z = \sqrt{\frac{\mu_0}{\epsilon_0}} = 1. \tag{6.1.1}$$

The following set of equations for electric and magnetic field components will satisfy Maxwell's equations

$$E_x(x, y, t) = -\frac{4}{5}\cos(3\pi x - 5\pi t)\sin(4\pi y) \tag{6.1.2}$$

$$E_y(x, y, t) = \frac{3}{5}\sin(3\pi x - 5\pi t)\cos(4\pi y) \tag{6.1.3}$$

$$H_z(x, y, t) = \sin(3\pi x - 5\pi t)\cos(4\pi y). \tag{6.1.4}$$

The following boundary and initial conditions are applied

$$E_x(x, y, \frac{\Delta t}{2}) = -\frac{4}{5}\cos(3\pi x - \frac{5\pi\Delta t}{2})\sin(4\pi y) \tag{6.1.5}$$

$$E_y(x, y, \frac{\Delta t}{2}) = \frac{3}{5}\sin(3\pi x - \frac{5\pi\Delta t}{2})\cos(4\pi y) \tag{6.1.6}$$

$$H_z(x, y, 0) = \sin(3\pi x)\cos(4\pi y) \tag{6.1.7}$$

$$E_x(x, 0, t) = 0 \tag{6.1.8}$$

$$E_y(x, 1, t) = 0 \tag{6.1.9}$$

$$E_y(0, y, t) = -\frac{3}{5}\sin(5\pi t)\cos(4\pi y) \tag{6.1.10}$$

$$E_y(1, y, t) = \frac{3}{5}\sin(3\pi - 5\pi t)\cos(4\pi y). \tag{6.1.11}$$

The set of equations 6.1.2-6.1.4 are then solved using the Yee's scheme described in the previous chapter. For each field component, the error is measured against the exact solution of the field component in the L_2 norm, which for a two-dimensional situation, is given in by the following formula

$$\| \, error \, \|_{L_2} = \sqrt{\sum_{i,j} \left(H_z^{exact}(i, j) - H_z^{yee}(i, j)\right)^2} \tag{6.1.12}$$

Similar formulae are used for the calculation of the L_2 errors of the remaining two components.

§6.1.1 Results for uniform structured meshes

Uniform grid spacing was chosen for FD-TD discretization of the Equations 6.1.2. Three different mesh sizes are used for the calculations

$$\delta = \Delta x = \Delta y = \frac{1}{20 \times 2^s}, \quad s = 0, 1, 2. \tag{6.1.13}$$

The time step was set to be

$$\Delta t = \frac{2\delta}{3} \tag{6.1.14}$$

δ	$\text{Log}_{10}\delta$	Δt	$Max(\|\|error\|\|_{L_2})$	$\text{Log}_{10}(Max(\|\|error\|\|_{L_2}))$	$rate$
$\frac{1}{20}$	-1.3	$\frac{1}{30}$	0.19105968074892	-0.71883095227381	
$\frac{1}{40}$	-1.6	$\frac{1}{60}$	4.8184483898169D-02	-1.3170927883638	1.9942061203
$\frac{1}{80}$	-1.9	$\frac{1}{120}$	1.2018123209225D-02	-1.9201633479337	2.0102351986

Table 6.1: The maximal errors in L_2 norm for $H_z(x, y, t)$ - uniform mesh

δ	$\text{Log}_{10}\delta$	Δt	$Max(\|\|error\|\|_{L_2})$	$\text{Log}_{10}(Max(\|\|error\|\|_{L_2}))$	$rate$
$\frac{1}{20}$	-1.3	$\frac{1}{30}$	0.15337622304758	-0.81424196111450	
$\frac{1}{40}$	-1.6	$\frac{1}{60}$	3.7948576056417D-02	-1.4208045154850	2.021875163
$\frac{1}{80}$	-1.9	$\frac{1}{120}$	9.4684171812906D-03	-2.0237226151767	2.0097270167

Table 6.2: The maximal errors in L_2 norm for $E_x(x, y, t)$ - uniform mesh

δ	$\text{Log}_{10}\delta$	Δt	$Max(\|\|error\|\|_{L_2})$	$\text{Log}_{10}(Max(\|\|error\|\|_{L_2}))$	$rate$
$\frac{1}{20}$	-1.3	$\frac{1}{30}$	0.11715624132197	-0.93123457006752	
$\frac{1}{40}$	-1.6	$\frac{1}{60}$	2.8881641405108D-02	-1.5393781285219	2.027145195
$\frac{1}{80}$	-1.9	$\frac{1}{120}$	7.2047999722036D-03	-2.1423780720567	2.0099995717

Table 6.3: The maximal errors in L_2 norm for $E_y(x, y, t)$ - uniform mesh

in order to satisfy the stability condition given by Equation 5.2.

The convergence rate of the L_2 spatial error in the maximum norm over the time [0,10] is shown in Figure 6.1.1. Calculated values are shown in Tables 6.1.1 - 6.1.1. The obtained results show that the slope of the line for the Yee's scheme converges to 2 confirming the second order accuracy.

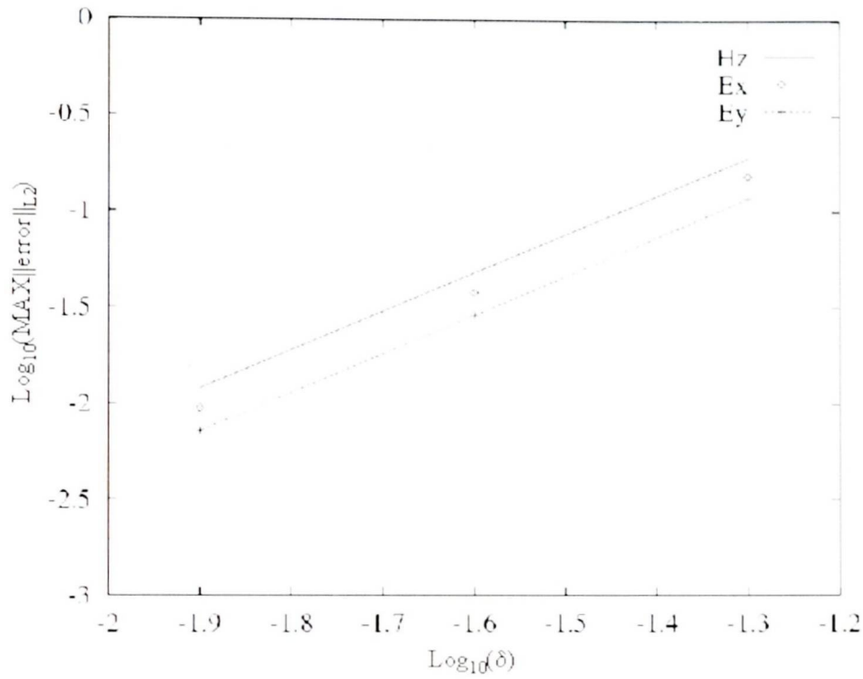

Figure 6.1.1: $\mathrm{Log}_{10}(Max(\|error\|_{L_2}))$ for a 2-D uniform structured mesh as a function of $\mathrm{Log}_{10}\delta$ for H_z, E_x, E_y

§6.1.2 Results for nonuniform structured mesh

In this section, for the same cavity, a now non-uniform grid spacing was chosen. The computational domain is solved using three different meshed having $(20 \times 2^s) \times (20 \times 2^s)$ $(s = 0, 1, 2)$ mesh points. The mesh size in the non-refined region is $\delta = \Delta x = \Delta y = \frac{1}{2 \times 20^s}$ $(s = 0, 1, 2)$ and $\delta/2$ in the refined region. The refined region takes place between the nodes $7 \times 2^s - 13 \times 2^s$ $(s = 0, 1, 2)$, respectively. The time step is now set to be

$$\Delta t = \frac{\delta}{3}. \tag{6.1.15}$$

The convergence rate of the L_2 spatial error in the maximum norm over the time [0,10] is again calculated. Results for the electric and magnetic field components

$\frac{\delta}{2}$	$\text{Log}_{10}\delta$	Δt	$\text{Log}_{10}(Max(\|error\|_{L_2}))$	$rate$
$\frac{1}{68}$	-1.8325089127062	$\frac{1}{204}$	-0.648901933625 46	
$\frac{1}{136}$	-2.1335389083702	$\frac{1}{408}$	-1.2406244318794	1.9656595913
$\frac{1}{272}$	-2.4345689040342	$\frac{1}{916}$	-1.8418338002266	1.9971742916

Table 6.4: The maximal errors in L_2 norm for $H_z(x, y, t)$ - nonuniform mesh

$\frac{\delta}{2}$	$\text{Log}_{10}\delta$	Δt	$\text{Log}_{10}(Max(\|error\|_{L_2}))$	$rate$
$\frac{1}{68}$	-1.8325089127062	$\frac{1}{204}$	-0.7415262112127	
$\frac{1}{136}$	-2.1335389083702	$\frac{1}{408}$	-1.3405155057722	1.9966309819
$\frac{1}{272}$	-2.4345689040342	$\frac{1}{916}$	-1.9425392143550	2.0067456953

Table 6.5: The maximal errors in L_2 norm for $E_x(x, y, t)$ - nonuniform mesh

$\frac{\delta}{2}$	$\text{Log}_{10}\delta$	Δt	$\text{Log}_{10}(Max(\|error\|_{L_2}))$	$rate$
$\frac{1}{68}$	-1.8325089127062	$\frac{1}{204}$	-0.8671398488086	
$\frac{1}{136}$	-2.1335389083702	$\frac{1}{408}$	-1.4664275915696	1.9976258092
$\frac{1}{272}$	-2.4345689040342	$\frac{1}{916}$	-2.0685207426194	2.0069771702

Table 6.6: The maximal errors in L_2 norm for $E_y(x, y, t)$ - nonuniform meshes

are shown in Tables 6.1.2 - 6.1.2. The obtained results show that for non-uniform structured meshed the Yee's scheme converges to 2 as well (see Figure 6.1.2).

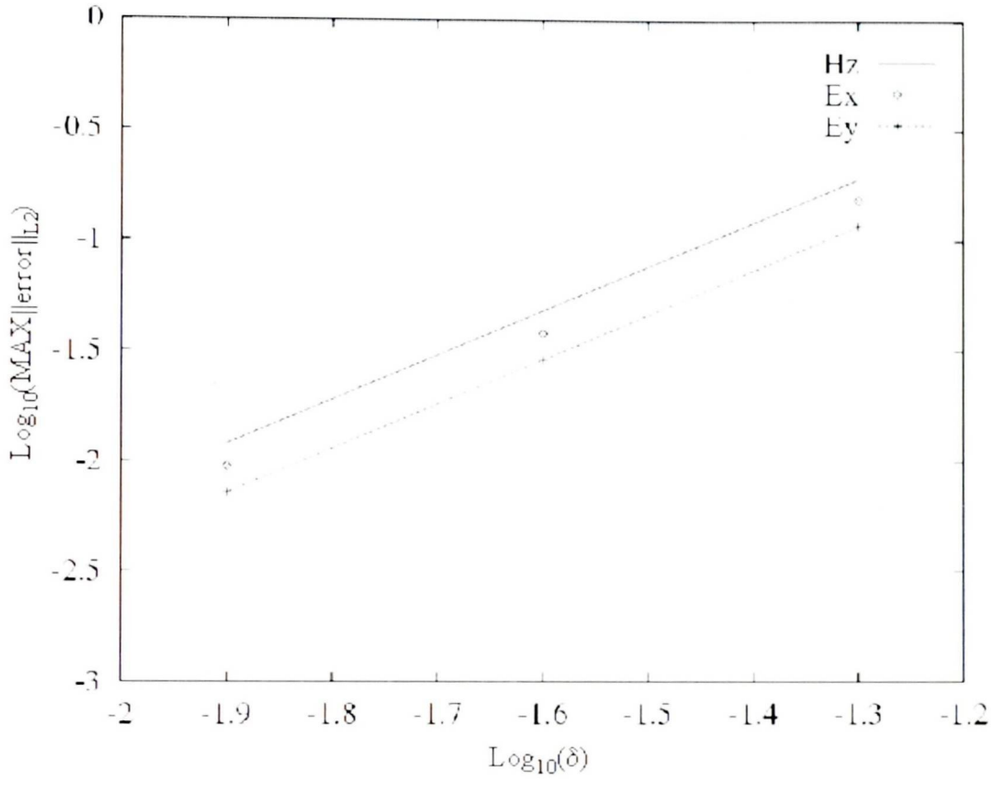

Figure 6.1.2: $\mathrm{Log}_{10}(Max(\|error\|_{L_2}))$ for a 2-D non-uniform structured mesh as a function of $\mathrm{Log}_{10}\delta$ for H_z

§6.2 2-D Electromagnetic distribution

In this section the 2-D power distribution is computed. The microwave oven model used in this example consists of microwave cavity containing a rectangular block of porous biomaterial, Figure 6.2.1. It is of uniform cross section and infinite extent in z-direction. A TE mode excitation field was considered, i.e.

$$E = (E_x(x, y, t), E_y(x, y, t), 0) \tag{6.2.1}$$

$$H = (0, 0, H_z(x, y, t)) \tag{6.2.2}$$

The perfectly conducting boundary conditions (Equation 3.5.1 and 3.5.2) are applied at all boundaries except for the waveguide inlet, where

$$E_y(x, y, t) = E_0 sin\omega t \tag{6.2.3}$$

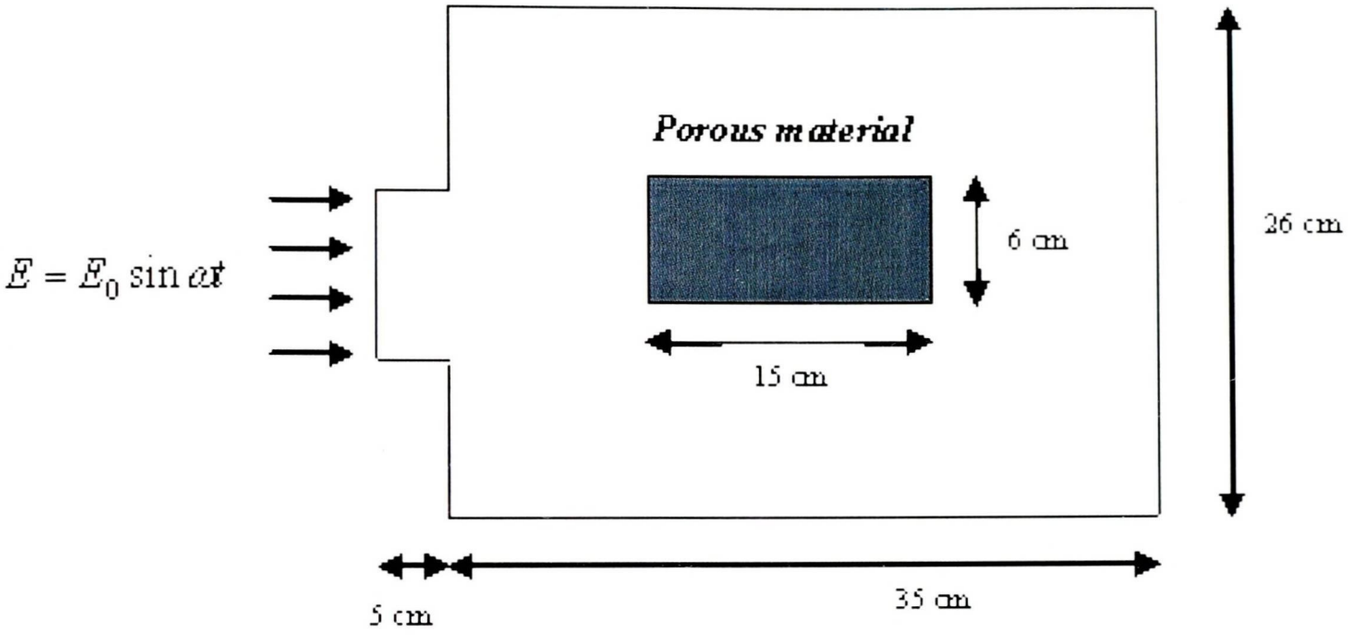

Figure 6.2.1: 2-D Microwave Oven Model

The amplitude of the incident electric field, E_0 was chosen to be $100\,kV$, and the frequency is taken to be $f = 2450\,MHz$, i.e. $\omega = 2\pi f$. A uniform mesh 25×40 is chosen with $\delta = 1\,cm$. The stability condition (Equation 5.2) imposes

$$\Delta t < 2.36 \times 10^{-11} \text{ seconds.} \tag{6.2.4}$$

Consequently the time step is chosen to be $\Delta t = 2.3 \times 10^{-11}$. Dielectric properties are those for mashed potato at $T = 20^oC$: $\epsilon_r' = 65.1$ and $\epsilon_{eff} = 19.6$ (see Figure 1.2.2). The dielectric was placed symmetrically with respect to the excitation and is placed between nodes $16 - 30$ in the x direction and $9 - 17$ in the y direction. The waveguide is positioned between the nodes 10 and 16 in the y direction and is as wide as 5δ.

The time evolution of the electric field inside and outside the biological material is shown Figures 6.2.2 and 6.2.3, respectively. It can be seen that the magnitude of the electric field strength is attenuated in the dielectric due to absorption. The field in the biomaterial becomes steady after 1.035×10^{-7} seconds , corresponding to roughly 4300 time steps. The convergence of the relative change in the total sum of the power distribution (Figure 6.2.4) as described in Section 5.3.1.4 was used as

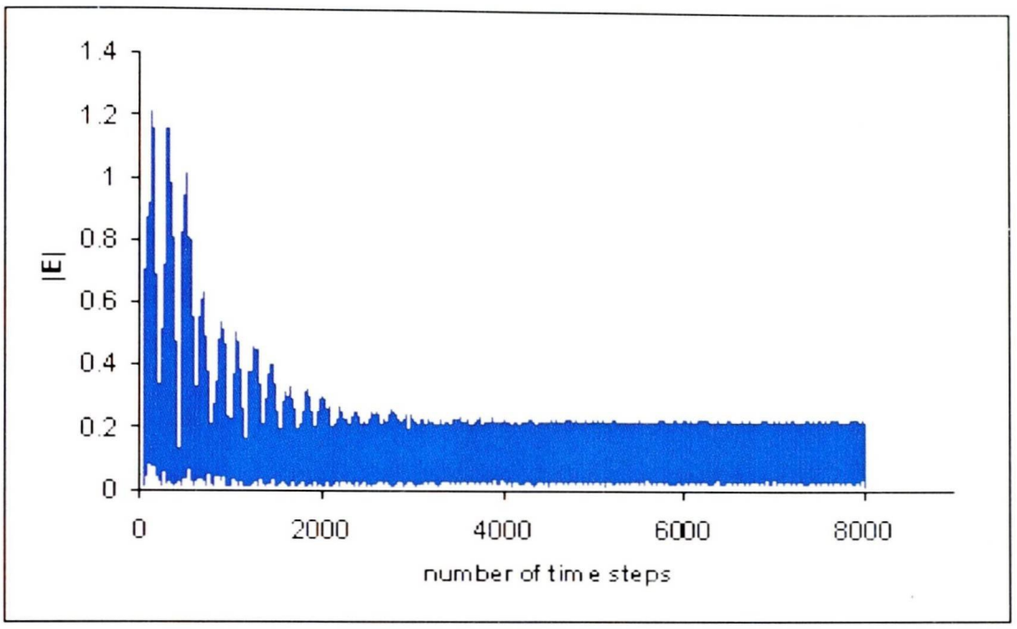

Figure 6.2.2: Electric field variation at an arbitrarily chosen point inside the biomaterial

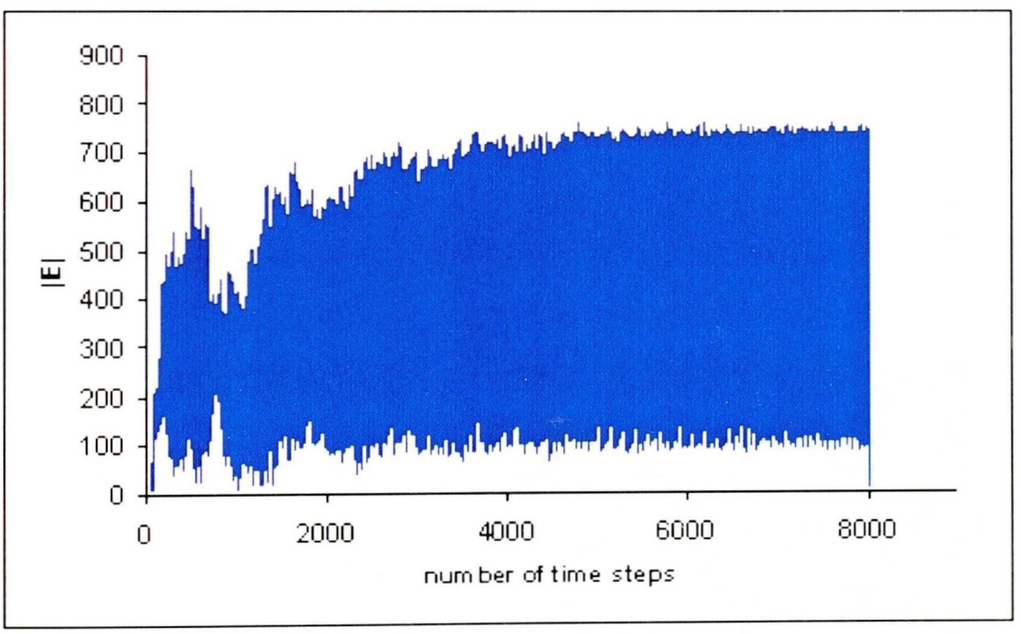

Figure 6.2.3: Electric field variation at an arbitrarily chosen point outside the biomaterial but inside the cavity

a criteria for stopping the iterations. Relative change of 1% was chosen. Figures 6.2.6 and 6.2.5 show a typically irregular electric field distribution inside the oven, in this case accentuated by the corners of the biomaterial. (In practice various mechanisms for smoothing this distribution are used, e.g. stirring, curved packaging, magnetron placement and our approach will be extended to include them). The field

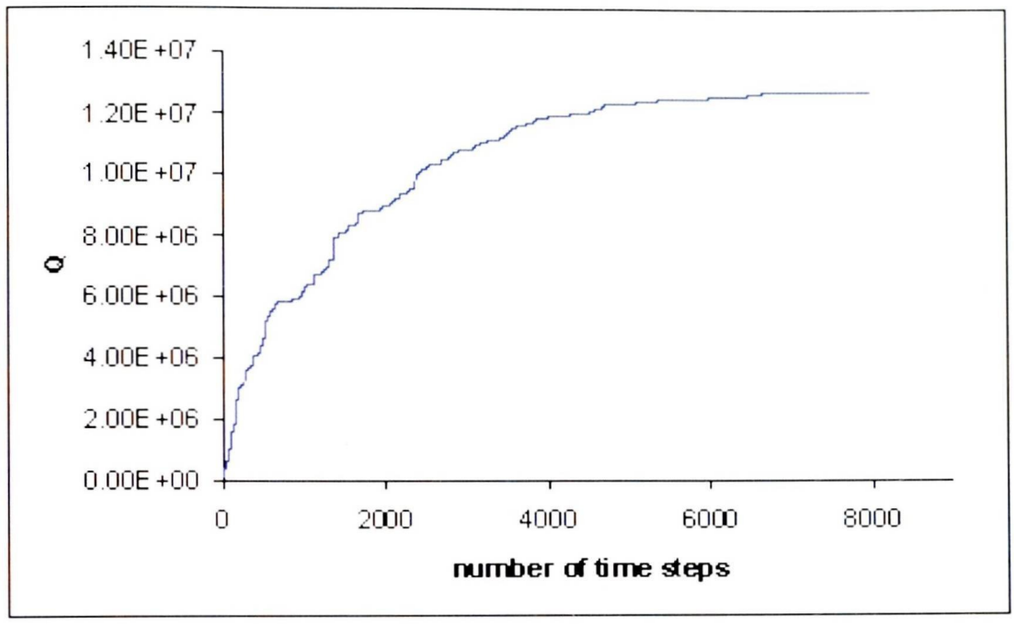

Figure 6.2.4: Convergence history of the total heating I

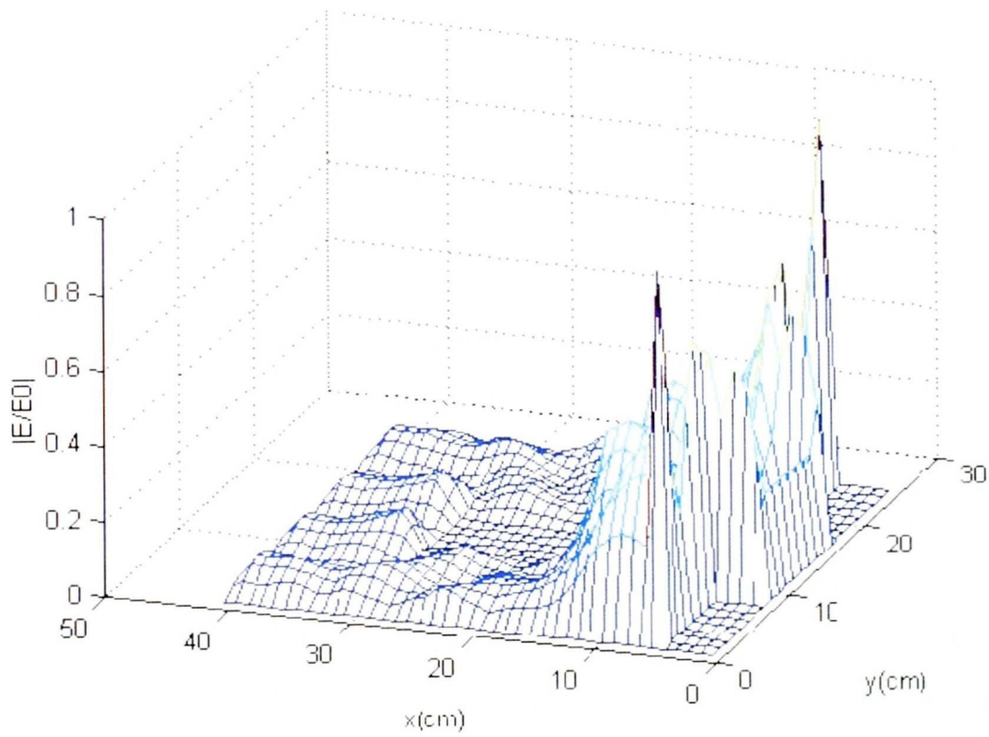

Figure 6.2.5: Electric field distribution inside the microwave oven-snapshot

distribution is relatively large near the waveguide and virtually zero and very flat inside the biomaterial where the fields are exponentially attenuated with consequent heating of the material.

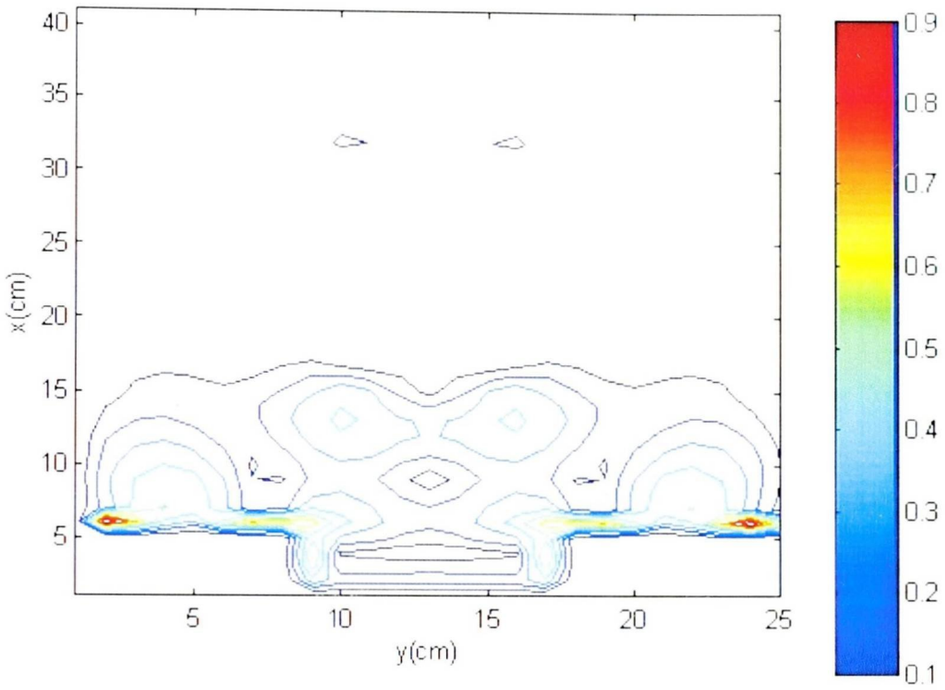

Figure 6.2.6: Contour plot of the electric field distribution inside the oven

The distribution of the heating function, Q, is shown in Figure 6.2.7. The conductivity is identically zero in the air-space, so there is zero heating there. The heating function is fairly smooth inside the material, but on the boundary with the air its value increases, with a dramatic increase at the end nearest the waveguide where there is direct irradiation.

The mesh size is now refined using mesh size $\delta = 0.5\,cm$ and time step was chosen accordingly, $\Delta t = 1.15^{-11}$ seconds. Distribution of the heating function using such a mesh is shown in Figure 6.2.8. Refining the mesh triggers a corresponding increase in the computation time. If there are n_x and n_y grid points in the x and y direction, the total number of nodes is $n_x \times n_y \approx O(n^2)$. The amount of computation in each iteration is proportional to $O(n^2)$, so that the total amount of computation is $O(n^2 t)$.

For the microwave frequency of $2450\,MHz$, the wavelength $\lambda = 12.2\,cm$. It is convenient to have roughly 10 cells per wavelength. The penetration depth defined by

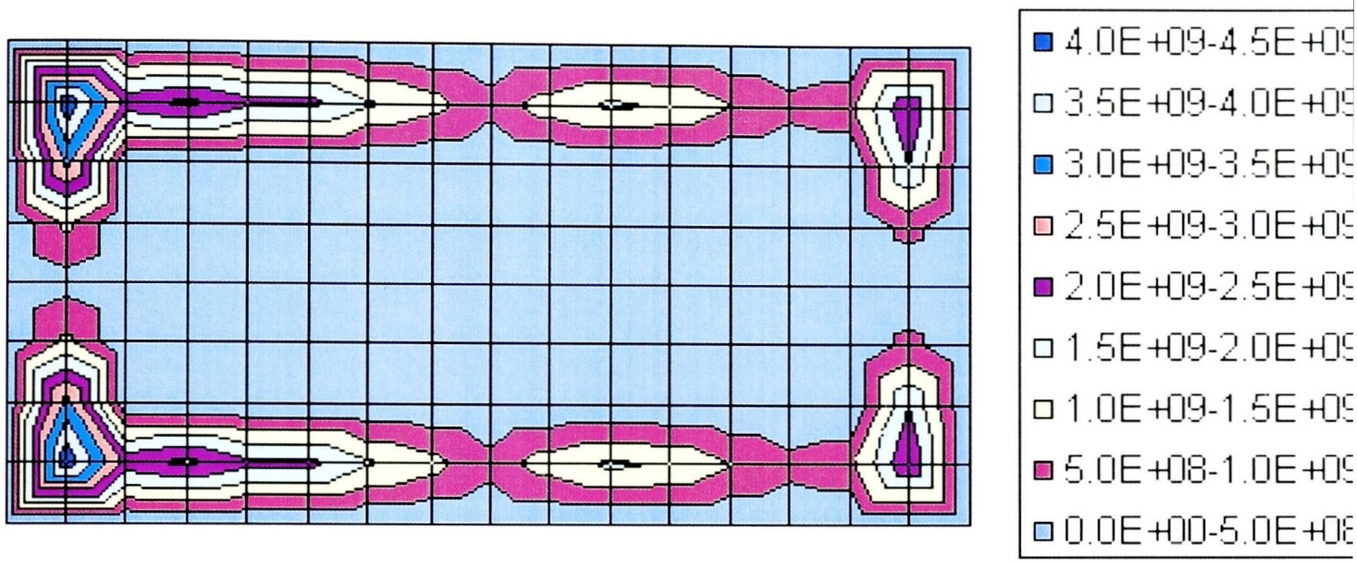

Figure 6.2.7: Heating function, Q, inside the biomaterial for $\delta = 1\,cm$

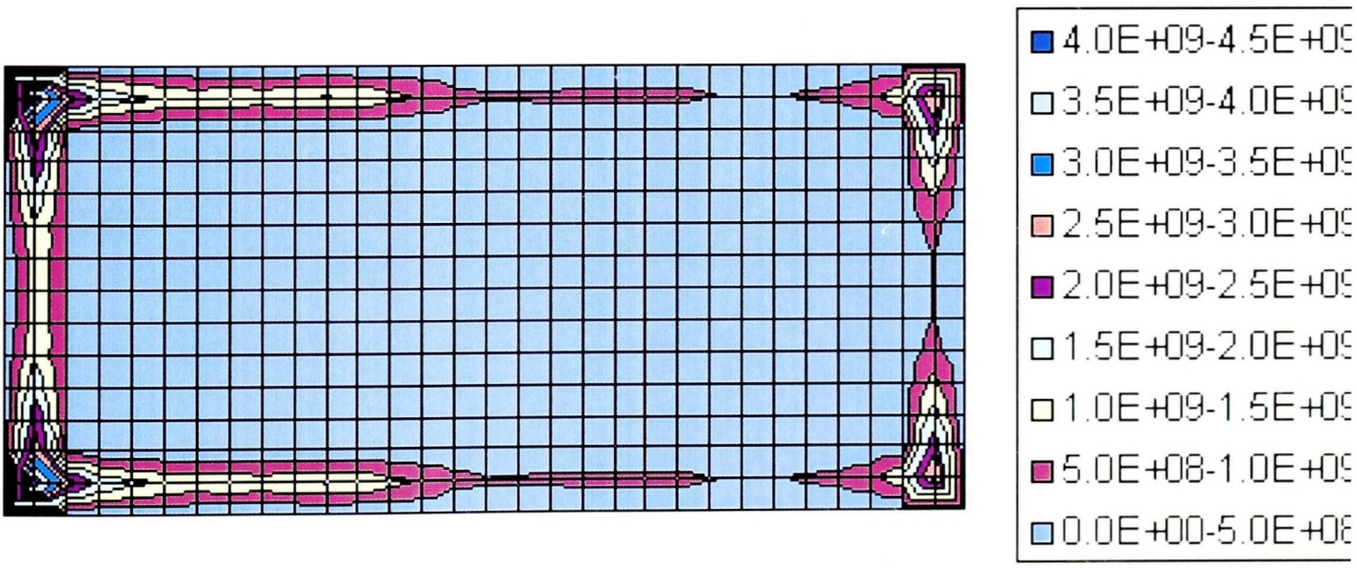

Figure 6.2.8: Heating function, Q, inside the biomaterial for $\delta = 0.5\,cm$

the Equation 1.2.16 is approximately $0.7\,cm$.

§6.3 2-D Electromagnetic-thermal results

In this section coupled 2-D electro-thermal results are presented[83]. Taking into account the increase in the computational time for finer meshes, a nonuniform mesh was then chosen here. The calculations are faster and the accuracy is as good as for finer meshes. The mesh size of $1\,cm$ was chosen outside and $0.5\,cm$ inside the lossy material. The time step was chosen to be again $\Delta t = 1.15^{-11}$ seconds.

A 2-D heat transfer solver is developed by the author. The 2-D unsteady heat transfer equation[51] is solved using FV method. The diffusion term is neglected and it's assumed that the heat transfer is due to convection only. The Theta Method[51] is used for representing the partial-differential equation as a difference equation

$$\int_{t}^{t+\Delta t} T_{i,j}\,dx = [\theta T_{i,j}^{n+1} + (1-\theta)T_{i,j}^{n}]\Delta t. \tag{6.3.1}$$

where

$$\theta = 0.5 + \varsigma \tag{6.3.2}$$

and

$$\varsigma = 0.01 \tag{6.3.3}$$

In this example $\theta \geq \frac{1}{2}$. The mesh is stable for any Δt. The interface conductivity is computed as the harmonic mean of two neighboring values.

The solution of the discretized equation obtained this way is obtained using a line-by-line method known as the *Alternating-Direction Implicit* (A.D.I). Here, the A.D.I. method is expanded in two dimensions and makes use of the TDMA[51] (Three-

T_{max}	ϵ'_r	$t(seconds)$
20.00	65.1	
29.83	63.03	11
39.59	61.08	12
49.14	59.17	13
58.33	57.33	14
67.07	55.59	15
75.79	53.84	17
84.27	52.15	19

Table 6.7: Time intervals at which the electric properties are updated

Diagonal-Matrix Algorithm). The direction is alternated after each iteration traverses. When system of linear equations in matrix form $A \cdot X = B$ is solved, for each time step iteration k the following three criteria are checked

1. $k > 100$
2. $\|r\|_2 < \tau_1$, where $r^k = A \cdot X^k - B$
3. $\frac{\|X^{k+1} - X^k\|_2}{\|X^k\|_2} < \tau_2$.

In this example $\tau_1 = 10^{-6}$ and $\tau_2 = 10^{-3}$ and the time step for the thermal solver is one second.

The thermal algorithm is coupled to the electromagnetic solver and the solution technique described in Section 5.3 was used. The temperature dependence of the relative dielectric constant and the dielectric loss for reconstituted potato starch are used from literature (See Figure 1.2.2). Other properties of the biomaterial can be found in Table 7.11. The biomaterial was heated for $t = 101$ seconds, recalculating the power distribution every time the maximum relative change in the dielectric properties over the whole biomaterial region is greater than 10%. Typical change of ϵ'_r with temperature and the times of recalculation of the electromagnetic solver are shown in Table 6.7. Figure 6.3.1 shows the temperature distribution inside the material after $t = 101$ seconds. This distribution is checked against the distribution

obtained by coupling the electromagnetic solver with PHOENICS and using the same conditions (Figure 6.3.2). As it can be noticed the agreement between the two sets of results is excellent.

A disadvantage of this approach is that electrical properties are not calculated for each cell, but they are set as a constant for the whole biomaterial. When the maximum relative change in dielectric properties is detected (it will happen at the position of the maximum temperature change), the electromagnetic solver is rerun using the new value for the electrical properties for the whole region. Consequently, it is not possible to observe the penetration of microwaves, because the heating functions changes globally and not locally.

In the next section a more refined simulation where the electrical properties are updated independently for each cell is presented.

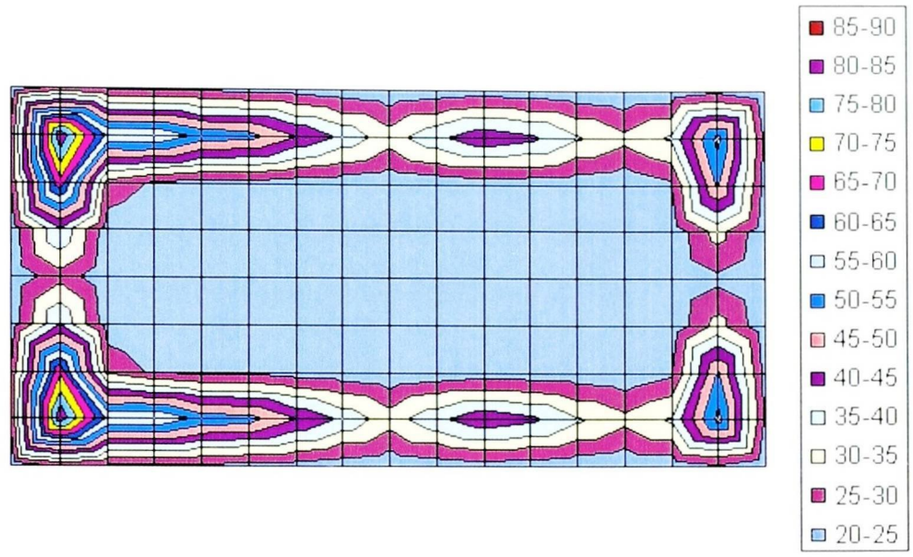

Figure 6.3.1: Temperature distribution, $T(^oC)$, in the biomaterial after 101 seconds calculated using the author's developed 2-D model

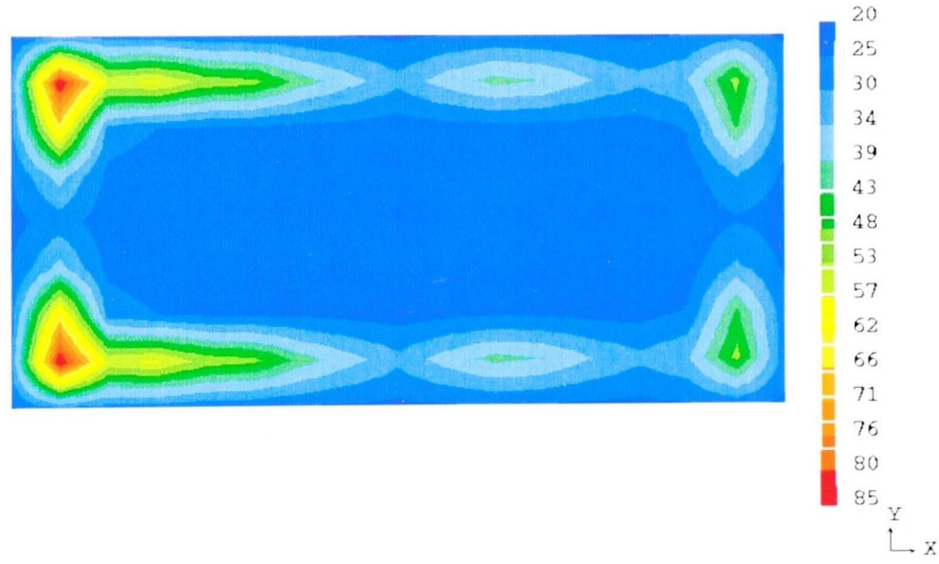

Figure 6.3.2: Temperature distribution, $T(^oC)$, in the biomaterial after 101 seconds calculated using PHOENICS to solve the HTE

§6.4 2-D electromagnetic-heat-mass transfer

The electro-thermal algorithm in this section has been coupled to the mass transfer equation to produce a fully coupled 2-D algorithm[84]. The two HTEs corresponding for each phase (see Equations 4.4.2 and 4.4.3) were solved together with the corresponding mass transfer equations 4.5.2 and 4.5.3.

Results are shown for a simple biomaterial with material properties set to those of mashed potato density porosity $\phi = 0.40$, 90% of which is assumed to be liquid at the beginning. The dielectric properties were assumed to be both temperature and moisture dependent. The temperature dependence is described in the previous section, while the moisture dependence and implementation of the Darcy's law is discussed in Chapter 5. The total heating time was 110 seconds. Constant pressure boundary conditions were imposed on each side, the biomaterial surface was assumed to be completely dry.

Figure 6.4 shows the temperature profile in the biomaterial. The hottest spots are on the side closest to the input. Consequently, the liquid concentrations will be low in those regions (see Figure 6.4.2) and the gas concentrations high due to internal evaporation as shown in Figure 6.4.4. Because of the change of phase the gas pressure will build up in those areas which is shown in Figure 6.4.3.

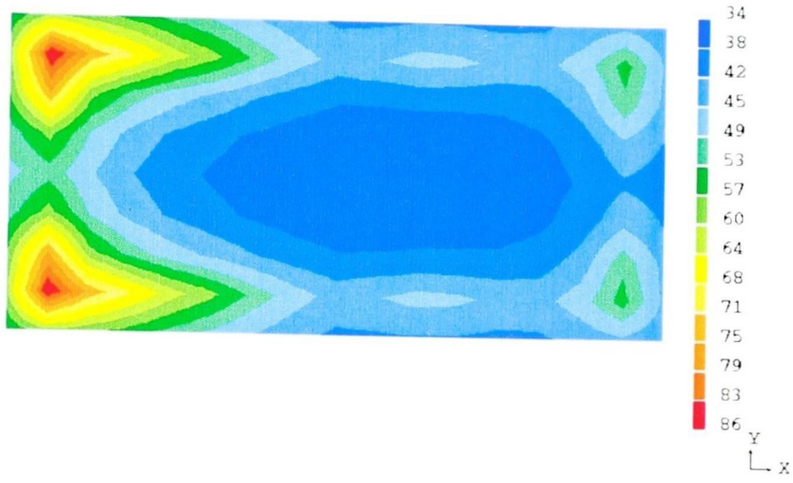

Figure 6.4.1: Temperature distribution, $T(^oC)$, after 110 seconds

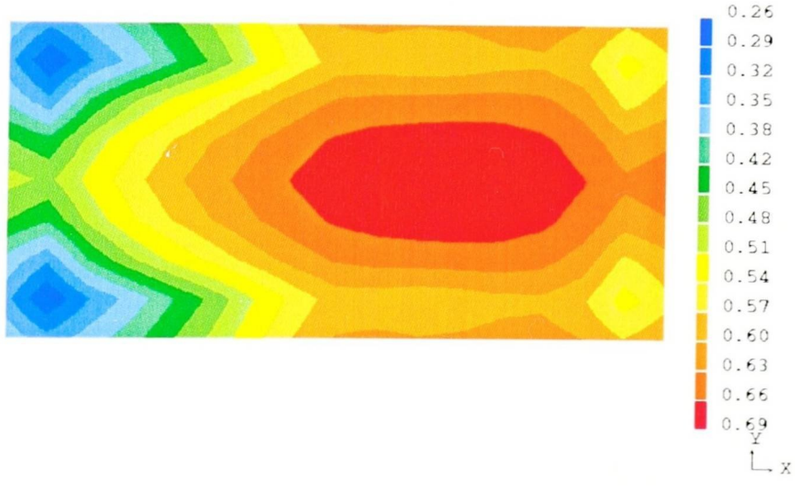

Figure 6.4.2: Moisture distribution, M, after 110 seconds

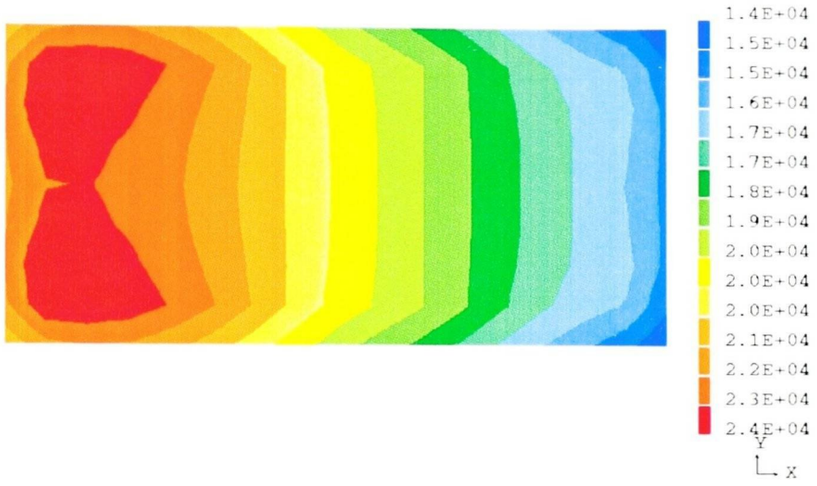

Figure 6.4.3: Dynamic gas pressure, $p(Pa)$, distribution after 110 seconds

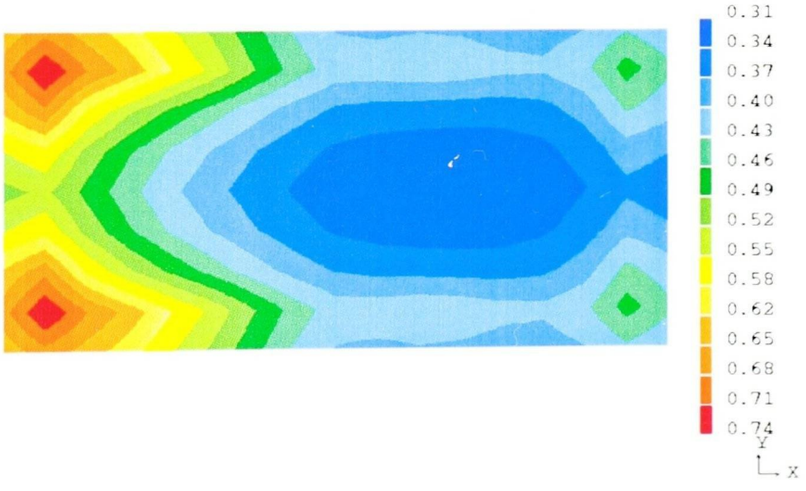

Figure 6.4.4: Gas distribution, $1 - M$, after 110 seconds

CHAPTER

SEVEN

3-D Computational Results

In this chapter 3-D computational results are presented. In the first section a comparison between the analytical and computed results for all fields components in an unloaded rectangular cavity is given and the error is calculated, proving the second order accuracy of the FD-TD scheme. Then computed results for the heating function in a loaded cavity are compared to those of other authors and methods.

The chapter proceeds with the validation of the temperature field using both experimental measurements and results reported in the literature.

The chapter ends with 3-D results obtained with the fully coupled electro-thermal-mass model. The results on coarse and fine meshes are compared.

§7.1 3-D Validation Example

The simplest mode of propagation in a rectangular wave guide was considered. The walls were taken to be perfect conductors i.e $\sigma_{eff} = 0$ and the cavity is filled with air ($\epsilon_r' = 0$). The following set of equations will satisfy the equations 3.1.8-3.1.13[82]

$$H_x(x, y, z, t) = \sin(\omega t)\sin(Ax + By + Cz) \tag{7.1.1}$$

$$H_y(x, y, z, t) = \sin(\omega t)\sin(Ax + By + Cz) \tag{7.1.2}$$

$$H_z(x, y, z, t) = \sin(\omega t)\sin(Ax + By + Cz) \tag{7.1.3}$$

$$E_x(x, y, z, t) = \frac{C - B}{\omega}\cos(\omega t)\cos(Ax + By + Cz) \tag{7.1.4}$$

$$E_y(x, y, z, t) = \frac{A - C}{\omega}\cos(\omega t)\cos(Ax + By + Cz) \tag{7.1.5}$$

$$E_z(x, y, z, t) = \frac{B - A}{\omega}\cos(\omega t)\cos(Ax + By + Cz) \tag{7.1.6}$$

where

$$\omega^2 = A^2 + B^2 + C^2. \tag{7.1.7}$$

For these computations the following values are chosen

$$A = 3\pi \tag{7.1.8}$$

$$B = -2\pi \tag{7.1.9}$$

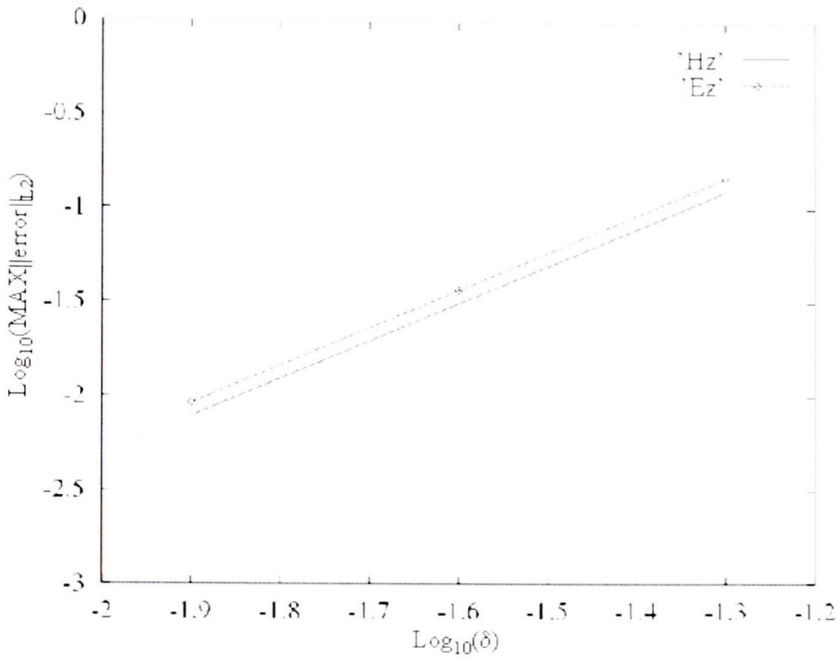

Figure 7.1.1: $\mathrm{Log}_{10}(Max(\|error\|_{L_2}))$ as a function of $\mathrm{Log}_{10}\delta$ for H_z, E_z

$$C = -\pi \tag{7.1.10}$$

$$\omega = \sqrt{14}\pi. \tag{7.1.11}$$

The equations are solved using the 3-D Yee's algorithm and the convergence rate of the L_2 spatial error in the maximum norm over the time [0,10] is calculated (Tables 7.1 - 7.6). Graphical illustration for H_z and E_z field components is given in Figure 7.1.1. The time step is chosen to satisfy the Fourier stability condition (see Equation 5.2.2)

$$\Delta t = \frac{4\delta}{7} \tag{7.1.12}$$

The obtained results show that the slope of the line for the Yee's scheme converges to 2.

δ	$\text{Log}_{10}\delta$	Δt	$Max(\|error\|_{L_2})$	$\text{Log}_{10}(Max(\|error\|_{L_2}))$	$rate$
$\frac{1}{20}$	-1.3	$\frac{1}{35}$	0.12375596929879	-0.907433843941 85	
$\frac{1}{40}$	-1.6	$\frac{1}{70}$	3.1100544429861D-02	-1.5072320083746	1.9993272147758
$\frac{1}{80}$	-1.9	$\frac{1}{140}$	7.773131341889675D-03	-2.1094039939983 6	2.0072399520791

Table 7.1: The maximal errors in L_2 norm for $H_x(x, y, t)$

δ	$\text{Log}_{10}\delta$	Δt	$Max(\|error\|_{L_2})$	$\text{Log}_{10}(Max(\|error\|_{L_2}))$	$rate$
$\frac{1}{20}$	-1.3	$\frac{1}{35}$	0.10602600872703	-0.974587586989 00	
$\frac{1}{40}$	-1.6	$\frac{1}{70}$	2.6596243809881D-02	-1.5751796944904	2.0019736916713
$\frac{1}{80}$	-1.9	$\frac{1}{140}$	6.658668093302093D-03	-2.176612632327 74	2.0047764594578

Table 7.2: The maximal errors in L_2 norm for $H_y(x, y, t)$

δ	$\text{Log}_{10}\delta$	Δt	$Max(\|error\|_{L_2})$	$\text{Log}_{10}(Max(\|error\|_{L_2}))$	$rate$
$\frac{1}{20}$	-1.3	$\frac{1}{35}$	0.12466287553604	-0.904262859675 43	
$\frac{1}{40}$	-1.6	$\frac{1}{70}$	3.1271971293460D-02	-1.5048447412423	2.0019396052229
$\frac{1}{80}$	-1.9	$\frac{1}{140}$	7.830814074708778D-03	-2.106193087268 21	2.0044944867530

Table 7.3: The maximal errors in L_2 norm for $H_z(x, y, t)$

δ	$\text{Log}_{10}\delta$	Δt	$Max(\|error\|_{L_2})$	$\text{Log}_{10}(Max(\|error\|_{L_2}))$	$rate$
$\frac{1}{20}$	-1.3	$\frac{1}{35}$	3.2743638249926D-02	-1.4848730664000	
$\frac{1}{40}$	-1.6	$\frac{1}{70}$	8.2178909270097D-03	-2.0852396272640	2.001221869546
$\frac{1}{80}$	-1.9	$\frac{1}{140}$	2.053113339181222D-03	-2.68758707536281	2.007824826996

Table 7.4: The maximal errors in L_2 norm for $E_x(x, y, t)$

δ	$\text{Log}_{10}\delta$	Δt	$Max(\|error\|_{L_2})$	$\text{Log}_{10}(Max(\|error\|_{L_2}))$	$rate$
$\frac{1}{20}$	-1.3	$\frac{1}{35}$	0.13599566187734	-0.86647494495907	
$\frac{1}{40}$	-1.6	$\frac{1}{70}$	3.4105102469580D-02	-1.4671806412829	2.002352321079
$\frac{1}{80}$	-1.9	$\frac{1}{140}$	8.524194710706845D-03	-2.06934663863642	2.007219991173

Table 7.5: The maximal errors in L_2 norm for $E_y(x, y, t)$

δ	$\text{Log}_{10}\delta$	Δt	$Max(\|error\|_{L_2})$	$\text{Log}_{10}(Max(\|error\|_{L_2}))$	$rate$
$\frac{1}{20}$	-1.3	$\frac{1}{35}$	0.14694490203947	-0.83284547631157	
$\frac{1}{40}$	-1.6	$\frac{1}{70}$	3.6820060202242D-02	-1.4339155057429	2.003566764771
$\frac{1}{80}$	-1.9	$\frac{1}{140}$	9.203914328836006D-03	-2.03602743245091	2.007039755693

Table 7.6: The maximal errors in L_2 norm for $E_z(x, y, t)$

§7.2 3-D Power Distribution Results

The microwave oven model used in this section consists of a simple waveguide and cavity containing a block of porous material of rectangular cross section, as shown in Figure 7.2.1.

A waveguide attached to the centre of one of the cavity faces is used to deliver the excitation field. The input plane of the waveguide is excited in the dominant TE^z_{10} mode with an amplitude of $E_0 = 100\,kV/m$. The source operates at the domestic microwave frequency of $2.45\,GHz$ and is located away from the junction, so that the higher order modes are virtually non–existent. The energy which is reflected back due to a mismatch between the impedance of the waveguide and that of the cavity passes through the excitation plane, which appears transparent, is absorbed by the absorbing boundary plane.

The amplitudes of the incident wave are given by:

$$E_y^{inc} = E_0 \sin \frac{\pi(x - x_0)}{A} \cos(\omega t - \beta z_{k0}) \tag{7.2.1}$$

$$H_x^{inc} = \frac{E_0 \beta}{\omega \mu} \sin \frac{\pi(x - x_0)}{A} \cos(\omega t - \beta\ z_{k0-1/2}) \tag{7.2.2}$$

where x_0, y_0 are the coordinates of the waveguide corner, $z = z_{k_0}$ is the excitation plane (3 mesh intervals away from the absorbing boundary in our model), A is the waveguide x-dimension and β is the mode wave number. Constant dielectric properties were chosen: $\epsilon'_r = 2.0$ and $\epsilon_{eff} = 0.5$. Results for the power distribution are obtained for different slab positions and slab dimension and compared against results obtained by Liu at al.[2] and Bialkowski and Shahan[3] who used the Field Matching Method (FMM). A very good agreement between the two sets of results was noticed.

Figures 7.2.2-7.2.10 show the power distribution in a lossy material for different

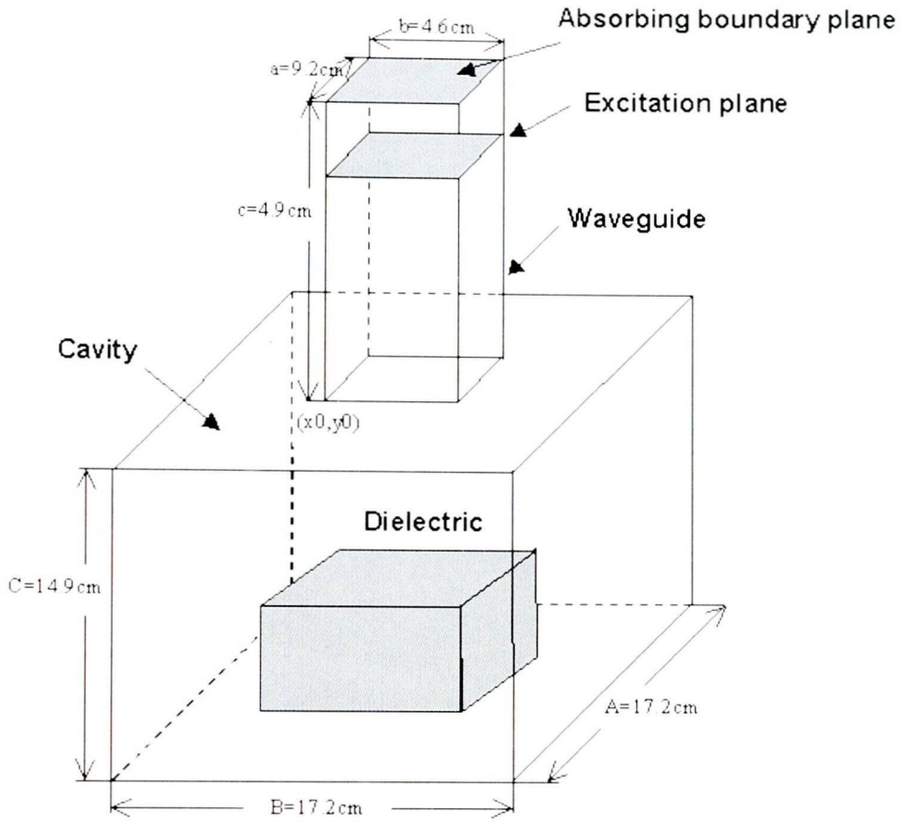

Figure 7.2.1: Microwave oven model

locations within the cavity. The slab occupies the entire cross section of the cavity and has a thickness of 3δ. The power distribution is plotted for the x, y-plane which is one cell size bellow the surface plane facing the waveguide-oven junction. It can be noticed that the power distribution varies greatly with the slab location. For the positions when the dielectric is closer to the waveguide-cavity junction, maximum values are in the centre of the plane (Figure 7.2.10), while for the positions further from the junction, the peak values are at the edges (Figure 7.2.2).

Figures 7.2.12 and 7.2.14 show the results of a partially loaded cavity with slab dimensions $20\delta \times 20\delta \times 3\delta$ located centrally with respect to the waveguide. These power distributions are rather different from those shown in Figures 7.2.10 and 7.2.8, respectively.

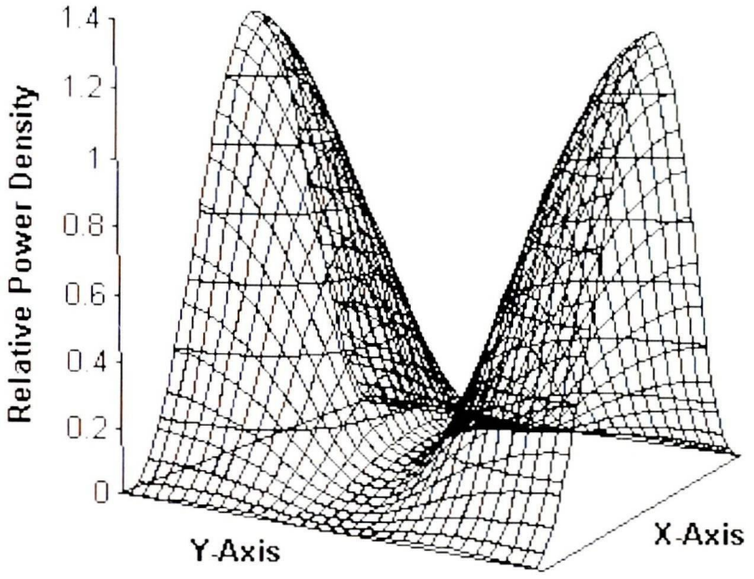

Figure 7.2.2: Power distribution for $z_0 = 23\delta$ - this work

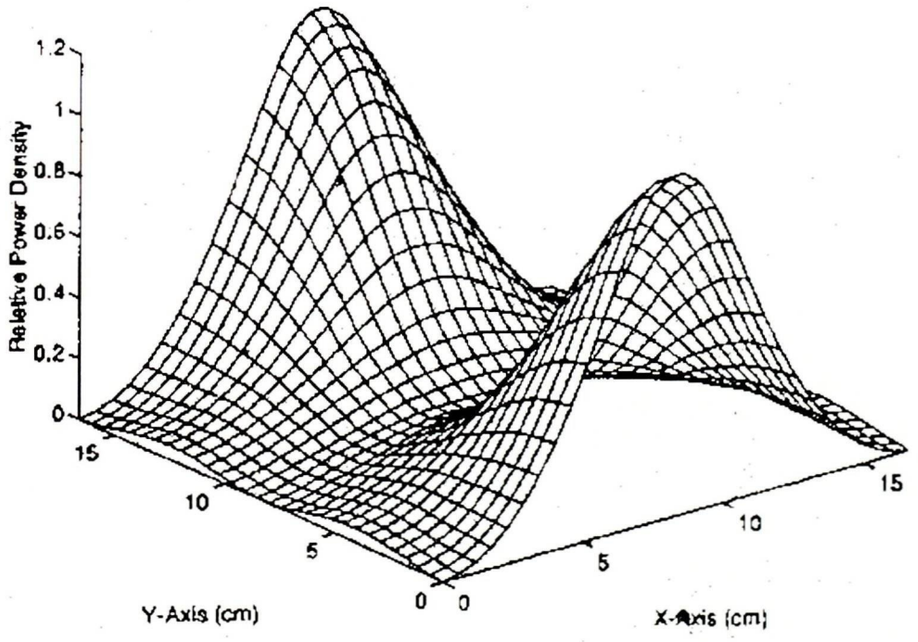

Figure 7.2.3: Power distribution for $z_0 = 23\delta$ - Liu et al.[2]

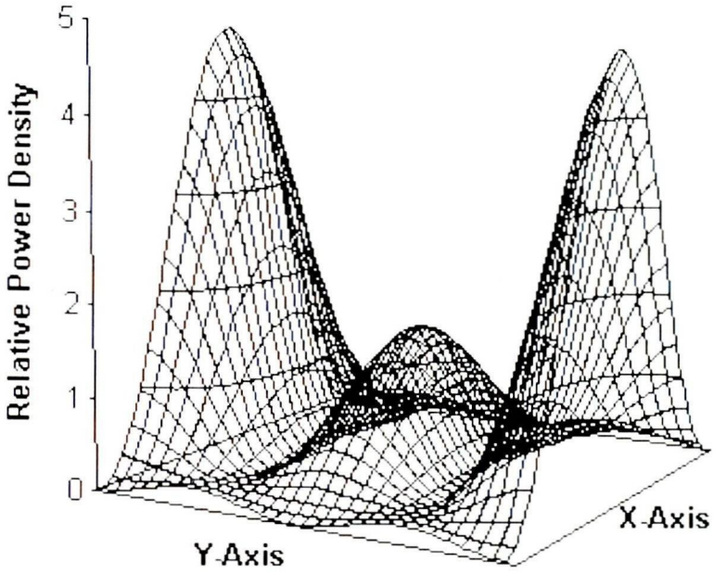

Figure 7.2.4: Power distribution for $z_0 = 18\delta$ - this work

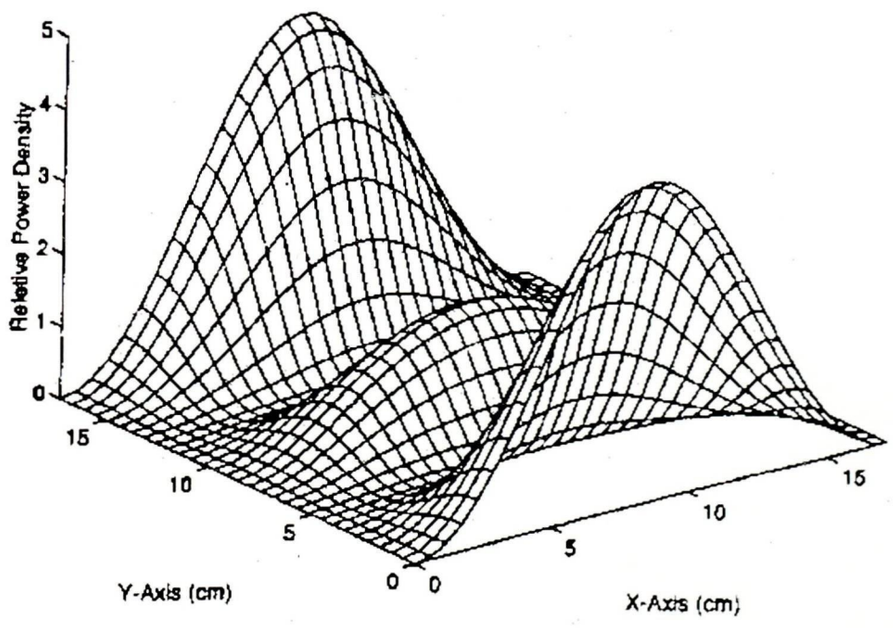

Figure 7.2.5: Power distribution for $z_0 = 18\delta$ - Bialkowski and Shahan[3]

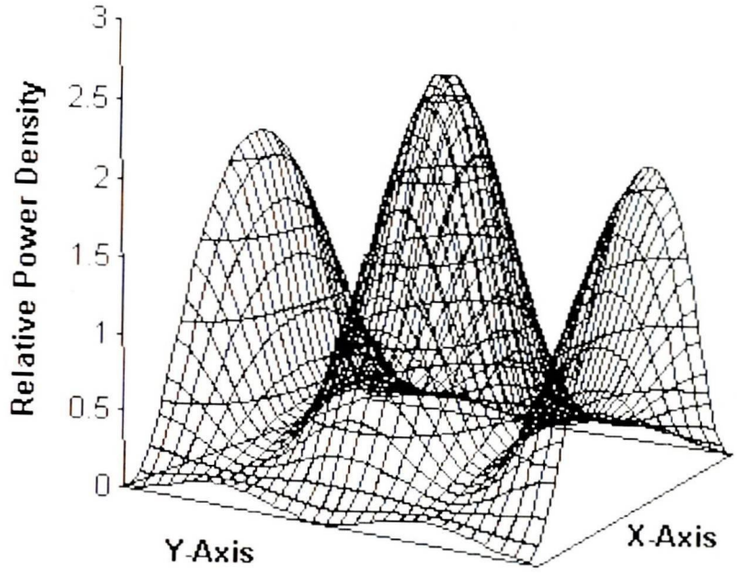

Figure 7.2.6: Power distribution for $z_0 = 13\delta$ - this work

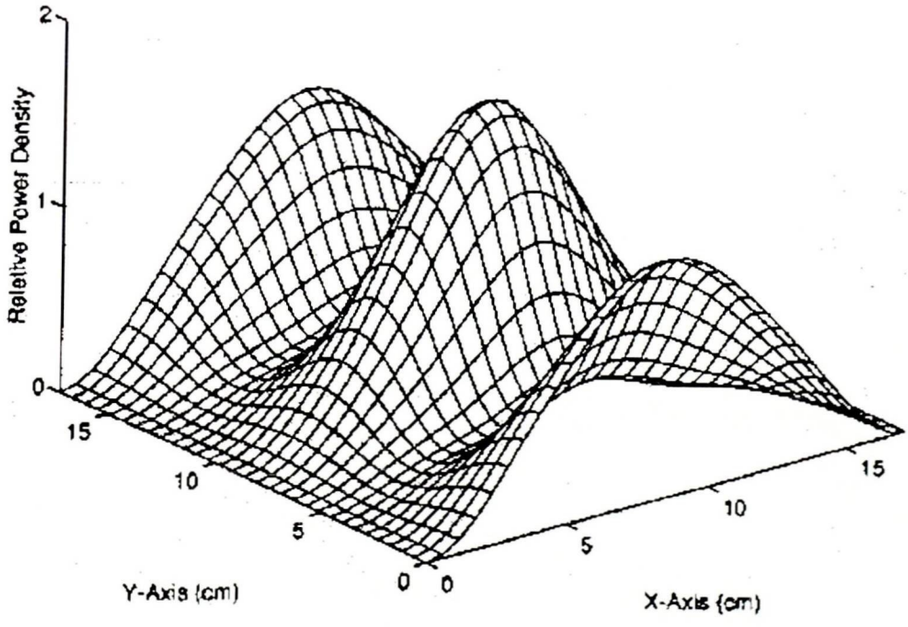

Figure 7.2.7: Power distribution for $z_0 = 13\delta$ - Bialkowski and Shahan[3]

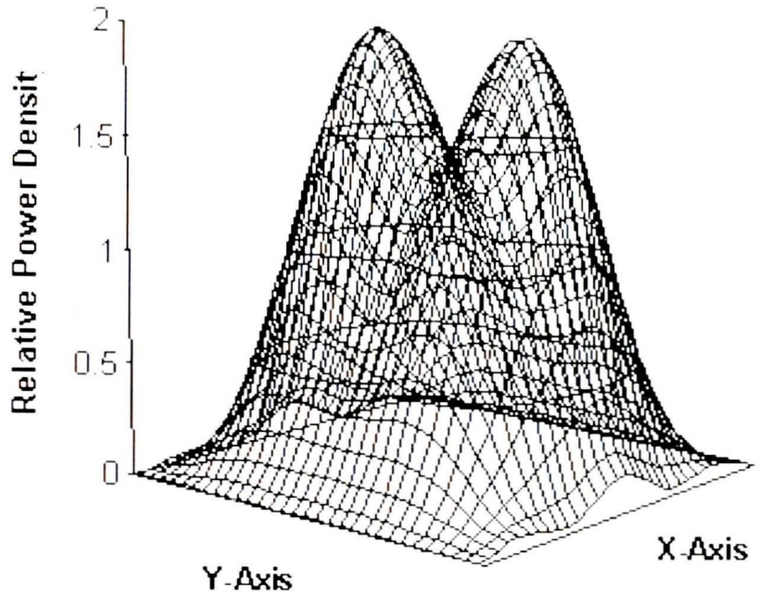

Figure 7.2.8: Power distribution for $z_0 = 8\delta$ - this work

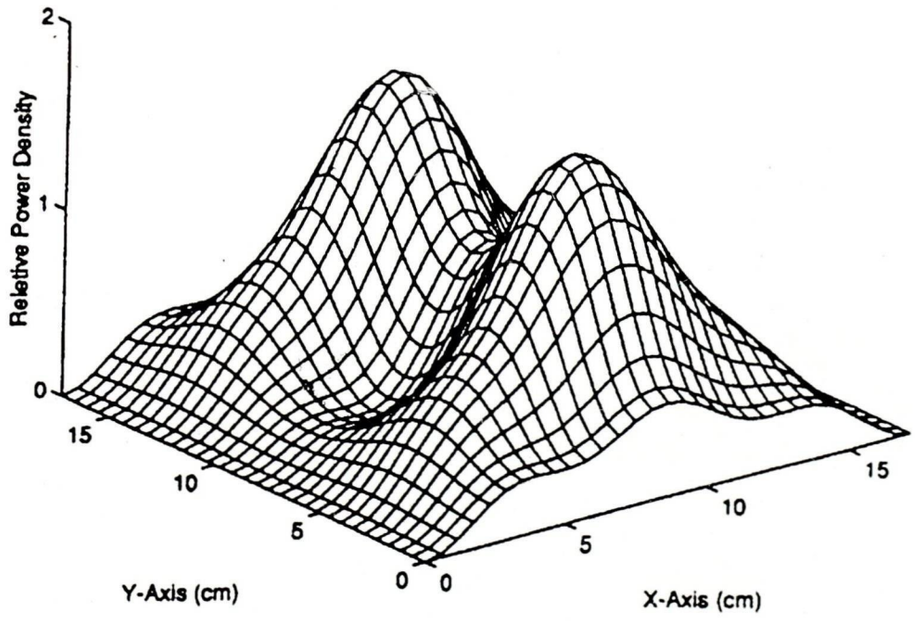

Figure 7.2.9: Power distribution for $z_0 = 8\delta$ - Bialkowski and Shahan[3]

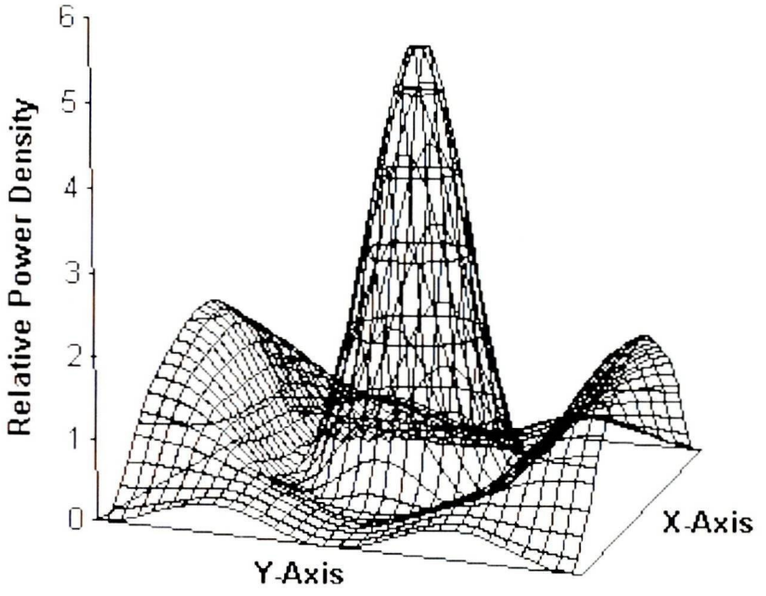

Figure 7.2.10: Power distribution for $z_0 = 3\delta$ - this work

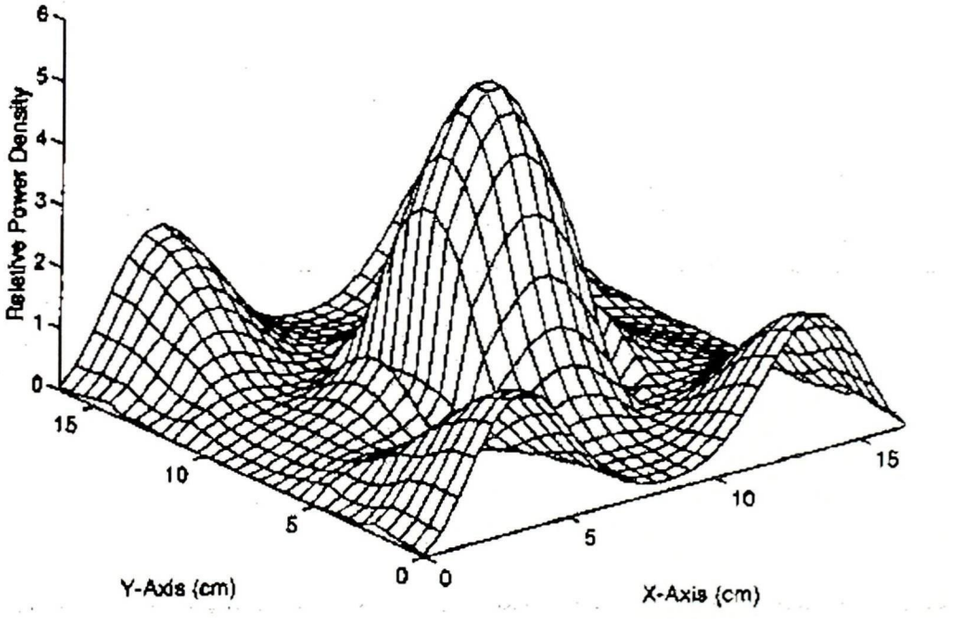

Figure 7.2.11: Power distribution for $z_0 = 3\delta$ - Liu et al.[2]

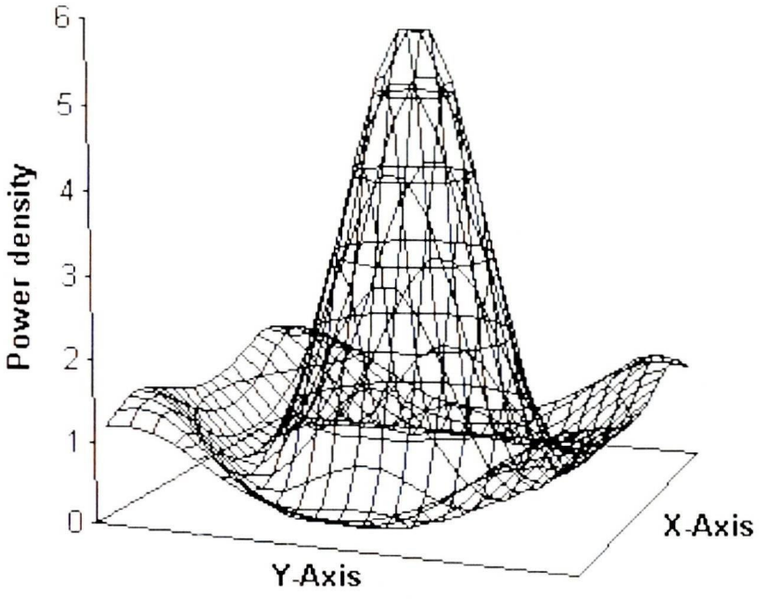

Figure 7.2.12: Power distribution for $z_0 = 3\delta$ for centrally located slab - this work

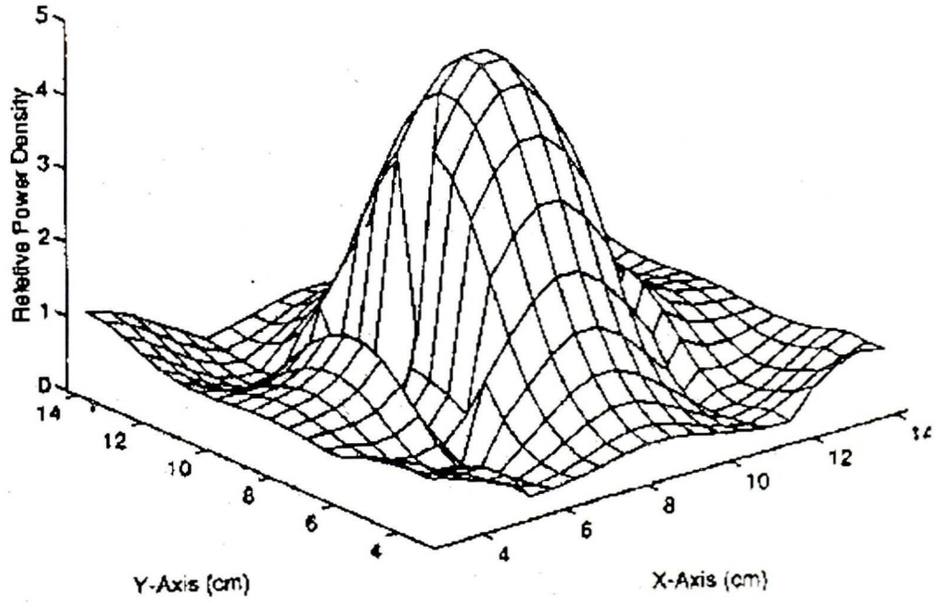

Figure 7.2.13: Power distribution for $z_0 = 3\delta$ for centrally located slab - Liu et al.[2]

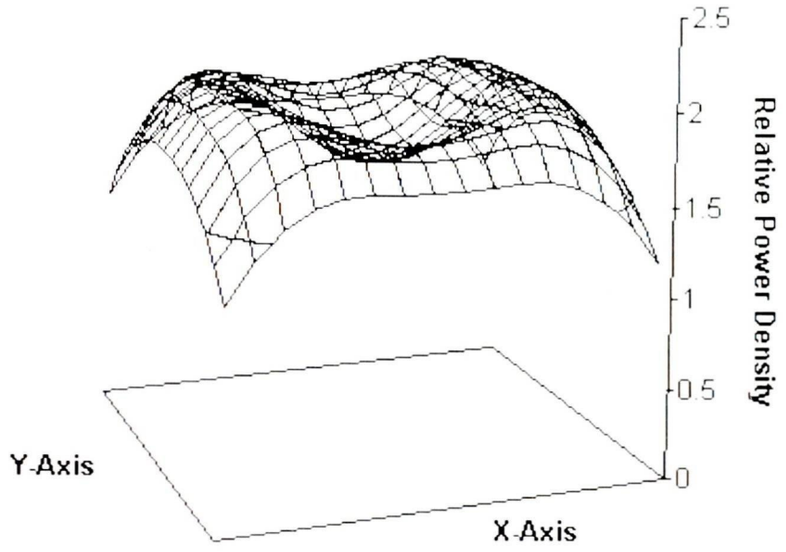

Figure 7.2.14: Power distribution for $z_0 = 8\delta$ for centrally located slab - this work

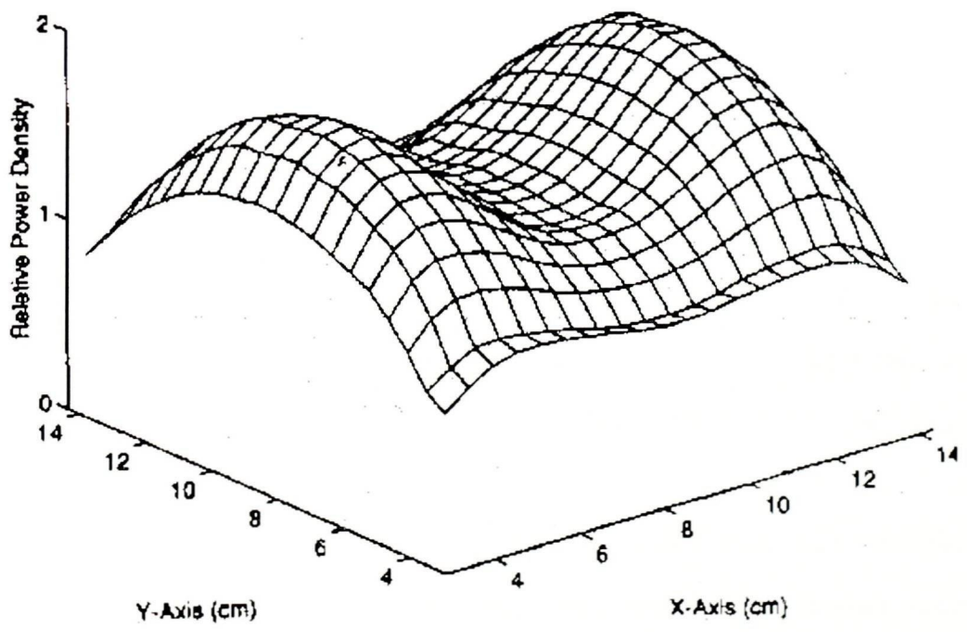

Figure 7.2.15: Power distribution for $z_0 = 8\delta$ for centrally located slab - Liu et al.[2]

T	12.3	25.0	34.7	39.95	45.5	48.0
ϵ'_r	52	43	36	36	28.4	22.4
ϵ''_{eff}	20	14.5	11.5	11.3	7.2	7.0

Table 7.7: Temperature dependence of the dielectric properties

§7.3 Coupled electro-thermal model

In this section a combined 3-D FD-TD and FV model for the electromagnetic and heat transfer process is presented. The properties are assumed to be temperature dependent only. The model is validated by comparison to experimental and numerical models based only on the FD-TD scheme[4].

The load was chosen to be a "phantom gel" and it was placed inside a container to maintain shape. It has a rectangular cross section. Energy is supplied to the cavity by a rectangular waveguide excited at a dominant TE_{10} mode. The power dissipated in the experiment was estimated to be approximately $600\,W$ and consequently the applied excitation amplitude was evaluated from the temperature rise to closely apply to the experiment.

The temperature dependence of the dielectric properties was measured[4]and is shown in Table 7.7.

Other gel parameters used are: specific heat $C_p = 3600\,Jkg^{-1}K^{-1}$, density $\rho = 1000\,kgm^{-3}$ and thermal conductivity $k = 0.55\,JK^{-1}m^{-1}s^{-1}$. The initial temperature of the load was $T_{init} = 5^oC$ and ambient temperature chosen was $T_{amb} = 30^oC$.

The dimensions of the oven are $321\,mm \times 271\,mm \times 390\,mm$. A non-uniform mesh consisting of $88 \times 68 \times 92$ cells is applied. The mesh sizes in each direction are shown in Tables 7.8, 7.9 and 7.10. The gel occupies a cuboid from nodes 13-56 in the x direction, 19-46 in the y direction and 25-70 in the z direction and is placed symmetrically with respect to the waveguide feed.

Unit cell	size(mm)
$1-4$	12
$5-6$	10
$7-8$	6
$9-22$	3.5
$23-46$	3.375
$47-60$	3.5
$61-62$	5.5
$63-68$	8.5

Table 7.8: Unit cells in the x direction

Unite cell	size(mm)
$1-10$	10.25
$11-12$	7.5
$13-14$	5
$15-24$	3.5
$25-40$	3.75
$41-50$	3.5
$51-52$	6.75

Table 7.9: Unit cells in the y direction

Unit cell	size(mm)
$1-4$	7
$5-8$	3
$9-10$	3
$11-12$	5
$13-16$	8
$17-18$	7.5
$19-20$	5
$21-42$	3.5
$43-52$	3.4
$53-74$	3.5
$75-76$	5
$77-78$	7.5
$79-84$	10

Table 7.10: Unit cells in the z direction

The program was run for a period of 180 seconds and temperature was measured across the horizontal and vertical planes of symmetry. The calculated power distribution in the horizontal plane of symmetry is shown in Figure 7.3.1. It is almost identical to the one that was obtained by Ma et al[4]. The calculated temperature after 180 seconds in the horizontal and vertical plane of symmetry are shown in Figures 7.3.4 and 7.3.6, respectively. They are compared to the results obtained by Ma et al.[4] (Figures 7.3.3 and 7.3.7) and experimentally measured distributions [4] (Figures 7.3.5 and 7.3.8).

It can be seen that in both planes the agreement is very good. However, there is a displacement in measured temperatures in Figures 7.3.5 and 7.3.8 due to the fact that the biomaterial was placed in a container. The main patterns of the temperature distribution have been successfully predicted. In particular the hot spots along the centre of the front face of the load and at the corners. Because the oven is asymmetric, the position of the hot spot on the face is not in the centre of the load (plane $z = 0$), even though the dielectric material was placed symmetrically with respect to the waveguide feed. In the vertical plane of symmetry (Figure 7.3.6), most of the heating takes place at the bottom right corner of the workload. The temperature in this region is very high compared to the temperatures in the centre.

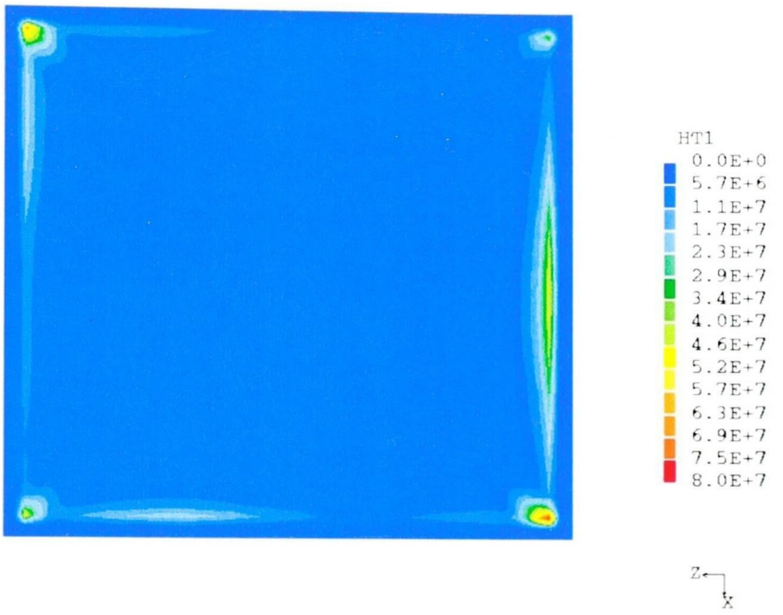

Figure 7.3.1: Calculated power distribution, $Q(Wm^{-3})$, in the horizontal symmetry plane after 180 seconds - this work

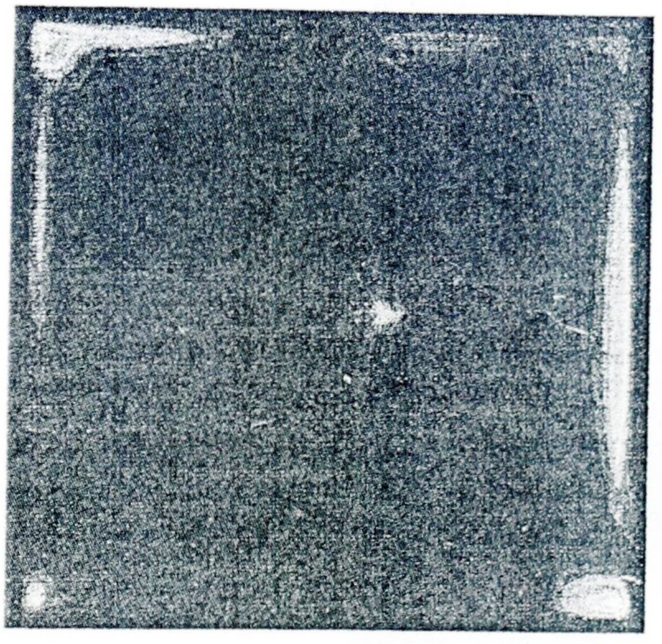

Figure 7.3.2: Calculated initial power distribution, $Q(Wm^{-3})$, in the horizontal symmetry plane - Ma et al.[4]

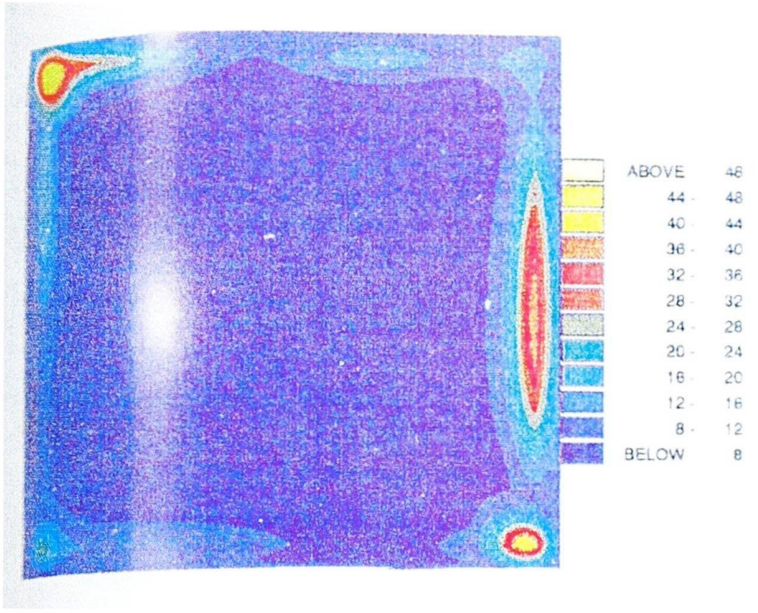

Figure 7.3.3: Calculated temperature distribution, $T(^oC)$, in the horizontal symmetry plane after 180 seconds - Ma et al.[4]

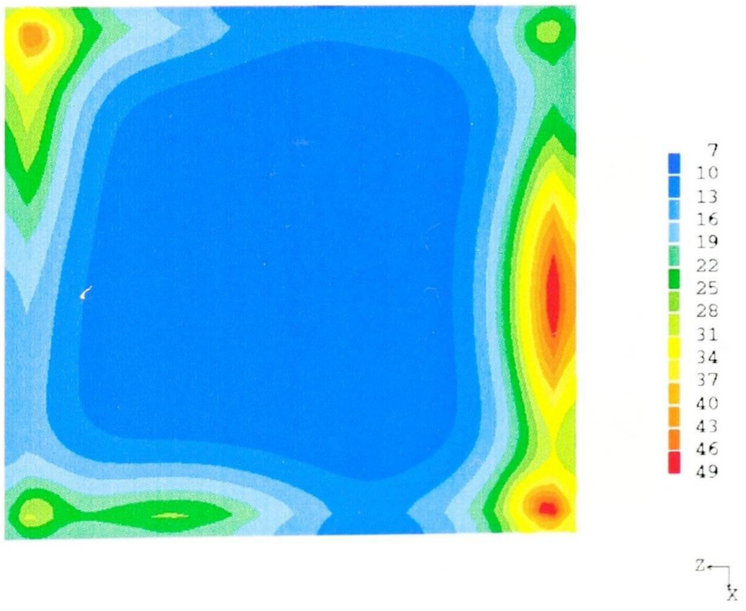

Figure 7.3.4: Calculated temperature distribution, $T(^oC)$, in the horizontal symmetry plane after 180 seconds - this work

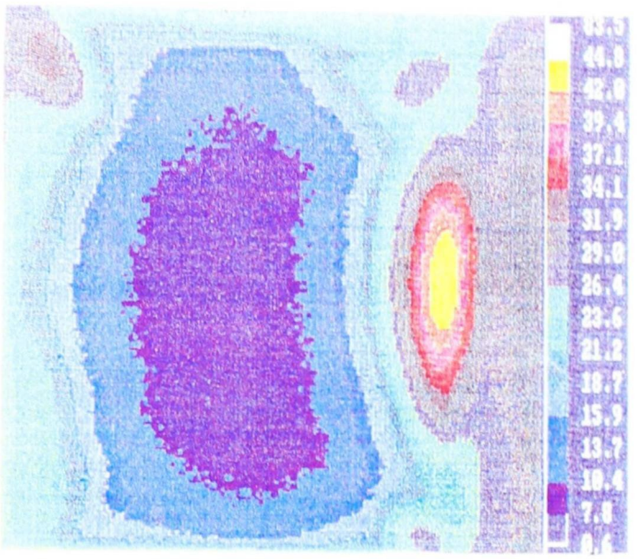

Figure 7.3.5: Measured temperature distribution, $T(^oC)$, in the horizontal plane after 180 seconds - experimental results[4]

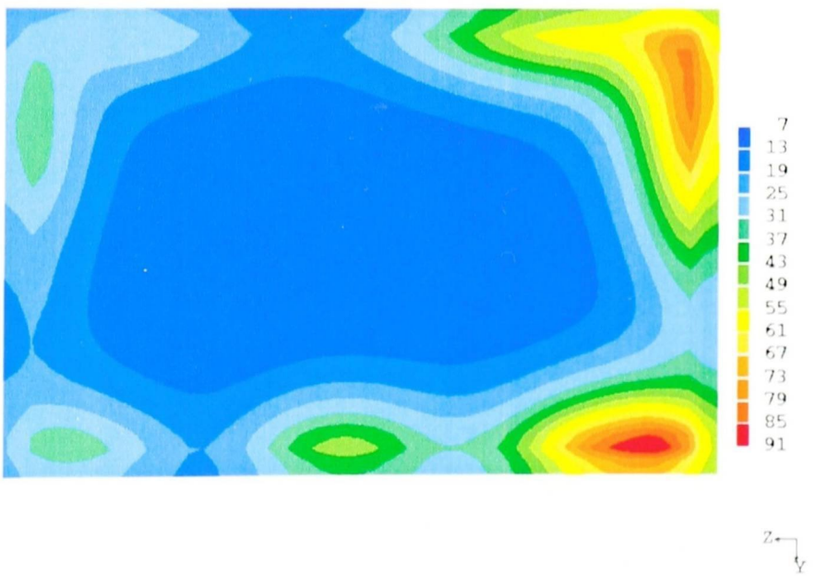

Figure 7.3.6: Calculated temperature distribution, $T(^oC)$, in the vertical symmetry plane after 180 seconds - this work

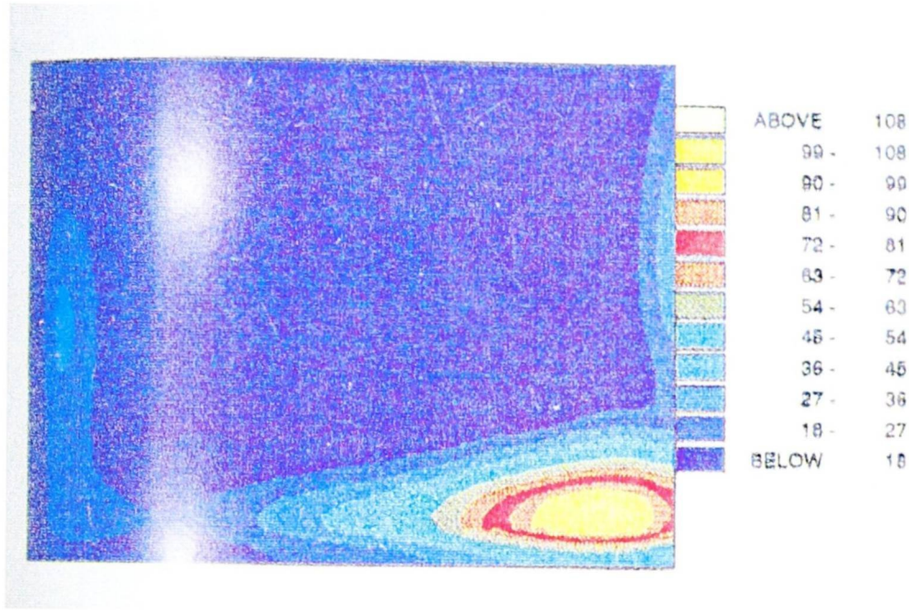

Figure 7.3.7: Calculated temperature distribution, $T(^oC)$, in the vertical symmetry plane after 180 seconds - Ma et al.[4]

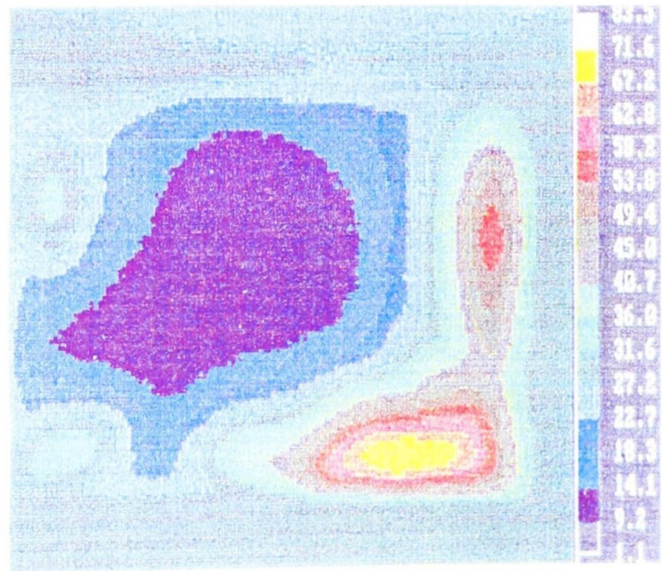

Figure 7.3.8: Measured temperature distribution, $T(^oC)$, in the vertical plane after 180 seconds - experimental results[4]

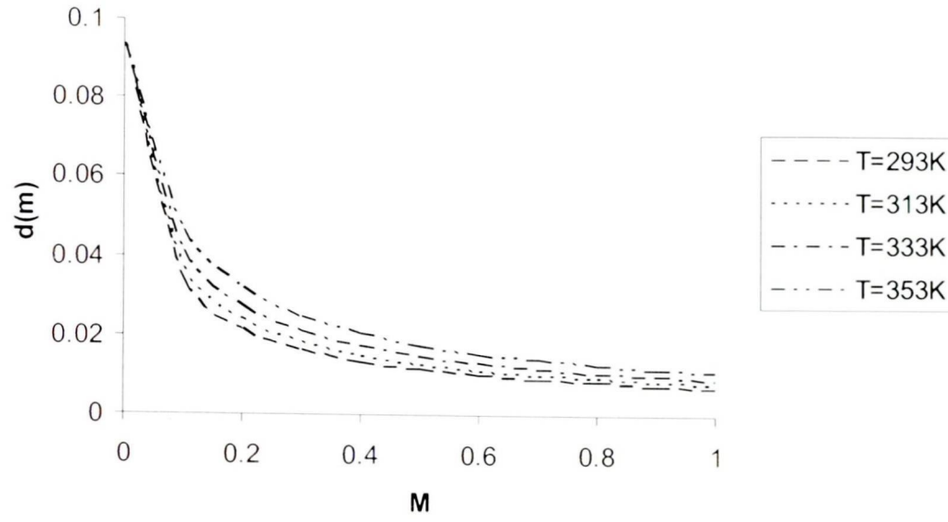

Figure 7.4.1: Penetration depth

§7.4 Coupled electro-thermal-mass transfer model

In order to produce a coupled electro-thermal-mass transfer model, the dielectric properties of the biomaterial have to be assumed to change both with temperature and moisture[27]. If the solid, liquid and gaseous phase temperature dependencies are known, then the porous medium relative permittivity and loss factor can be calculated using the following simple homogenization (see Section 4.2)

$$\overline{\epsilon}(M,T) = (1-\phi)\epsilon^{solid}(T) + \phi(M\epsilon^{liquid}(T) + (1-M)\epsilon^{gas}(T)) \,. \tag{7.4.1}$$

The dielectric permittivity and dielectric loss for dried solid were deduced from the permittivity of 80% moist reconstituted potato starch[14] on $T = 20°C$ using the equation 7.4.1. The temperature dependencies of water and gas were taken from the literature[1]. Using these expressions in (1.2.16) allows the penetration depth of this porous biomaterial to be calculated and its variation with moisture for a range of temperatures shown in Figure 7.4.1. The fluid movement through the porous medium is governed by the permeability for gas (k_g) and water (k_w). These are calculated using two different intrinsic permeabilities k_{gi} and k_{wi} (see Table 7.11) for gas and water that take into account structural changes occurring during the

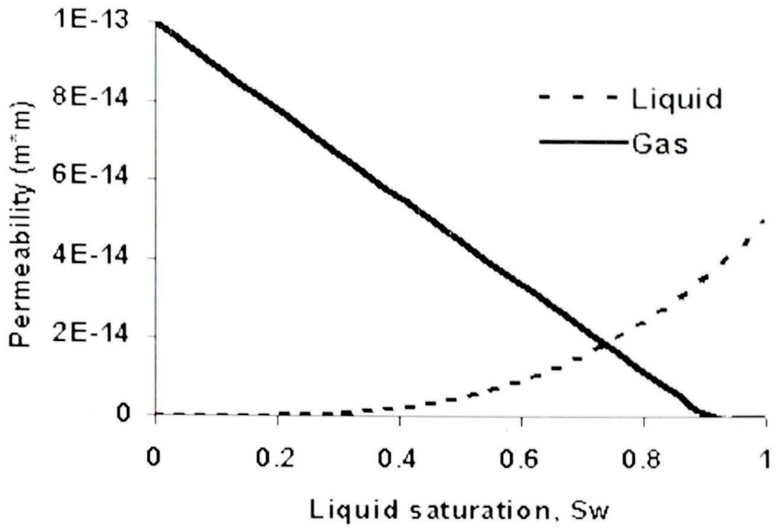

Figure 7.4.2: Relative permeabilities

microwave process[59], i.e.

$$k_g = k_{gl}k_{gr}, \quad k_w = k_{wl}k_{wr} \tag{7.4.2}$$

where the relative permeabilities k_{gr} and k_{wr} are used to interpolate between the dry and fully saturated end points (see e.g.[76]):

$$\begin{aligned} k_{gr} &= 1 - 1.1M \qquad M < 1/1.1, \\ k_{gr} &= 0 \qquad\qquad M > 1/1.1, \\ k_{wr} &= (\frac{M - M_{ir}}{1 - M_{ir}})^3 \qquad M > M_{ir}, \\ k_{wr} &= 0 \qquad\qquad M < M_{ir}, \end{aligned}$$

where M_{ir} is the irreducible liquid saturation[76]. Above two equations are shown graphically in Figure 7.4.2, using the values given in Table 7.11.

Computational results for the problem geometry shown in Section 7.2 and material properties described in the this sections are shown in Figures 7.4.3 to 7.4.24. Two slab positions are observed: away from the cavity-waveguide junction on the bottom (Figures 7.4.3 - 7.4.10) and close to the cavity - waveguide junction (Figures 7.4.19 - 7.4.24). This problem definition was chosen to highlight the fundamental physical mechanisms involved in the microwave processing of porous bio-materials and is not intended to reflect commercial applications. The software is however, sufficiently flexible to include features such as packaging when appropriate.

The results for the first case are presented as cross sections of the heated biomaterial showing the important physical variables - temperature, gas pressure, heat source Q, and liquid saturation - at t=20 seconds and t=150 seconds, and temperature histories at sample points in the interior and close to the top surface. The cross sections are in the y, z-plane so that the excitation waveguide is on top (see Figure 7.2.1) and are sampled approximately midway through the biomaterial. Since the biomaterial is not packaged moisture and heat can escape from all surfaces. The main physical effects visible in these plots are the expected material dry-out, accompanied by the expected increase in the penetration of the microwaves into the biomaterial. The mathematical model allows for evaporation (i.e. mass transfer between the liquid and gas phase) to take place within the porous material at all temperatures below the boiling point; the evaporation rate will be dependant on the surface area of the liquid phase which is in turn dependant on the porous structure. This parameter has been set to provide fairly rapid evaporation in this case but would need to be matched to experimental measurements in a commercial application. The temperature profiles are consistent with those used in the earlier validation study presented in Section 7.3. The same localised heating on the edges of the material (due to the local singularities at corners and edges of a lossy rectangular dielectric) and poor heating of the interior due to the low thermal conductivity of the gel is observed. Their conductivity is similar to the one calculated by (4.4.4) for the dry state typical of the directly heated region so that dryout is partly responsible for the poor interior heating shown in Figure 7.4.8.

Figure 7.4.3: Heating function, $Q(Wm^{-3})$, inside the reconstituted potato starch at $t = 20$ seconds

The results also show pressure increases around the localised heating areas driving a flow of liquid away from these areas demonstrating the importance of coupling a fully multi-phase porous media flow dynamics to the microwave heating. Similar results are reported by Perré and Turner[36] for timber drying (with higher internal pressure increases due to the lower permeability of timber) and Ni et al.[59] in a one-dimensional model of a material with similar permeabilities who reported internal pressure buildups of a similar magnitude.

These results took around 2 hours to produce with around 24,000 electromagnetic grid cells and 4000 finite volumes on a Sun Ultra5, 400 MHz CPU processor. Fine grid computations (Figures 7.4.13-7.4.18) with 190,000 electromagnetic grid cells and 32,000 finite volumes showed relatively small changes to the original calculations. These coupled computations are clearly expensive take more than 30 hours on the same machine) but would run significantly faster on the latest Sun processors.

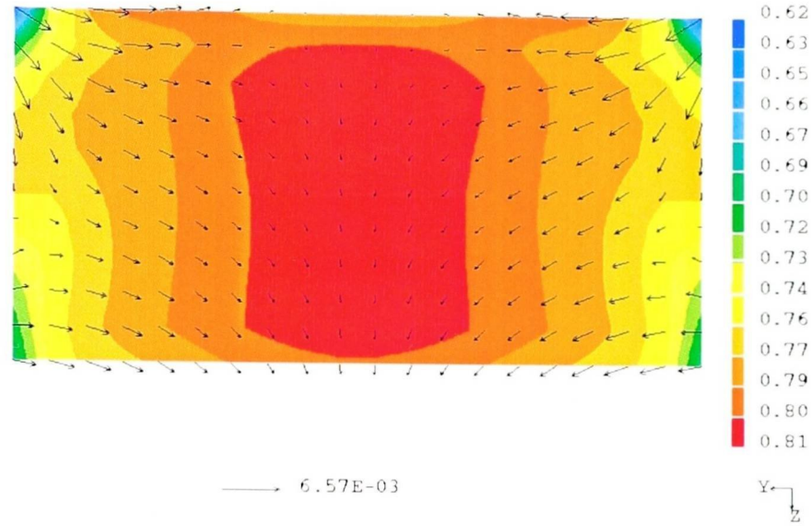

Figure 7.4.4: Liquid saturation, M, inside the reconstituted potato starch at $t = 20$ seconds

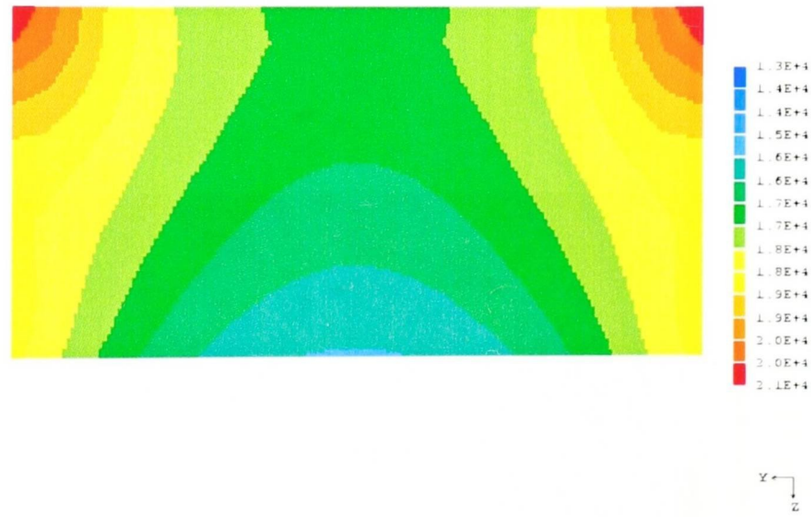

Figure 7.4.5: Dynamic Pressure profile, $p(Pa)$, inside the reconstituted potato starch at $t = 20$ seconds

The second set of results are for a slab having dimensions $200mm \times 200\,mm \times 4\,mm$ positioned such that the planes of the horizontal and vertical symmetry of the load coincided with those of the waveguide (Figures 7.4.19-7.4.24)[85]. The load was placed

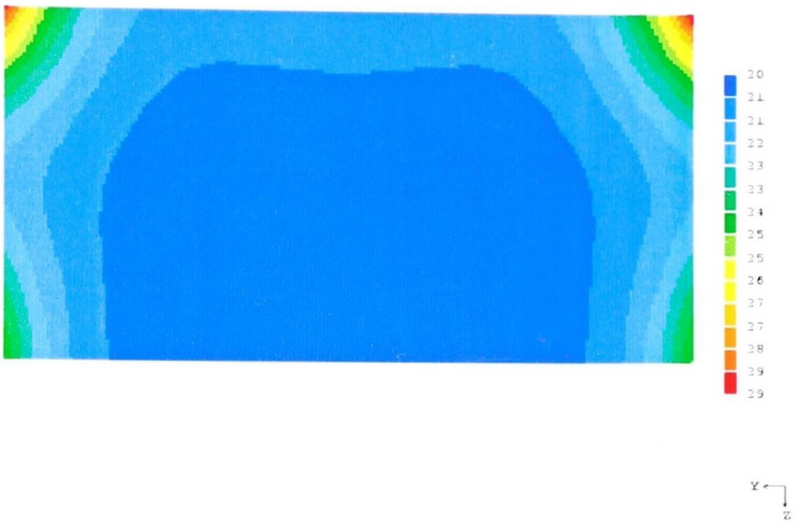

Figure 7.4.6: Liquid temperature profile, $T_l(^oC)$, inside the reconstituted potato starch at $t = 20$ seconds

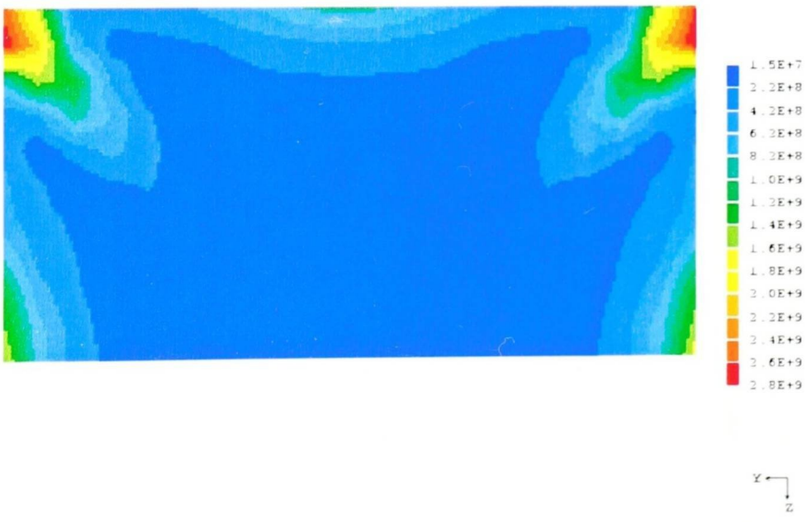

Figure 7.4.7: Heating function, $Q(Wm^{-3})$, inside the reconstituted potato starch at $t = 150$ seconds

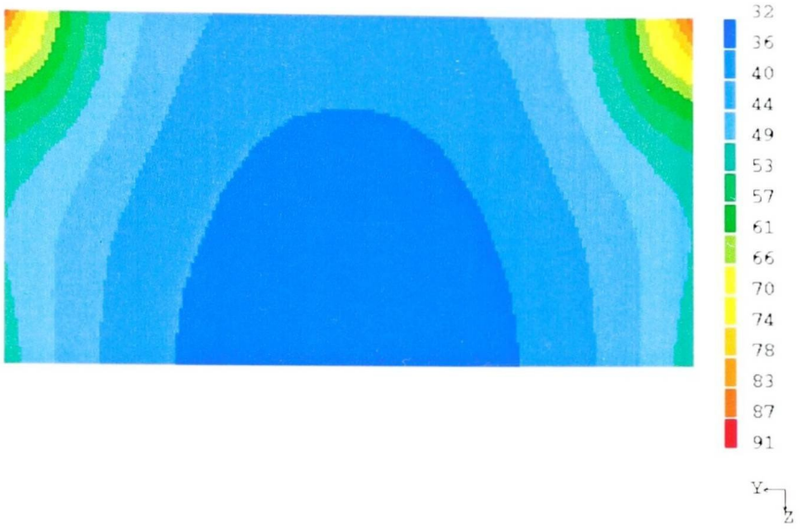

Figure 7.4.8: Liquid temperature profile, $T_l(^oC)$, inside the reconstituted potato starch at $t = 150$ seconds

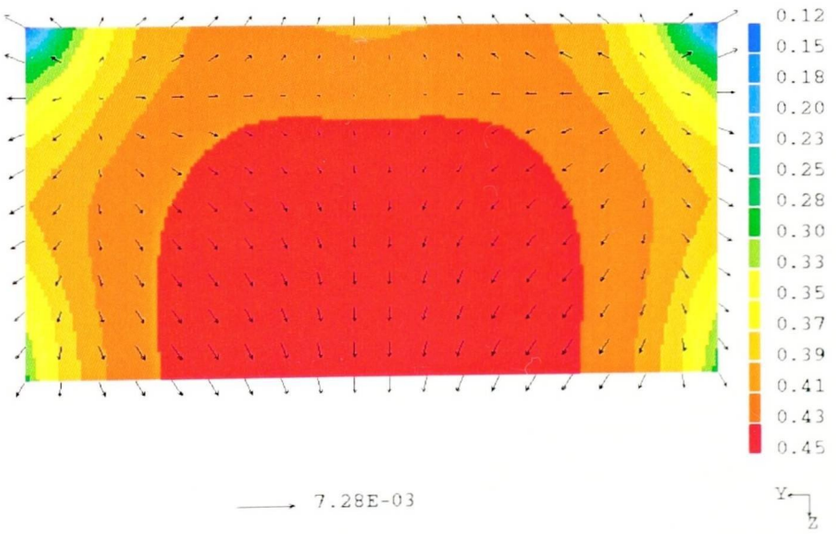

Figure 7.4.9: Liquid saturation, M, inside the reconstituted potato starch at $t = 150$ seconds

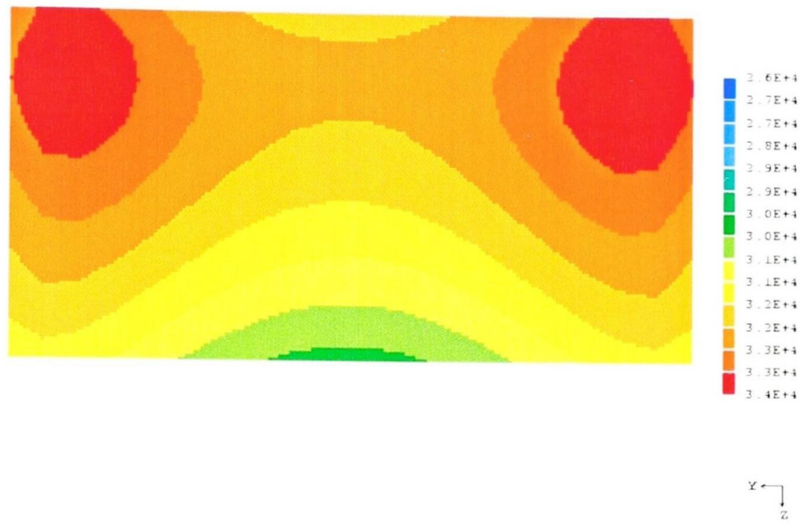

Figure 7.4.10: Dynamic Pressure profile, $p(Pa)$, inside the reconstituted potato starch at $t = 150$ seconds

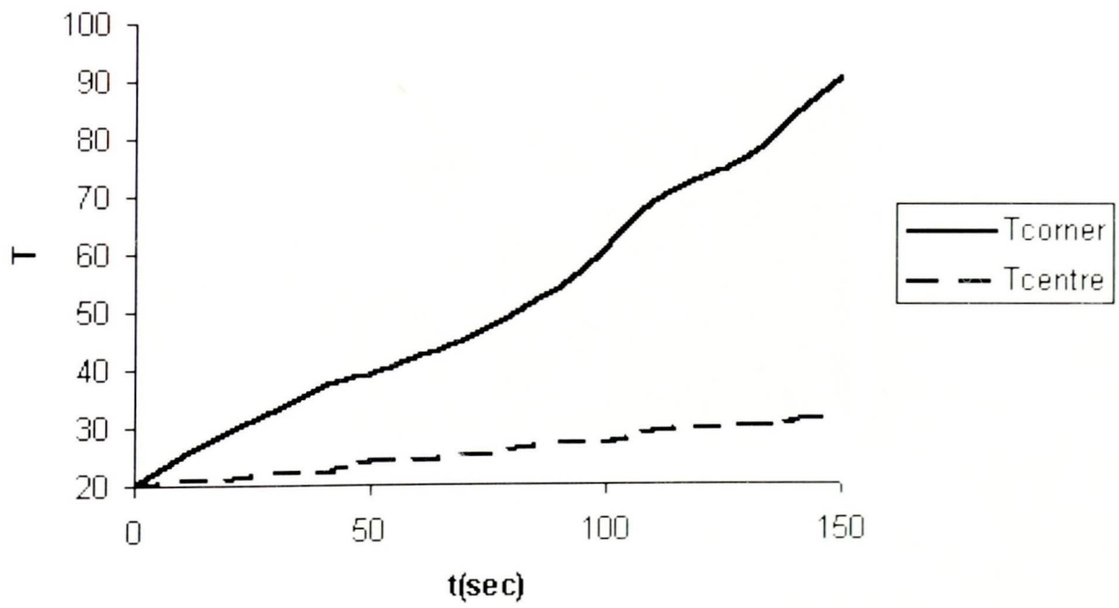

Figure 7.4.11: Temperature , $T(^oC)$, evolution over time at two different points in cross-section

Figure 7.4.12: Heating function, $Q(Wm^{-3})$, inside the reconstituted potato starch at $t = 20$ seconds - fine mesh

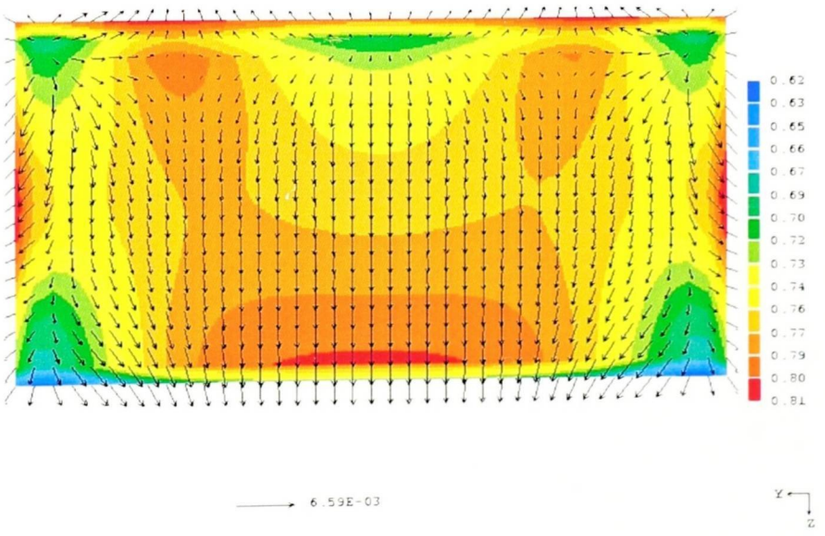

Figure 7.4.13: Liquid saturation, M, inside the reconstituted potato starch at $t = 20$ seconds - fine mesh

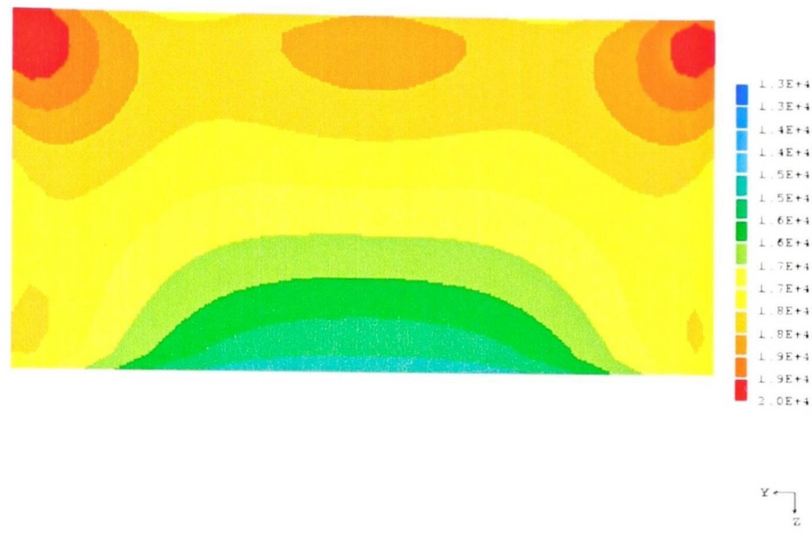

Figure 7.4.14: Dynamic Pressure profile, $p(Pa)$, inside the reconstituted potato starch at $t = 20$ seconds - fine mesh

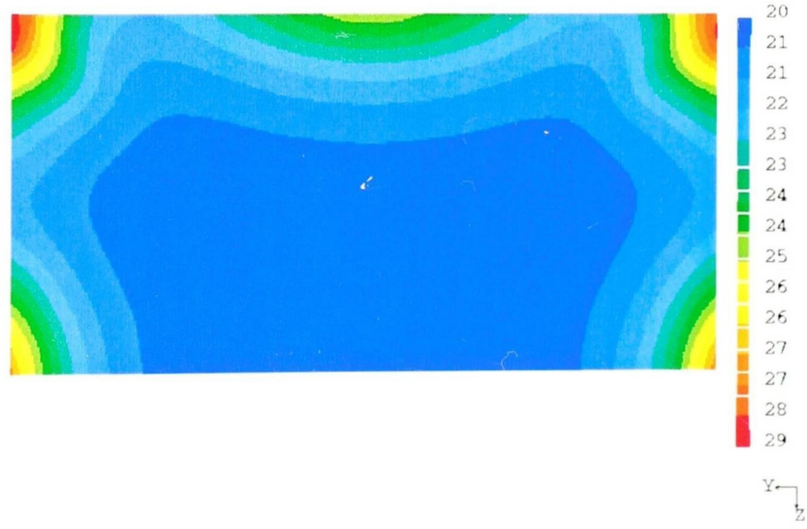

Figure 7.4.15: Liquid temperature profile, $T_l(^oC)$, inside the reconstituted potato starch at $t = 20$ seconds - fine mesh

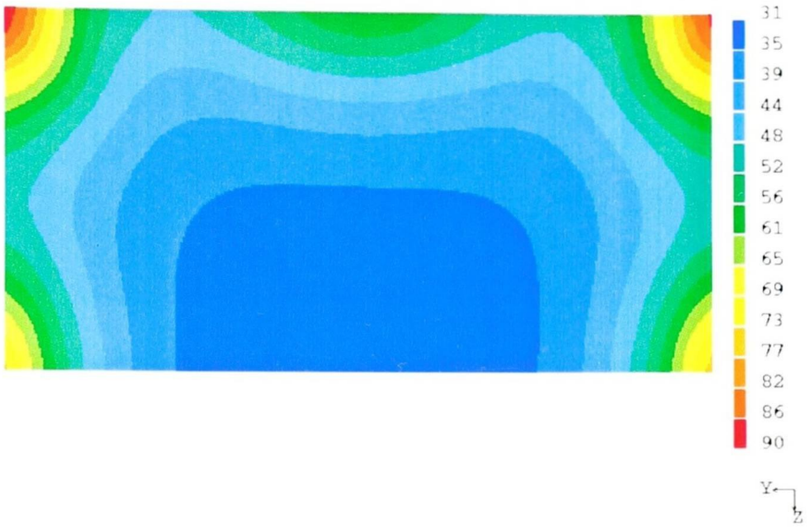

Figure 7.4.16: Liquid temperature profile, $T_l(^oC)$, inside the reconstituted potato starch at $t = 150$ seconds - fine mesh

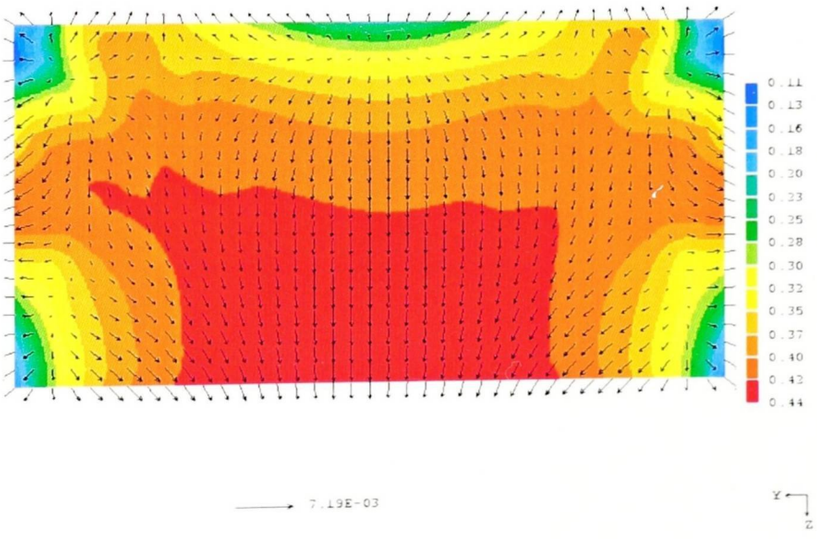

Figure 7.4.17: Liquid saturation, M, inside the reconstituted potato starch at $t = 150$ seconds - fine mesh

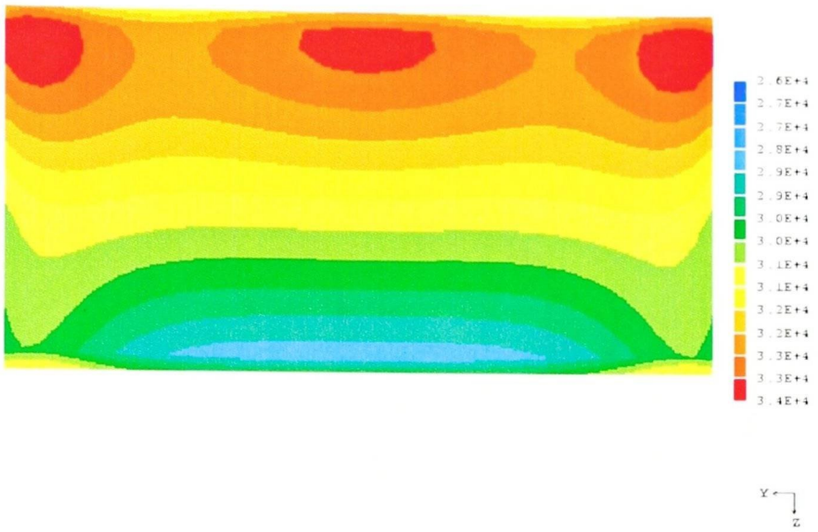

Figure 7.4.18: Dynamic Pressure profile, $p(Pa)$, inside the reconstituted potato starch at $t = 150$ seconds - fine mesh

at a distance of $17\,mm$ from the oven–waveguide junction. Due to the symmetry of the oven, the maximum values of the heating function in this case on the face are in the centre, Fig. 7.4.19. The calculated temperature distributions is shown in Fig. 7.4.22. Temperature increase will be very steep in the centre corresponding to the power distribution, slowing down towards the edges due to surface cooling. Due to the smaller thickness of the slab compared to the previous case and the fact that now the material gets heating from bellow as well, the temperature profiles are more uniform. It is easy to observe in this case the surface evaporation (Figures 7.4.23 and 7.4.24). It can be noted that hot spots at the corners disappear due to surface temperature boundary conditions (Figure 7.4.22). The microwave power distribution will change as shown in Fig. 7.4.20.

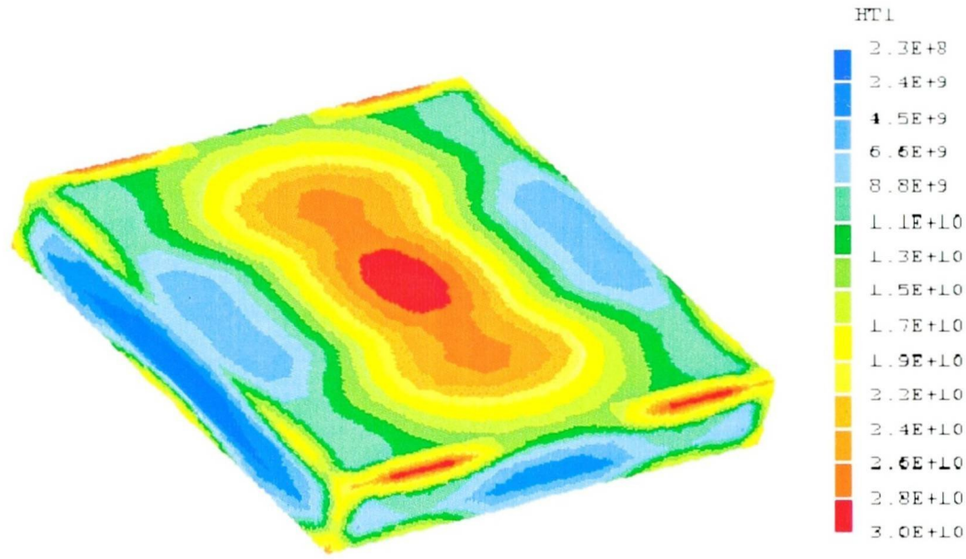

Figure 7.4.19: Heating function, $Q(Wm^{-3})$, inside the reconstituted potato starch at $t = 20$ seconds

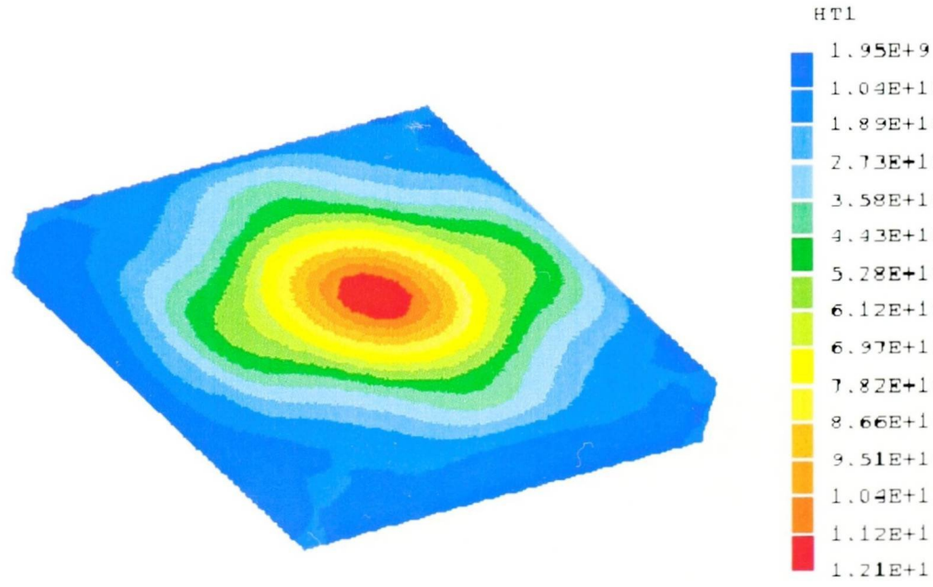

Figure 7.4.20: Heating function, $Q(Wm^{-3})$, inside the reconstituted potato starch at $t = 120$ seconds

Table 7.11: Input parameters used in the computations

Parameter	Value	Source
Porosity, ϕ	0.55	
Initial saturation, S_w	0.80	
Irreducible saturation, S_{ir}	0.08	(76)
Intrinsic gas permeability at very dry state, $k_{gi}(m^2)$	10×10^{-14}	(59)
Intrinsic liquid permeability at very wet state, $k_{wi}(m^2)$	5×10^{-14}	(59)
Initial temperature, $T_{init}(^\circ C)$	20	This work
Surrounding air temperature, $T_{init}(^\circ C)$	20	This work
Specific heat of gas, $c_{pg}(Jkg^{-1}K^{-1})$	1005	
Specific heat of water, $c_{pw}(Jkg^{-1}K^{-1})$	4180	
Specific heat of potato, $c_{ps}(Jkg^{-1}K^{-1})$	3500	
Gas density, $\rho_g(kgm^{-3})$	1.189	
Water density, $\rho_w(kgm^{-3})$	1000	
Potato density, $\rho_s(kgm^{-3})$	1050	
Dynamic viscosity of gas, $\mu_g(Pas)$	1.8×10^{-5}	
Dynamic viscosity of water, $\mu_w(Pas)$	5.468×10^{-4}	
Latent heat of vapourization, $L(Jkg^{-1})$	2.435×10^6	
Convective heat transfer coefficient, $h(Wm^{-2}K^{-1})$	10	(4)
Thermal conductivity of gas, $k_g(Wm^{-1}K^{-1})$	0.0258	
Thermal conductivity of water, $k_l(Wm^{-1}K^{-1})$	0.597	
Thermal conductivity of potato, $k_s(Wm^{-1}K^{-1})$	0.6	

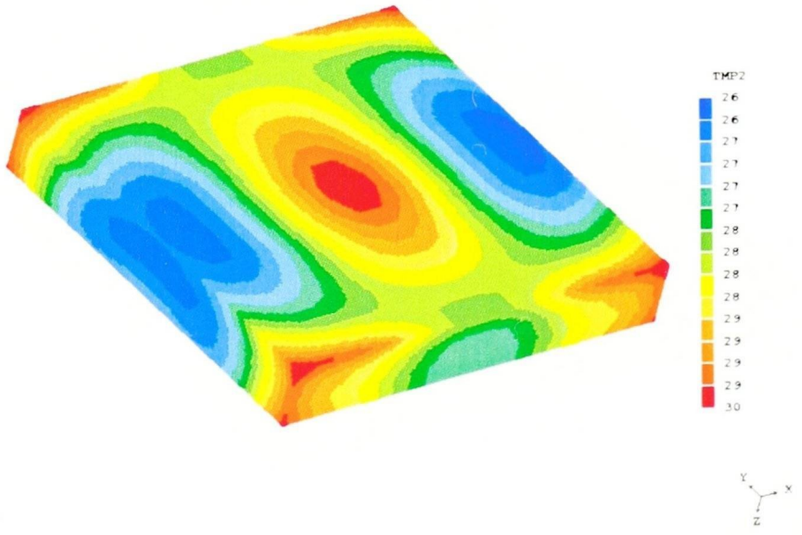

Figure 7.4.21: Temperature profile, $T(^oC)$, inside the reconstituted potato starch at $t = 20$ seconds

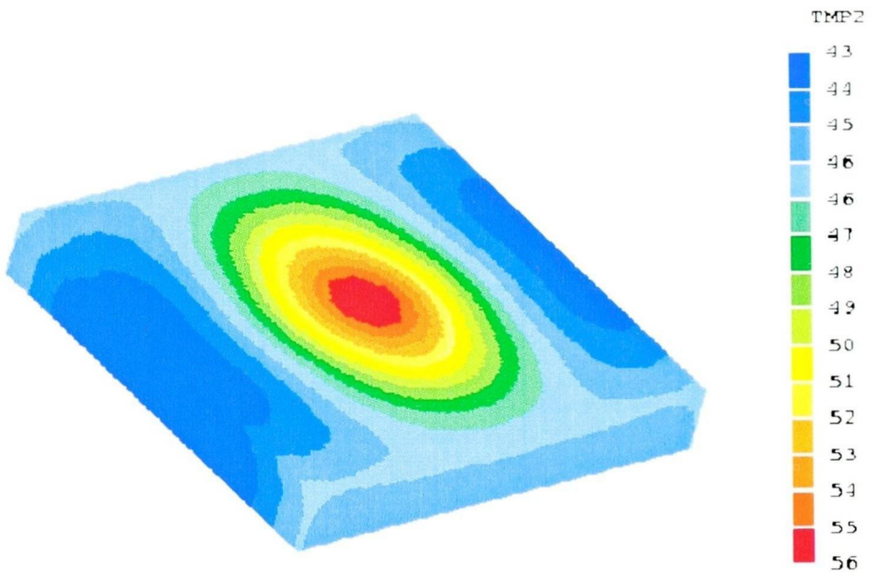

Figure 7.4.22: Temperature profile, $T(^oC)$, inside the reconstituted potato starch at $t = 120$ seconds

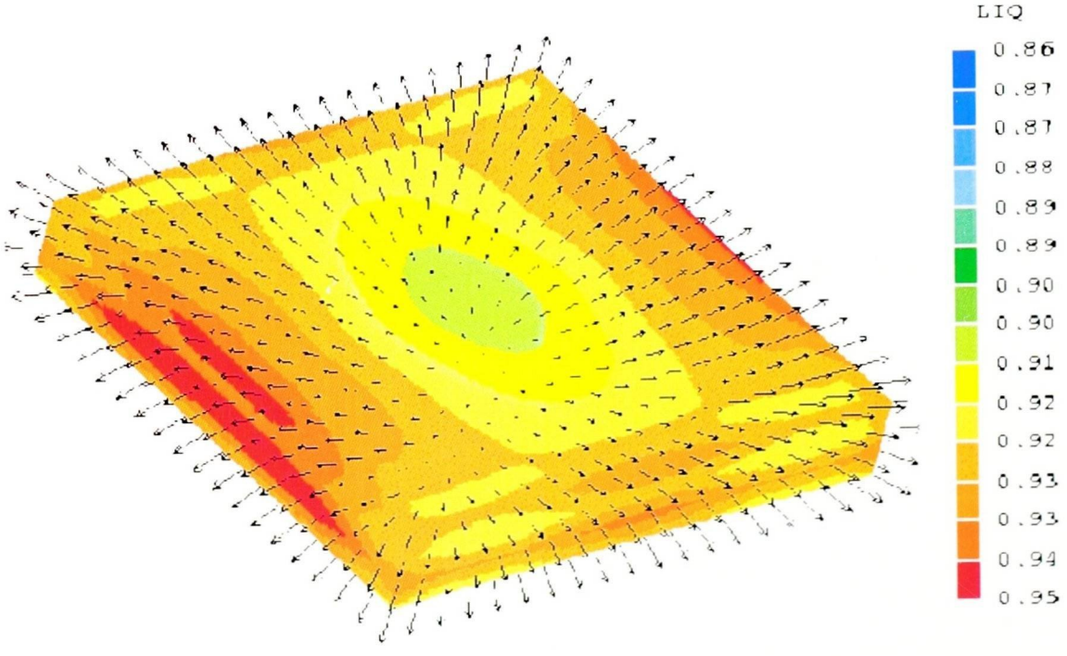

Figure 7.4.23: Liquid concentration, M, inside the reconstituted potato starch at $t = 40$ seconds

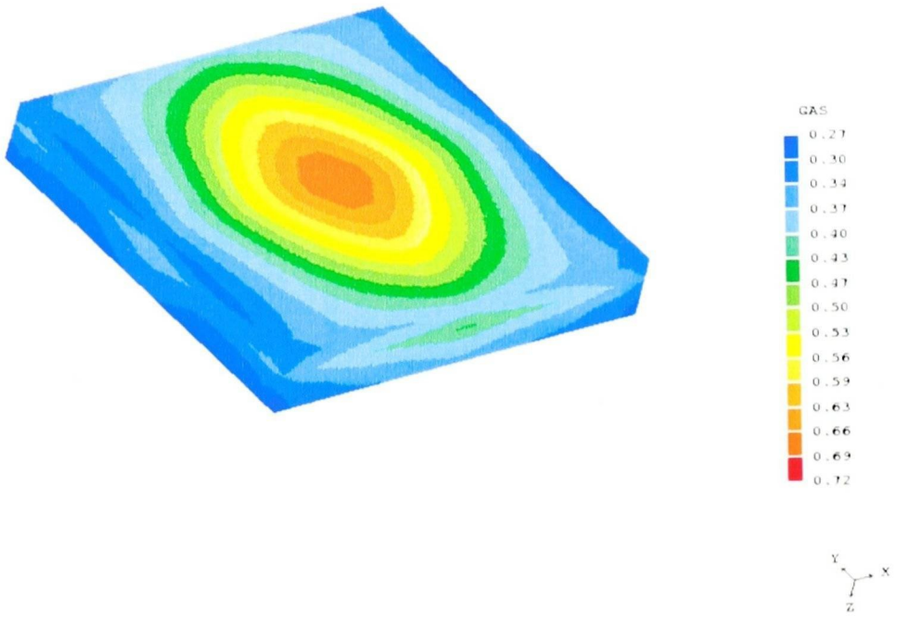

Figure 7.4.24: Gas concentration, $1 - M$, inside the reconstituted potato starch at $t = 120$ seconds

CHAPTER

EIGHT

Conclusion

A multi-phase transport flow model in a porous medium, which combines a three-dimensional heat and mass transfer code with a three-dimensional electromagnetic computational scheme, was able to predict the overall drying behaviour of a porous material in a microwave oven.

The FD-TD scheme was chosen for solving the electromagnetic field distribution. The scheme was described in detail, along with the implementation of the boundary conditions at dielectric interfaces. Its second order accuracy was proved by comparison of the numerical results to analytical solutions in unloaded 2-D and 3-D rectangular microwave cavities. Both uniform and nonuniform structured meshed were employed. The power distribution in loaded 2-D single- and multi-mode microwave cavities was validated. The influence of dielectric properties, sample size and location on resonant conditions was studied. Results for 3-D microwave power distribution in loaded microwave enclosures was compared to results from other numerical techniques found in the literature.

The flow model is a multi-phase one. The moisture transport in the porous food material is modelled with phase change. Local (pressure and temperature dependent) saturation conditions were applied at each computational cell interface and are able to model evaporation and re-condensation. The pressure field was calculated by means of the of a pressure correction equation based on the SIMPLE algorithm. The solution domain for the CFD calculations includes the food material only. The

surface boundary conditions deal with heat transfer by both forced convention and radiation as well as evaporation. A 1-D freeze-drying example was used for investigation of different aspects of drying. More comprehensive results were obtained using PHOENICS.

Full coupling between the two calculations is achieved by mapping the food dielectric properties from the CFD mesh onto the CEM mesh and then mapping the microwave heating function from the CEM mesh to the CFD mesh. In this way the two calculations have been closely coupled in an optimally cost-efficient manner.

Results of a coupled electro-thermal algorithm coded by the author were compared to results obtained with PHOENICS. A very good agreement was noticed. A similar 3-D algorithm for the temperature distribution in a biomaterial was validated against other numerical results and experimental measurements.

The fully coupled model accounts for the pressure driven fluid flow and change of phase in wet bio-materials. Drying occurs due to liquid movement which does not occur during more conventional drying processes. The characteristics of heat and mass transfer are greatly influenced by internal heat generation. With the internal heat generation, most of the moisture is vaporized before leaving the sample. Agreement was achieved between calculated values for the penetration depth and the distribution of the heating function inside the sample as dielectric properties change. The results were also compared to those of simpler problems available in the literature.

The inadequacies of the model are mainly due to rectangular meshes which can not always approximate real shapes well enough. Local subgridding techniques could be employed to handle more complex geometries.

Future work could also incorporate two important practical features of domestic microwave processing - the use of rotation (as opposed to mode stirring) and active packaging. This is particularly important when thawing foods from frozen.

Since the electromagnetic relaxation timescale is of the order of picoseconds, the rotation could be treated as a sequence of fixed positions. The fully-coupled algorithm makes use of two independent meshes with a general mapping function; this permits physical rotation to be implemented entirely within the mapping procedures. The CFD mesh would rotate with the food while the spatial distribution of the heating function changes. The CEM mesh does not rotate but dielectric material properties would now be re-mapped from the new CFD mesh position. CEM mesh sub-structuring would ensure the new food boundary position is well approximated.

Packaging has a direct effect on heating and moisture transport. Edge over-heating is avoided to some extent with curved packaging. The heating effect could also be modified by including metallised plastic susceptors or foil shielding inside the packaging. The use of susceptors (characterized in terms of surface resistivities) is of interest for microwave cooking from a frozen state. Susceptors are effectively sub-grid scale features (of the order of millimeter in thickness) however they can be approximated reasonably well if the CEM computational grid is aligned with the layer. The FD-TD scheme would then define tangential electric field components and normal magnetic fields on the layer. The method is readily modified so that these specific degrees of freedom are computed using surface resistivities from the integral form of Maxwell's equations.

In this study, temperatures between the room temperature and the boiling point have been considered. Another possible research direction can be the processing of frozen food in which gross changes in dielectric properties occur as a result of phase change and where mushy zones may develop.

References

[1] A. C. Metaxas and R. J. Meredith, *Industrial Microwave Heating*. Peter Peregrinus Ltd., London (1983).

[2] F. Liu, I. Turner and M. Bialkowski, 'A Finite–Difference Time–Domain Simulation of Power Density Distribution in a Dielectric Loaded Microwave Cavity', *Journal of Microwave Power and Electromagnetic Energy*, **29(3)**, 138–148 (1994).

[3] M. E. Bialkowski and O.Shahan, 'Analysis of a waveguide-disk load', *IEEE MTT-S Symposium. Dallas*, 375–378 (1990).

[4] L. Ma, D.-L. Paul, N. Pothecary, C. Railton, J. Bows, L. Barratt and J. M. abd D. Simons, 'Experimental Validation of a Combined Electromagnetic and Thermal FTDT Model of a Microwave Heating Process', *IEEE Transactions on Microwave Theory and Techniques*, **43(11)**, 2565–2572 (1995).

[5] G. A. Kriegsmann, 'Thermal Runaway in Microwave Heated Ceramics: A One-Dimensional Model', *J.Appl.Phys*, **71(1)**, 1960–1966 (1992).

[6] D. W. Lyons, J. D. Hatcher and J. E. Sunderland, 'Drying of a Porous Medium with Internal Heat Generation', *International Journal of Heat and Mass Transfer*, **15**, 897–905 (1972).

[7] M. R. Booty and G. A. Kriegsmann, 'Microwave Heating and Joining of Ceramic Cylinders: A Mathematical Model', *Methods and Applications of Analysis*, **1(4)**, 403–414 (1994).

[8] A. G. Whittaker and D. M. P. Mingos, 'The Application of Microwave Heating to Chemical Syntheses', *Journal of Microwave Power and Electromagnetic Energy*, **29(4)**, 195–219 (1994).

[9] G. A. Kriegsmann, 'Hot Spots Formation in Microwave Heated Ceramic Fibers', *J. Appl.Math* (1997).

[10] M. Subirats, M. F. Iskander, M. J. White and J. J. O. Kiggans, 'FTDT Simulation of Microwave Sintering in Large (500/4000 liter)Multimode Cavities', *Journal of Microwave Power and Electromagnetic Energy*, **32(3)**, 161–169 (1997).

[11] A. Breccia, B. Esposito, G. B. Fratadocchi and A. Fini, 'Reaction Between Methanol and Commercial Seed Oils Under Microwave Radiation', *Journal of Microwave Power and Electromagnetic Energy*, **34(1)**, 3–21 (1969).

[12] G. Saltiel and A. K. Datta, 'Heat and Mass Transfer in Microwave Processing', *Advances in Heat Transfer*, **33**, 1–94 (1999).

[13] D. Sullivan, 'A Frequency-Dependent FTDT Method for Biological Applications', *IEEE Transactions on Microwave Theory and Techniques*, **40(3)**, 532–539 (1992).

[14] N. Bengtsson and T. Ohlsson, 'Microwave Heating in the Food Industry', *Proceedings of the IEEE*, **62(1)**, 44–54 (1974).

[15] A. H. Barrett, A. V. Cardello, A. Prakash, L. Mair, I. A. Taub and L. L. Lesher, 'Optimization of Dehydrated Egg Quality by Microwave Assisted Freeze–Drying and Hygrocolloid Incorporation', *Journal of Food Processing and Preservation*, **21**, 225–244 (1997).

[16] J. Sochanski, J. Goyette, T. Bose, C. Akyel and R. Bosisio, 'Freeze-Drying of Thin Plates by Microwaves', *Journal of Microwave Power and Electromagnetic Energy*, **26(2)**, 90–99 (1991).

[17] B. J. Pangrle, K. G. Ayappa, H. T. Davis, E. A. Davis and J. Gordon, 'Microwave Thawing of Cylinders', *AIChE Journal*, **37(12)**, 1789–1800 (1991).

[18] H. Zhao and I. Turner, 'The Use of a Coupled Computational Model for Studying the Microwave Heating of Wood ', *J. Appl.Math*, 1–18 (1999).

[19] T. Ohlsson, 'Temperature distribution in microwave oven heating– the influence of microwave feed system design', *Swedish Institute for Food Preservaation Researc: A Research Note*, 93–96 (1980).

[20] M. Chamchong and A. K. Datta, 'Thawing of Food in a Microwave Oven:II.Effect of Load Geometry and Dielectric Properties', *Journal of Microwave Power and Electromagnetic Energy*, **34(1)**, 22–31 (1999).

[21] A. K. Datta, 'Heat and mass transfer in the microwave processing of food', *Chemical Engineering Progress*, **86**, 47–53 (1990).

[22] J. R. Bows and P. S. Richardson, 'Effective of Component Configuration and Packaging materials on Microwave Reheating a Frozen Three-Componment Meal', *International Journal of Food Science and Technology*, **25**, 538–550 (1990).

[23] L. Zhou, 'Finite Element Modeling of Heat and Mass Transfer, and Related Nutrient Change and Microbial Activity During Microwave Heating of Food Materials ', *PhD Thesis. The Pennsylvania State University* (1993).

[24] K. G. Ayappa, H. T. Davis, G. Crapiste, E. A. Davis and J. Gordon, 'Microwave Heating: An Evaluation of Power Formulations', *Chemical Engineering Science*, **46**, 1005–1016 (1991).

[25] W. Fu and A. Metaxas, 'A Mathematical Derivation of Power Penetration Depth for Thin Lossy Materials', *Journal of Microwave Power and Electromagnetic Energy*, **27(4)**, 217–222 (1992).

[26] G. Summu, 'A Review on Microwave Baking of Foods', *International Journal of Food Science and Technology*, **36**, 117–127 (2001).

[27] D. D. Dincov, K. A. Parrott and K. A. Pericleous, 'A Numerical Algorithm for Heat and Mass Transfer in Microwave Processing of Moist Biomaterials', *International Journal of Numerical Methods for Heat and Fluid Flow (submitted)* (2002).

[28] D. D. Dincov, K. A. Parrott and K. A. Pericleous, 'Heat and Mass Transfer in Microwave Heating of Moist Biomaterials', 3^{rd} *International Symposium on Finite VOlumes for Complex Applications* (2002).

[29] 'PHOENICS code, CHAM ltd Wimbledon (http://www.cham.co.uk)' (2002).

[30] M. F. Iskander, 'Computer Modelling and Numerical Techniques for Quantifying Microwave Interactions with Materials', *Mat.Res.Soc.Symp.Proc.*, **189**, 149–171 (1991).

[31] M. Ishii, *Thermo-fluid dynamic theory of two-phase flow*. Eyrolles, Book Publication (1975).

[32] D. S. Chen, R. K. Singh, R. K. Haghighi and P. E. Nelson, 'Finite element analysis of temperature distribution in microwaved cylindrical potato tissues ', *Journal of Food Engineering*, **18**, 351–368 (1993).

[33] Y. E. Lin, R. C. Anantheswaran and V. M. Puri, 'Finite element analysis of solid foods ', *Journal of Food Engineering*, **25**, 85–112 (1995).

[34] D. A. Al-Mukhtar and J. E. Sitch, 'Transmission–line matrix method with irregularity graded space', *IEE Proceedings*, **128(6)**, 299–305 (1981).

[35] D. C. Dibben and A. C. Metaxas, 'Finite Element Time Domain Analysis of Multimode Applicators Using Edge Elements', *Journal of Microwave Power and Electromagnetic Energy*, **29(4)**, 242–252 (1994).

[36] P. Perré and I. W. Turner, 'An investigation of the combined microwave and convective drying of softwood in an oversized waveguide: a comparison between theoretical and experimental results ', *J. Appl.Math* (1999).

[37] K. S. Yee, 'Numerical solution of initial boundary values probelems involving Maxwell's equations in isotropic media', *IEEE Trans.Antennas Propag.*, **14** 302–307 (1996).

[38] A. Razek, 'Computational Electromagnetics for Microwave Heating', *J Appl.Math* (1999).

[39] X. Jia and P. Jolly, 'Simulation of Microwave Field and Power Distribution in a Cavity by a Three–Dimensional Finite Element Method', *Journal of Microwave Power and Electromagnetic Energy*, **27(1)**, 11–22 (1992).

[40] D. C. Dibben and A. C. Metaxas, 'Time Domain Finite Element Analysis of Multimode Microwave Applicators', *IEEE Transactions on Magnetics*, **32(3)**, 942–945 (1996).

[41] P. Monk and E. Suli, 'Error Estimates for Yee's Method on Non–uniform Grids', *IEEE Transactions on Magnetics*, **30(5)**, 3200–3203 (1994).

[42] P. Monk, 'Sub–Gridding FTDT Schemes', *ACES Journal*, **11**, 37–46 (1996).

[43] M. Pourcq, 'Field and Power-Density Calculations in Closed Microwave Systems by Three-Dimensional Finite Differences', *IEE Proceedings*, **132(6)**, 360–368 (1985).

[44] A. Taflove, 'Application of the finite–difference time–domain method to sinusoidal steady–state electromagnetic–penetration problems', *IEEE Trans. Electromagn. Compat.*, **22(2)**, 191–202 (1980).

[45] D. C. Dibben and A. C. Metaxas, 'Frequency Domain vs. Time Domain Finite Element Methods for Calculation of Fields in Multimode Cavities', *IEEE Transactions on Magnetics*, **33(2)**, 1486–1471 (1997).

[46] S. M. Rao, D. R. Wilton and A. W. Glisson, 'Electromagnetic scattering by surfaces of arbitrary shape', *IEEE Trans. on Ant. and Propag.*, **30(3)**, 409–418 (1982).

[47] C. Lu and W. C. Chew, 'The use of Huygens equivalence principle for solving 3–D integral equation for scattering', *IEEE Trans. on Ant. and Propag.*, **30(3)**, 409–48 (1982).

[48] R. Luebbers, F. P. Hunsberger, K. S. Kunz, R. B. Standler and M. Schneider, 'A Frequency–Dependent Finite–Difference Time–Domain Formulation for Dispersive Materials', *IEEE Transactions on Electromagnetic Compatibility*, **32(3)**, 222–227 (1990).

[49] O. P. Gandhi, B.-Q. Gao and J.-Y. Chen, 'A Frequency–Dependent Finite–Difference Time–Domain Formulation for General Dispersive Media', *IEEE Transactions on Microwave Theory and Techniques*, **41(4)**, 658–665 (1993).

[50] G. A. Kriegsmann, 'Microwave Heating of Dispersive Media', *J. Appl.Math*, **53(3)**, 655–669 (1993).

[51] S. V. Patankar, *Numerical Heat Transfer and Fluid Flow*. McGraw–Hill, New York (1980).

[52] D. S. Chen, R. K. Singh, R. K. Haghighi and P. E. Nelson, 'Finite element analysis of temperature distribution in microwaved particulate foods ', *American Society of Agricultural Engineers*, 1–11 (1990).

[53] J. Tattiyakul, M. A. Rao and A. K. Datta, 'Simulation of heat transfer to a canned corn starch dispersion subjected to axial rotation', *Chemical Engineering and Processing*, **40**, 391–399 (2001).

[54] A. K. Datta and J. Liu, 'Thermal time distributions for microwave and conventional heating of food', *Trans IChemE*, **70**, 83–90 (1992).

[55] A. V. Luikov, 'Systems of differential equations of heat and mass transfer in capillary porous bodies', *International Journal of Heat and Mass Transfer*, **18**, 1–14 (1973).

[56] Z. H. Wang and M. H. Shi, 'Numerical Study on Sublimation-Condensation Phenomena During Microwave Freeze Drying', *Chemical Engineering Science*, **53(18)**, 3189–3197 (1998).

[57] G. Lian, C. S. Harris, R. Evans and M. Warboys, 'Coupled Heat and Moisture Trasfer During Microwave Vacuum Drying', *Journal of Microwave Power and Electromagnetic Energy*, **32(1)**, 34–43 (1997).

[58] L. Zhou, V. M. Puri, R. C. Anantheswaran and G. Yeh, 'Finite Element Modeling of Heat and Mass Transfer in Food Materials During Microwave Heating – Model Development and Validation', *Journal of Food Engineering*, **25**, 509–529 (1994).

[59] H. Ni, A. K. Datta and K. E. Torrance, 'Moisture Transport in Intensive Microwave Heating of Biomaterials: A Multiphase Porous Media Model', *International Journal of Heat and Mass Transfer*, **42**, 1501–1512 (1999).

[60] H. Ni and A. K. Datta, 'Moisture loss as related to heating uniformity in microwave processing of solid foods', *Journal of Food Process Engineering*, **22**, 367–382 (1999).

[61] H. Ni and A. K. Datta, 'Moisture, oil and energy transport during deep-fat frying of fat materials', *Trans IChemE*, **77**, 194–204 (1999).

[62] H. Ni and A. K. Datta, 'Moisture distribution and loss in microwave heating of foods: effect of food structure, initial moisture level and surface conditions', *Trans IChemE*, **17**, 200–210 (1999).

[63] P. Perré and I. W. Turner, 'A 3-D Version of TransPore:A Comprehensive Heat and Mass Transfer Computational Model for Simulating the Drying in Porous Media', *International Journal of Heat and Mass Transfer*, **42**, 4501–4521 (1999).

[64] W. Fu and A. Metaxas, 'Numerical Prediction of Three-Dimensional Power Density Distributions in a Multi-Mode Cavity', *Journal of Microwave Power and Electromagnetic Energy*, **29(3)**, 67–75 (1994).

[65] A. K. Datta and R. C. Anantheswaran, *Handbook of Microwave Technology for Food Applications*. Marcel Dekker, New York (2001).

[66] K. G. Ayappa, H. T. Davis, E. A. Davis and J. Gordon, 'Analysis of Microwave Heating of Materials with Temperature-Dependent Properties', *AIChE Journal*, **37(3)**, 313–322 (1991).

[67] F. Torres and B. Jecko, 'Complete FTDT Analysis of Microwave Heating Processes in Frequency–Dependent and Temperature–Dependent Media', *IEEE Transactions on Microwave Theory and Techniques*, **45(1)**, 108–117 (1997).

[68] F. Liu, I. Turner, E. Siores and P. Groombridge, 'A Numerical and Experimental Investigation of the Microwave Heating of Polymer Materials Inside a Ridge Waveguide', *Journal of Microwave Power and Electromagnetic Energy*, **31(2)**, 71–81 (1994).

[69] J. Clemens and C. Saltiel, 'Numerical modeling of microwave processing in microwave furnaces ', *IJHMT*, **39(9)**, 1665–1675 (1996).

[70] P. Monk and K. Parrott, 'Phase–Accuracy Comparisons and Improved Far–Field Estimates for 3–D Edge Elements on Tetrahedral Meshes', *Journal of Computational Physics*, **170**, 614–641 (2001).

[71] Z. Bi, K. Wu, C. Wu and J. Litva, 'A dispersive boundary condition for microstrip component analysis using FT–DT method ', *IEEE Transactions on Microwave Theory and Techniques*, **40(4)**, 774–776 (1992).

[72] R. W. M. Lau and R. J. Sheppard, 'The modelling of biological systems in three dimensions using the time domain finite–difference method:I.The implementation of the model', *The institute of Physics*, **31**, 1247–1256 (1986).

[73] M. Sundberg, P.-S. K. P. O. Risman and T. Ohlsson, 'Analysis and Design of Industrial Microwave Ovens Using the Finite Difference Time Domain Method', *Journal of Microwave Power and Electromagnetic Energy*, **31(3)**, 142–157 (1996).

[74] A. Taflove, 'Review of the formulation and applications of the finite–difference time–domain method for numerical modelling of electromagnetic wave interaction with arbitrary structures', *Wave Motion*, **10**, 547–582 (1988).

[75] G. Mur, 'Absorbing boundary conditions for finite–difference approximation o the time domain electromagnetic field equations', *IEEE Transactions on Electromagneic Compatibility*, **23**, 1073–1077 (1981).

[76] J. Bear, *Dynamics of Fluids in Porous Media*. Dover Publications, New Yor (1998).

[77] S. Whitaker, 'Simultaneous heat, mass and momentum transfer in porous media a theory of drying ', *Advances in Heat Transfer*, **31**, 1–104 (1998).

[78] 'Commercial CFD codes (http://icemcfd.com/cfd)' (2002).

[79] D. B. Spalding, *Numerical Computation of Multiphase Flow and Heat-transfer* Pineridge Press, Swansea (1981).

[80] T. N. Croft, 'Unstructured Mesh - Finite Volume Algorithms for Swirling, Turbulent, Reacting Flows', *PhD Thesis, University of Greenwich* (1997).

[81] D. D. Dincov, K. A. Parrott and K. A. Pericleous, '2-D Mapping Between FD-TD and FV Methods on Structured Uniform Meshes ', 9^{th} *Annual Proceedings of the Postgraduate Seminar Series, CMS Press*, **(9)** (2000).

[82] A. Yefet and P. Petropoulos, 'A Non-Dissipative Staggered Fourth-order Accurate Explicit Finite Difference Scheme for the Time-Domain Maxwell's Equations', *NASA/CR-1999-209514.*, **99** (1999).

[83] D. D. Dincov, K. A. Parrott and K. A. Pericleous, '2-D Coupled Electromagnetic and Thermal Solvers for Microwave Heating Simulation', 8^{th} *Annual Proceedings of the Postgraduate Seminar Series, CMS Press*, **(9)** (1999).

[84] D. D. Dincov, K. A. Parrott and K. A. Pericleous, 'Microwave Heating and Phase Change and Phase Change in Two-phase Porous Materials ', *Computational Fluid Dynamics Conference Proceedings, Eccomas 2001* (2001).

[85] D. D. Dincov, K. A. Parrott and K. A. Pericleous, 'Coupled 3-D Finite Difference Time Domain and Finite Volume Methods for Solving Microwave Heating in Porous Media', *Lecture Notes in Computer Science*, **2329(1)**, 813–822 (2002).